Ludwig-Maximilians-Universität München

Sektion Physik

A Flavour Independent Search for Neutral Higgs Bosons in the 2HDM Framework with the OPAL Detector at LEP

Diplomarbeit

von

Tatjana Unverhau

September 2000

Erstgutachterin: Prof. Dr. D. Schaile
Zweitgutachter: Prof. Dr. C. Kiesling

Ludwig-Maximilians-Universität München

Sektion Physik

A Flavour Independent Search for Neutral Higgs Bosons in the 2HDM Framework with the OPAL Detector at LEP

Diplomarbeit

von

Tatjana Unverhau

September 2000

To my parents

Abstract

Three decades ago the Higgsmechanism was introduced, to give mass to otherwise massless gauge bosons.

This thesis presents a search for the neutral Higgs bosons h and A, as they occur in type II of models with two scalar Higgs field doublets. Analyzed is the process $e^+e^- \rightarrow Z \rightarrow hA$, with sensitivity to all hadronic decay modes including regions in the parameter space where the decay to b quarks is suppressed. In standard analyses the identification of b quarks is a very powerful tool and its exclusion leads to a decreased sensitivity. To compensate for this, a mass dependent analysis was developed. This allows an optimal use of kinematical information which remains the only means to efficiently discriminate between signal and background processes.

The analysis is applied to the data collected in 1998 with the OPAL detector at a centre-of-mass energy of 189 GeV, corresponding to an integrated luminosity of 172.1 pb^{-1}. No signal has been observed above the Standard Model background, which leads to the exclusion of the h and A for certain masses and values of the model parameters.

Contents

List of Figures

List of Tables

Chapter 1

Introduction

What is the world made of? This question was asked first about 2500 years ago by Greek philosophers. Ever since it has occupied peoples minds, seeking for a understanding of nature. The answers changed drastically over the centuries. There have been ideas such as that basic matter is water, or that all matter is composed out of four basic natural elements: fire, water, earth and air.

The first concept of elementary particles dates back to Demokrit from Abdera who lived from 460-370 BC. He introduced the principle of non-continuous matter. Subdividing matter ever further one would reach a limit and end up with an invisible, indivisible substance. After the Greek word for indivisible, *atomos*, he called them atoms. This idea did not gain popularity until the early 18th century, when the Frenchman Joseph Gay-Lussac found that oxygen and hydrogen produce water always with the same ratio. To him this indicated that the elements consist of basic units. John Dalton took a further step by proposing that every element has its own type of atoms and all atoms of one element are identically. This puzzle was solved by the Russian chemist Dimitri Ivanovich Mendelejev. In 1869 he derived a system of classification for the elements. He ordered them by their atomic weight and discovered that the properties of the elements seem to change with a periodic pattern. From gaps in his table he predicted new elements with certain properties. Their subsequent discovery proved to be a great success for his model. In the last few decades our understanding of nature, and what we state as elementary particles has been revolutionized several times. Sophisticated technologies enable us to accelerate subatomic particles to ever higher energies, which again enables us to create ever heavier particles in collisions. In our present model, fermions, of which there are quarks and leptons, form the elementary constituents of matter. The model describing all interactions between these particles[1], mediated by so-called gauge bosons, is called the Standard Model.

Predictions of the Standard Model have been verified with extremely high precision in modern experiments. However, the key mechanism giving rise to masses in this model is not yet verified. It predicts at least one scalar particle, the so-called Higgs boson. Even if this particle itself is responsible to give rise to masses, the theory results in a complete ignorance of the mass of the particle itself. As yet it withdrew from detection.

The Large Electron-Positron Collider at the European Centre for Particle Physics (CERN) close to Geneva in Switzerland is able to accelerate particles to energies as high as 104.5 GeV, with a centre-of-mass energy twice as high. Electrons and positrons are assumed to have no substructure, thus all their energy is available to create new massive particles.

In this thesis an analysis will be described that searches for two neutral scalar Higgs particles that could be pairproduced in collisions of electrons and positrons. These particles occur in models with

[1] Gravitation is not included in this model

two scalar Higgs field doublets. As mentioned, the minimal choice is one Higgs field which gives rise to one Higgs boson. As Higgs bosons couple proportional to their mass, they mainly decay into heavy particles. For hadronic decay modes below the top quark threshold, that means a decay into b-quarks, which leave a rather significant print within the detector and therefore help in finding the Higgs boson. In models with two doublets five physical Higgs bosons occur (two have equal masses). Additionally to the four unknown masses there are two new free parameters. Depending on these parameters, a decay into b-quarks can be highly suppressed. Previous analyses mainly focused on the informations from b-quarks and thus are not sensitive in regions with diminishing or even vanishing decay rates to b-quarks. No Higgs bosons have been found in these searches and the quoted limits on their mass refer to certain regions in the parameter space with reasonably high b-quark decay rates.

To be sensitive to hadronic Higgs boson decays in all regions of this parameter space this analysis makes no use of any flavour specific information. The hadronic decay channels leads to four, so-called jets, in the final state. At the centre-of-mass energies of the LEP accelerator, pairproduced W bosons, which can also lead to a final state with four jets, constitute a major background to this process. Without the use of b-quark specific information however this background is hard to reject. Therefore, a mass-dependent approach was chosen for the analysis, which allows the efficient use of kinematical variables to discriminate the signal from background events.

The analysis is applied to data collected in 1998 with the OPAL detector at a centre-of-mass energy of 189 GeV, corresponding to an integrated luminosity of 172.1 pb^{-1}.

Chapter 2

Theoretical Overview

2.1 Standard Model

The Standard Model (SM) of particle physics quantitatively describes all interactions of the fundamental particles except quantum gravity effects. All interactions within this model are formulated as gauge theories. The following chapter presents a brief introduction to the particle content of the Standard Model and a discussion of the underlying principle of gauge theories.

2.1.1 Particle Content

Particles can be classified according to their spin statistics as either bosons (with integer spin) or fermions (with half integer spin). Quarks and Leptons, carrying spin 1/2, belong to the latter group and are believed to be the fundamental constituents of matter. Six leptons – as well as their antiparticles – are currently known: the electron (e^-), the muon (μ^-), the tau (τ^-) and the corresponding neutrinos. They interact solely through the weak interaction and, if charged, additionally through the electromagnetic force. Quarks, on the other hand, are in addition subject to the strong force and thus participate in all interactions. Analogously to leptons there are six types: up (u), down (d), strange (s), charm (c), bottom (b) and top (t) quark (again along with their anti-particles).

These fundamental quarks and leptons can be grouped into families or generations, one generation reflecting the other in its behaviour under the strong, electromagnetic and weak force. The difference lies in the particles' masses, the first generation containing all the lightest particles of a kind.

At the present state of knowledge, it is neither clear where this grouping originates from, nor is it certain that there are not more than three generations [1]. The assignment of the particles to generations, as well as some of their properties are summarized in table 2.1.

2.1.2 Forces

All interactions in the Standard Model are derived by insisting that the invariance of the Lagrangian of a system under global gauge transformations should hold locally [2]. The idea of local gauge invariance was first introduced by the work of Hermann Weyl in 1919 [2]. The application of local gauge

[1] A forth generation would have to contain heavier particles, if it should fit into this scheme, as measurements of upper bounds on the primordial mass fraction of ^{4}He and precise measurements of the Z-Boson width at LEP determine the number of generations of light neutrinos ($m_\nu < m_Z/2$) to be three.

[2] Local gauge transformations are transformations whose parameters are space-time dependent.

Quarks

Generation	Symbol	Charge	Mass(GeV) [1]
1.	u	$+2/3$	0.001 to 0.005
	d	$-1/3$	0.003 to 0.009
2.	c	$+2/3$	1.15 to 1.35
	s	$-1/3$	0.075 to 0.170
3.	t	$+2/3$	174.3 ± 5.1
	b	$-1/3$	4.0 to 4.4

Leptons

Generation	Symbol	Charge	Mass(MeV) [1]
1.	ν_e	0	< 0.000003
	e^-	-1	$0.510998902 \pm 0.000000021$
2.	ν_μ	0	< 0.19
	μ^-	-1	$105.6583568 \pm 0.0000052$
3.	ν_τ	0	< 18.2
	τ^-	-1	$1777.03^{+0.30}_{-0.26}$

Table 2.1: The three generations of fundamental fermions. The large uncertainties in the quark masses are due to the fact that quarks do not exist as free particles. The large top mass however permits direct measurements, as the top quark decays before hadronisation.

invariance to the Dirac Lagrangian generated all of electrodynamics. The concept of gauge theories will be summarized following the case of electrodynamics. Although this presents the simplest case it still contains all the important concepts.

Gauge Theories and the Electromagnetic Force

Starting from the the theory of a free electron, described by its 4-component complex spinor field Ψ_i (i=1,2,3,4). The Lagrangian density for such a free Dirac field Ψ is

$$\mathcal{L} = \bar{\Psi}(x)(i\gamma^\mu \partial_\mu - m)\Psi(x), \tag{2.1}$$

with $\bar{\Psi} = \Psi^+\gamma_0$ and γ_μ the 4x4 Dirac matrices. m is the electron mass. Phase transformations of the kind $\Psi(\mathrm{x}) \rightarrow \Psi'(\mathrm{x}) = \mathrm{e}^{\mathrm{i}\Theta}\Psi(\mathrm{x})$ [3], Θ being any real number, are called *global* phase transformations as the phase of the transformation is the same for any of the space time points x. In this case $\bar{\Psi}$ has to be transformed to $\bar{\Psi}e^{-i\Theta}$ and in the $\bar{\Psi}\Psi$ combinations the exponential factors cancel out. When we apply on the other hand a *local* gauge transformation, i.e. we allow the phase to vary from point to point: $\Psi(\mathrm{x}) \rightarrow \Psi'(\mathrm{x}) = \mathrm{e}^{\mathrm{i}\Theta(\mathrm{x})}\Psi(\mathrm{x})$, the Dirac Lagrangian is no longer invariant for we pick up an extra term from the derivative of Θ:

$$\partial_\mu(e^{i\Theta}\Psi) = i(\partial_\mu\Theta)e^{i\Theta}\Psi + e^{i\Theta}\partial_\mu\Psi$$

resulting in

$$\mathcal{L} \rightarrow \mathcal{L} - \partial_\mu\Theta\bar{\Psi}\gamma^\mu\Psi.$$

[3] The set of all such phase transformations is the group U(1). As $e^{i\Theta_1}e^{i\Theta_2} = e^{i\Theta_2}e^{i\Theta_1}$, it is an Abelian group.

For the following, it is helpful to replace Θ with $q\lambda(x)$, q being a charge. So the free Dirac Lagrangian is not invariant under local gauge transformations. If we now demand it to be invariant, we have to add an extra term to cancel the disturbing derivative. Suppose

$$\mathcal{L} = \bar{\Psi}(x)(i\gamma^\mu \partial_\mu - m)\Psi(x) - q\bar{\Psi}\gamma^\mu \Psi A_\mu, \tag{2.2}$$

A_μ being a new field (referred to as gauge field) that transforms as

$$A_\mu \rightarrow A_\mu^{'} = A_\mu + \partial_\mu \lambda. \tag{2.3}$$

This new Lagrangian is invariant under local gauge transformations, if the field transforms according to equation (2.3). However this is not the full Lagrangian, the field needs its free term. The Lagrangian for a free vector field is

$$\mathcal{L} = -\frac{1}{16\pi} F^{\mu\nu} F_{\mu\nu} + \frac{1}{8}\pi m_A A^\nu A_\nu.$$

While $F^{\mu\nu} = \partial^\mu A^\nu - \partial^\nu A^\mu$ stays invariant if transforming A_μ according to equation (2.3), the mass term does not. Therefore, if the latter term is not to spoil the invariance, the field A_μ has to be massless. Thus we get:

$$\mathcal{L} = \bar{\Psi}(x)(i\gamma^\mu \partial_\mu - m)\Psi(x) - q\bar{\Psi}\gamma^\mu \Psi A_\mu + \frac{-1}{16\pi} F^{\mu\nu} F_{\mu\nu}. \tag{2.4}$$

This can be exactly identified with the Lagrangian for Quantum Electro Dynamics (QED). The first term describes the kinetic energy and mass of Ψ, the second determines the interaction - how the field A_μ couples to Ψ via the charge q and the third term contains the kinetic energy of A_μ, which is precisely the electromagnetic potential. The last two terms reproduce the Maxwell Lagrangian for a massless vector field with the current density $J^\mu = q(\bar{\Psi}\gamma^\mu \Psi)$. Demanding that global gauge invariance should hold locally generated all of electrodynamics. The form of the Lagrangian in equation (2.2) can be derived by introducing the covariant derivative $D_\mu \equiv \partial_\mu + iqA_\mu$. Then replacing ∂_μ with D_μ and $A_\mu \rightarrow A_\mu + \partial_\mu \lambda$ the Lagrangian is invariant under $\Psi \rightarrow \Psi e^{iq\lambda(x)}$.

The gauge transformation can as well be described as a multiplication of the wave function with e^{iH}. H is in the case of electrodynamics simply a phase factor and as such the Lagrangian is said to be symmetric under an Abelian gauge transformation. In 1954 Yang and Mills extended the idea from the Abelian case of electrodynamics (with the photon representing that newly introduced gauge field) to the non Abelian case of the group SU(2), H being a 2×2 hermitian matrix. The three vector fields, needed to provide local gauge invariance, have to be massless again and at that time no isotriplet of particles with the necessary features had been observed. However, Yang and Mills had shown that it is possible to extend Weyls idea to the non-Abelian case. The power and generality of local gauge invariance was not fully appreciated though until the early 70's when t'Hooft showed that gauge theories are automatically renormalizable.

The Strong Interaction

The first application of the gauge principle in the non-Abelian case was to describe the strong interaction. The gauge theory describing the strong interaction is known as Quantum Chromodynamics (QCD). It is based on the non-Abelian group SU(3). Analogously to the electric charge, particles that are subject to this force (the quarks) carry a charge referred to as colour (therefore "chromo" dynamics). They exist in three colours, namely red, green, and blue. Demanding the Lagrangian of the

system to be invariant under local gauge transformations leads to the introduction of eight massless gauge fields, in nature realised by the eight massless gluons. The gluons, carrying a combination of colour and anticolour themselves, mediate the strong force not just between quarks, but also between themselves. No free quarks have been observed. This is due to the fact, that what is called the coupling *constant* of the strong interaction is not a constant at all. In fact for non-Abelian gauge theories the coupling decreases with increasing momentum transfer Q. At large values of Q^2 the coupling becomes small enough for processes to be calculated perturbatively and the quarks can be regarded as quasi-free particles. This feature of QCD is referred to as asymptotic freedom. The opposite effect that at increasing distances and thus small Q^2 the coupling becomes strong is referred to as confinement. This effect is most likely responsible for that we just observe colour singlet states, where quarks are confined forming mesons ($q\bar{q}$) and baryons (qqq). If quarks move apart from each other (for instance because of energy conservation after they were produced in high energy e^+e^-- collisions), the further they move apart the larger becomes the binding energy, so that energetically it is more favourable to create new $q\bar{q}$ pairs until colour singlet objects are produced.

The Weak Interaction

The weak interaction was first derived by Enrico Fermi as a point-like interaction with a 4-particle coupling and as such no force-mediating bosons. This description however is just a good approximation of reality for low energies. At high energy certain weak processes violate unitarity. The first attempts to describe the weak interaction as SU(2) gauge theory failed and it became apparent that the weak interaction could only be described in such a framework together with the electromagnetic interaction. Glashow, Weinberg and Salam finally succeeded in deriving both forces as different components of a single gauge theory. The underlying gauge group is the direct product of $\mathrm{U(1)_Y}$ and $\mathrm{SU(2)_L}$. L stands for left handed, taking into account, that the weak interaction is parity violating and thus left and right handed components of the fields should be treated separately. Y stands for the weak hypercharge [4], defined as

$$\frac{\mathrm{Y}}{2} = Q_{em} - I_3,$$

where I_3 is the third component of the weak isospin I and Q_{em} the electromagnetic charge. Fermion fields in this theory are separated into left and right handed components. The left-handed electron and neutrino fields form doublets, while in absence of right-handed neutrinos the right-handed electron fields form singlets concerning the weak isospin:

$$\begin{pmatrix} \mathrm{e} \\ \nu_\mathrm{e} \end{pmatrix}_\mathrm{L} \quad \begin{pmatrix} \mu \\ \nu_\mu \end{pmatrix}_\mathrm{L} \quad \begin{pmatrix} \tau \\ \nu_\tau \end{pmatrix}_\mathrm{L} \quad \begin{pmatrix} \mathrm{u} \\ \mathrm{d}' \end{pmatrix}_\mathrm{L} \quad \begin{pmatrix} \mathrm{c} \\ \mathrm{s}' \end{pmatrix}_\mathrm{L} \quad \begin{pmatrix} \mathrm{t} \\ \mathrm{b}' \end{pmatrix}_\mathrm{L} \quad \begin{matrix} I_3 = 1/2 \\ I_3 = -1/2 \end{matrix} \tag{2.5}$$

$$\mathrm{e_R},\ \mu_R,\ \tau_R,\ \mathrm{u_R},\ \mathrm{c_R},\ \mathrm{t_R},\ \mathrm{d_R},\ \mathrm{s_R},\ \mathrm{b_R} \quad I = 0 \tag{2.6}$$

Demanding a gauge invariant theory requires the introduction of four gauge fields: a massless weak isospin triplet of gauge fields $\mathbf{W}_\mu = (W^1_\mu, W^2_\mu, W^3_\mu)$ and a massless hypercharge singlet gauge field B_μ.

[4] For that the groups $\mathrm{U(1)_Y}$ and $\mathrm{SU(2)_L}$ commute Y has to take the same value for the charged fermion and the neutrino fields.

Thus, the covariant derivative for the gauge group $\mathrm{U(1)_Y} \times \mathrm{SU(2)_L}$ is

$$D_\mu = \partial^\mu + ig\mathbf{T}\mathbf{W}^\mu + i\frac{g'}{2}YB^\mu, \tag{2.7}$$

For left-handed leptons we have $\mathbf{T}= \tau/2, Y = -1$, for right-handed charged leptons $\mathbf{T} = 0$ and $Y = -2$, the τ are the Pauli matrices. As mentioned above, $\mathrm{SU(2)_L}$ and $\mathrm{U(1)_Y}$ can not be identified with the weak and the electromagnetic interaction respectively. For instance, the neutral gauge field W_μ^3 cannot be identified with the Z^0 boson, as observations show that the neutral non-QED current is not purely left-handed. The physical bosons are linear combinations of the four fields:

$$\begin{aligned} W_\mu^\pm &= \frac{1}{\sqrt{2}}(W_\mu^1 \mp iW_\mu^2) \\ Z_\mu &= -B_\mu \sin\Theta_w + W_\mu^3 \cos\Theta_w \equiv \mathrm{Z}^0 \\ A_\mu &= B_\mu \cos\Theta_w + W_\mu^3 \sin\Theta_w \equiv \gamma \end{aligned} \tag{2.8}$$

The problem remains, that these bosons are required to be massless, which is true for the photon, but obviously false for the Z^0 boson with a mass of about 91.2 GeV and the $\mathrm{W}^\pm$ bosons with masses of about 80.4 GeV [1]. One could start with a gauge invariant theory and add the mass terms by hand. However this would destroy the renormalizability of the theory. A rather elegant way to introduce masses to the theory lies in the principle of spontaneous symmetry breaking and the Higgs mechanism.

2.1.3 Spontaneous Symmetry Breaking and the Higgs Mechanism

Feynman calculus is based on perturbation theory, where fields are treated as fluctuations around the ground state. Thus one has to look for the minimum of the potential term in the Lagrangian and re-express $\mathcal{L}$ as a function of the deviation η from its minimum. Then expanding in powers of η one can extract the mass term as the coefficient of the η^2 term. If then we have a system where, because of an additional potential, the ground state of that system does not share the symmetry of the Lagrangian, the fields acquire mass. This phenomenon is often referred to as spontaneous symmetry breaking or hidden symmetry (as the ground state does not show the symmetry of the Lagrangian - all ground states taken together do though, but choosing one, the system looses its symmetry, the symmetry is said to be broken).

This shall be illustrated with the following Lagrangian of the two fields Φ_1 and Φ_2:

$$\mathcal{L} = \frac{1}{2}(\partial_\mu\Phi_1)(\partial^\mu\Phi_1) + \frac{1}{2}(\partial_\mu\Phi_2)(\partial^\mu\Phi_2) + \frac{1}{2}\mu^2(\Phi_1^2+\Phi_2^2) - \frac{1}{4}\lambda^2(\Phi_1^2+\Phi_2^2)^2 \tag{2.9}$$

As $\mathcal{L} = \mathcal{T} - \mathcal{U}$, the potential in this case is

$$\mathcal{U} = -\frac{1}{2}\mu^2(\Phi_1^2+\Phi_2^2) + \frac{1}{4}\lambda^2(\Phi_1^2+\Phi_2^2)^2. \tag{2.10}$$

The minima of this potential lie on a circle of radius μ/λ:

$$\Phi_{1min}^2 + \Phi_{2min}^2 = \mu^2/\lambda^2. \tag{2.11}$$

To re-express the Lagrangian we have to choose a particular ground state. For the sake of simplicity we pick

$$\Phi_{1min} = \mu/\lambda; \quad \Phi_{2min} = 0.$$

The deviations from this ground state can be expressed as the new fields

$$\eta \equiv \Phi - \mu/\lambda; \quad \xi \equiv \Phi_2.$$

In terms of these new fields the Lagrangian of eq.(2.9) writes as:

$$\begin{aligned} \mathcal{L} =& [\frac{1}{2}(\partial_\mu \eta)(\partial^\mu \eta) - \mu^2 \eta^2] + [\frac{1}{2}(\partial_\mu \xi)(\partial^\mu \xi)] \\ &+ [\mu\lambda(\eta^3 + \eta\xi^2) - \frac{\lambda^2}{4}(\eta^4 + \xi^4 + 2\eta^2\xi^2)] + \frac{\mu^4}{4\lambda^2}. \end{aligned} \tag{2.12}$$

The first term is just the Lagrangian for a scalar field η with mass $m_\eta = \sqrt{2}\mu$, the second is the free Lagrangian of a massless field ξ. The additional terms define couplings between η and ξ. So now one is left though with a massless ghost particle [5]. The cure to that problem lies in applying the idea of spontaneous symmetry breaking to the case of local gauge invariance. This is referred to as Higgs mechanism. If the Lagrangian is gauge invariant the phase can be arbitrarily chosen. Thus, finding an appropriate choice of gauge the Goldstone boson will be absorbed as the third degree of freedom, the longitudinal polarization degree of freedom, of a massless vectorfield which as such acquires mass. A massive gauge field and a massive scalar (referred to as Higgs particle) are left.

The simplest Higgs structure in the framework of the electroweak theory, that breaks the $\mathrm{U(1)_Y \times SU(2)_L}$ down to $\mathrm{U(1)_{em}}$ and gives rise to massive gauge bosons, consists of two complex fields, that form a weak isospin doublet:

$$\Phi = \begin{pmatrix} \phi^+ \\ \phi^0 \end{pmatrix} \quad I = 1/2, \qquad \mathrm{Y} = 1 \tag{2.13}$$

As just one physical Higgs boson occurs in this theory it is often referred to as Higgs boson of the minimal Standard Model. While all its couplings to bosons and fermions are known, the minimal Higgs boson is characterized by a complete ignorance of its mass. However there are some theoretical constraints on upper and lower limits for the Higgs mass. Detailed remarks to all features of a Higgs boson in this minimal Model, namely production and decay mechanism as well as theoretical constraints on its mass can be found in [3]. Precision measurements of electroweak observables provide a way to derive limits on the Higgs boson mass. At LEP2 the best global fit to these observables leads, due to the logarithmic dependence on the Higgs boson mass that enters the calculation via virtual Higgs boson corrections to $W^\pm$ and Z self boson energies, to a value [4] of the Higgs mass of

$$m_\mathrm{H} = 62^{+53}_{-30}\mathrm{GeV}.$$

Translated into an upper limit at the 95% confidence level that yields to $m_\mathrm{H} < 170$ GeV. Figure 2.1 shows the contribution of the Higgs mass to the χ^2 of a simultaneous fit of all Standard model parameters as a function of the Higgsmass. Despite the enormous effort that has been made to search for such a scalar particle it has not yet been observed. Direct searches for the Higgs boson at LEP2 lead to a lower limit on its mass $m_\mathrm{H} < 113.3$ GeV [5].

As there are few constraints on the Higgs sector within the Standard Model more complicated Higgs models should be considered also.

Models with two scalar Higgs field doublets are an attractive alternative. They can not only provide masses for gauge bosons and fermions within the Standard Model but as well as in extensions of the Standard Model such as sypersymmetric theories.

[5] The fact that a spontaneously broken continuous global symmetry is always accompanied by the appearance of massless scalar particles is known as Goldstone's theorem.

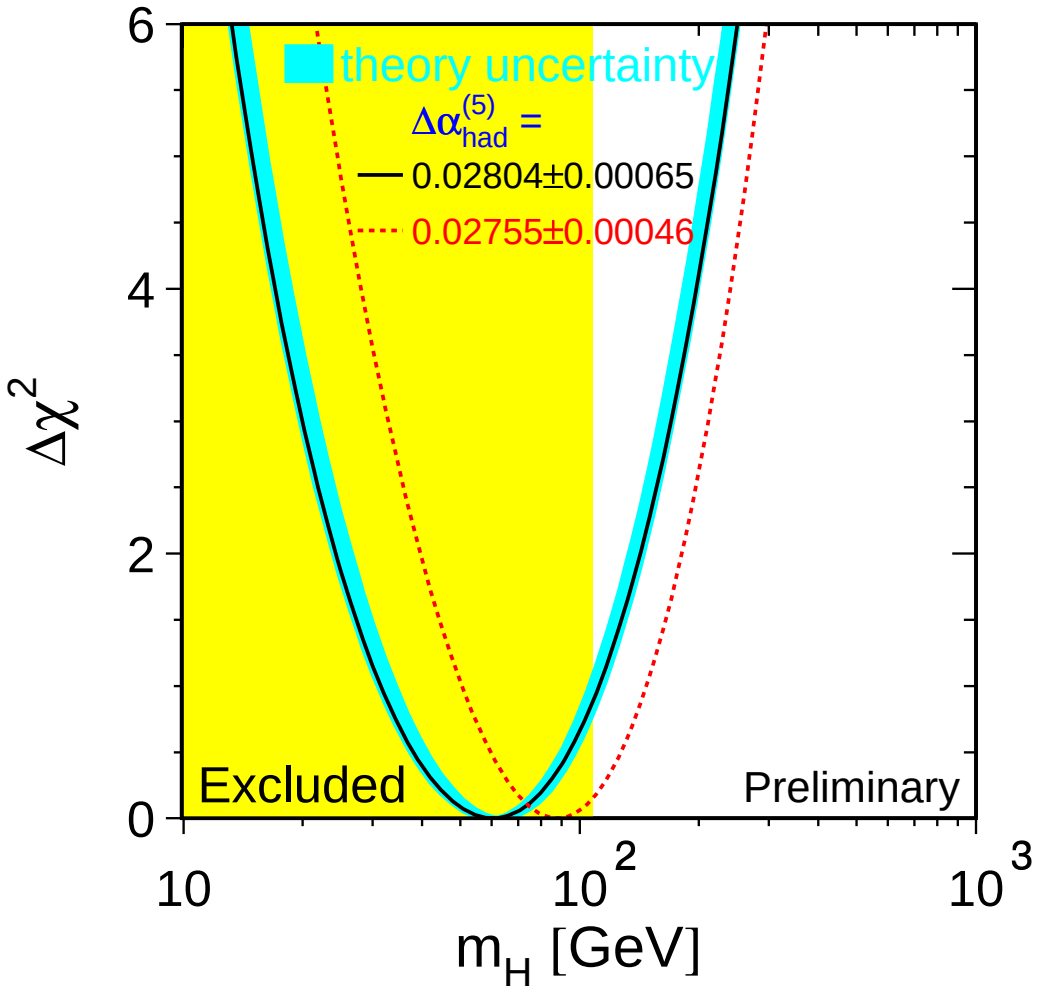

Figure 2.1: $\Delta\chi^2 = \chi^2 - \chi^2_{min}$ *vs.* m_{H} curve. The line is the result of the fit using all electroweak data. The band represents an estimate of the theoretical error due to missing higher order corrections. The vertical band shows the 95 % CL exclusion limit from the direct search [4].

2.2 Models with two scalar Higgs Field Doublets

In addition to the Higgs boson in the Standard Model (single doublet) there exists a wide variety of Models with two scalar Higgs field doublets. In the following the features particularly of type II of these models will be introduced. Equations are, if not otherwise indicated, taken from [3], which provides an extensive treatment of this subject.

2.2.1 Theoretical Structure

The most general Higgs potential in this framework is

$$\begin{aligned} V(\Phi_1,\Phi_2) =& \lambda_1(\Phi_1^\dagger\Phi_1 - v_1^2)^2 + \lambda_2(\Phi_2^\dagger\Phi_2 - v_2^2)^2 \\ &+\lambda_3[((\Phi_1^\dagger\Phi_1 - v_1^2) + (\Phi_2^\dagger\Phi_2 - v_2^2)]^2 \\ &+\lambda_4[(\Phi_1^\dagger\Phi_1)(\Phi_2^\dagger\Phi_2) - (\Phi_1^\dagger\Phi_2)(\Phi_2^\dagger\Phi_1)] \\ &+\lambda_5[Re(\Phi_1^\dagger\Phi_2) - v_1v_2\cos\xi]^2 \\ &+\lambda_6[Im(\Phi_1^\dagger\Phi_2) - v_1v_2\sin\xi]^2. \end{aligned} \tag{2.14}$$

Φ_1 and Φ_2 denote the two complex scalar fields

$$\begin{aligned} <\Phi_1> &= \begin{pmatrix} \phi_1^{0*} \\ -\phi_1^- \end{pmatrix}, \quad \mathrm{Y} = -1 \\ <\Phi_2> &= \begin{pmatrix} \phi_2^+ \\ \phi_2^0 \end{pmatrix}, \quad \mathrm{Y} = 1, \end{aligned} \tag{2.15}$$

that each form a doublet under $\mathrm{SU}(2)_\mathrm{L}$.

The λ_i in eq. 2.14 are real parameters, that if not negative yield the following minimum of the potential

$$<\Phi_1> = \begin{pmatrix} 0 \\ v_1 \end{pmatrix}, <\Phi_2> = \begin{pmatrix} 0 \\ v_2 e^{i\xi} \end{pmatrix}, \tag{2.16}$$

where v_1 and v_2 are the vacuum expectation values [6] of the Higgs fields and ξ is a CP violating phase. For the following ξ is set to zero to ensure CP-invariance within the Higgs sector.

Removing the Goldstone Bosons of the theory gives rise to five massive bosons, a charged scalar pair $\mathrm{H}^\pm$, the CP-even boson A and two CP-odd bosons h and H with $m_\mathrm{h} < m_\mathrm{H}$ by convention. This model has 6 free parameters, which are chosen to be the four masses of the Higgs bosons, the weak mixing angle α described below, and the ratio of the two vacuum expectation values defined as $\tan\beta$:

$$\tan\beta = \frac{v_1}{v_2}. \tag{2.17}$$

The physical Higgs state in the charged sector is

$$\mathrm{H}^\pm = -\Phi_1^\pm\sin\beta + \Phi_2^\pm\cos\beta \tag{2.18}$$

with a mass $m^2_{\mathrm{H}^\pm} = \lambda_4(v_1^2 + v_2^2)$. In the CP-odd sector we have one boson A,

$$\mathrm{A} = \sqrt{2}(-Im(\Phi_1^0)\sin\beta + Im(\Phi_2^0)\cos\beta) \tag{2.19}$$

with a mass $m^2_\mathrm{A} = \lambda_6(v_1^2 + v_2^2)$

In the CP-even sector two physical Higgs scalars mix through the following mass-squared matrix

$$\mathscr{M} = \begin{pmatrix} 4v_1^2(\lambda_1+\lambda_3) + v_2^2\lambda_5 & (4\lambda_3+\lambda_5)v_1v_2 \\ (4\lambda_3+\lambda_5)v_1v_2 & 4v_2^2(\lambda_2+\lambda_3) + v_1^2\lambda_5 \end{pmatrix} \quad , \tag{2.20}$$

[6] The vacuum expectation values v_1 and v_2 are related to the W mass via $m_\mathrm{W}^2 = g^2(v_1^2+v_2^2)/2$.

with the physical mass eigenstates

$$\begin{aligned} \mathrm{H}^0 &= \sqrt{2}[(Re(\Phi_1^0) - v_1)\cos\alpha + (Re(\Phi_2^0) - v_2)\sin\alpha], \\ \mathrm{h}^0 &= \sqrt{2}[-(Re(\Phi_1^0) - v_1)\sin\alpha + (Re(\Phi_2^0) - v_2)\cos\alpha] \end{aligned} \tag{2.21}$$

and the corresponding masses

$$m^2_{\mathrm{H}^0,\mathrm{h}^0} = \frac{1}{2}[\mathscr{M}_{11} + \mathscr{M}_{22} \pm \sqrt{(\mathscr{M}_{11} - \mathscr{M}_{22})^2 + 4\mathscr{M}_{12}^2}]. \tag{2.22}$$

The sixth free parameter, the mixing angle of the CP-even fields α is obtained from

$$\begin{aligned} \sin(2\alpha) &= \frac{2\mathscr{M}_{12}}{\sqrt{(\mathscr{M}_{11} - \mathscr{M}_{22})^2 + 4\mathscr{M}_{12}^2}}, \\ \cos(2\alpha) &= \frac{\mathscr{M}_{11} - \mathscr{M}_{22}}{\sqrt{(\mathscr{M}_{11} - \mathscr{M}_{22})^2 + 4\mathscr{M}_{12}^2}} \end{aligned} \tag{2.23}$$

2.2.2 Production Cross Sections and Decay Rates

The couplings of the Higgs bosons to gauge bosons and fermions are an important issue as they determine production cross sections as well as decay rates.

The production cross sections for the processes $\mathrm{e}^+\mathrm{e}^- \to \mathrm{Zh}$ and $\mathrm{e}^+\mathrm{e}^- \to \mathrm{hA}$ are [6]

$$\begin{aligned} \sigma(\mathrm{e}^+\mathrm{e}^- \to \mathrm{Zh}) &= \sin^2(\beta - \alpha)\sigma_{SM} \\ \sigma(\mathrm{e}^+\mathrm{e}^- \to \mathrm{hA}) &= \cos^2(\beta - \alpha)\bar{\lambda}\sigma_{SM}. \end{aligned} \tag{2.24}$$

The factor $\bar{\lambda}$ is defined as $\lambda_{\mathrm{Ah}}^{3/2}/[\lambda_{\mathrm{Zh}}^{1/2}(12m_Z^2/s + \lambda_{\mathrm{Zh}})]$ with the 2-particle phase space factor $\lambda_{ij} = (1-(m_i+m_j)^2/s)(1-(m_i-m_j)^2/s)$. σ_{SM} is the cross section for the Higgstrahlung process within the minimal Higgs of the Standard Model. This gives [6]

$$\sigma(\mathrm{e}^+\mathrm{e}^- \to \mathrm{ZH}) = \frac{G_F^2 m_Z^4}{96\pi s}(v_e^2 + a_e^2)\lambda_{\mathrm{HZ}}^{\frac{1}{2}} \frac{\lambda_{\mathrm{HZ}} + 12m_Z^2/s}{(1 - m_Z^2/s)^2}, \tag{2.25}$$

with the centre-of-mass energy $\sqrt{s}$ and the weak vector and axial vector couplings of the electron v_e and a_e respectively.

The couplings to fermions are determined by imposed constraints such as the absence of flavour changing neutral currents mediated by Higgs bosons. A theorem of Glashow and Weinberg predicts this absence if all fermions of a given electric charge couple to one of the Higgs doublets at most. This still leaves a variety of possible choices. Within two Higgs doublet models, type I is defined such that Φ_2 couples to all fermions, while Φ_1 couples to none of them. In type II, Φ_1 couples to down-type quarks and charged leptons while Φ_1 couples to up-type quarks and neutrinos.

Chapter 3

The OPAL Experiment

The OPAL Experiment is one of four collider experiments at the **L**arge **E**lectron-**P**ositron Collider (LEP), operated by the European Laboratory for Particle Physics, CERN.

Opposed to fixed target experiments, colliders have the advantage that the whole beam energy is available to create new massive particles. The Lorentz-invariant form for the total centre-of-mass energy of two colliding particles with masses m_1 and m_2 is

$$E_{cm} =: \sqrt{s} = \sqrt{(E_1 + E_2)^2 - (\vec{p}_1 \vec{p}_2)}$$

Considering just head-on collisions and particles with masses negligible compared to their energies this leads to:

$$\sqrt{s_{collider}} \approx \sqrt{4E_1 E_2}$$

At a fixed target experiment however (neglecting the mass m_1 of the accelerated particle) we have:

$$\sqrt{s_{fixed\ target}} \approx \sqrt{m_2 E_{beam}},$$

so that for E_{beam} being limited by present technology, colliders provide a discovery reach for far more massive particles.

A useful quantity to describe the performance of an accelerator is the factor of proportionality between event rate dN/dt and interaction cross-section $\sigma(s)$, the so-called luminosity $\mathscr{L}$:

$$dN/dt = \mathscr{L} \cdot \sigma(s). \tag{3.1}$$

In a collider circulating particles are grouped in bunches, that collide with a frequency f. For the case of an e^+e^- collider, with n circulating bunches per direction and N_{e^+} and N_{e^-} positrons and electrons per bunch respectively, the luminosity is given by

$$\mathscr{L} = f \frac{n N_{e^+} N_{e^-}}{4\pi \sigma_x \sigma_y}, \tag{3.2}$$

where σ_x and σ_y characterize the Gaussian transverse beam profiles in the horizontal and vertical directions.

For fixed target experiments the luminosity is generally higher, as Avogadros number enters the calculation through the density of the target material, so that the integrated luminosity for fixed target experiments lies in the order of $10^{36}\mathrm{cm}^{-2}\mathrm{s}^{-1}$, while the one for colliders reaches just about the order of $10^{32}\mathrm{cm}^{-2}\mathrm{s}^{-1}$.

3.1 The Accelerator

Figure 3.1: Aerial view of the Large Electron-Positron Collider (LEP). The LEP ring reaches from the airport on one side to the Jura mountain range on the other side.

The Large Electron-Positron Collider is located near Geneva on both sides of the border between Switzerland and France about a hundred meters below the surface. Figure 3.1 shows an aerial view of this accelerator, which is, with its 26.66 km in circumference, the world's largest e^+e^- collider. The ring consists of eight arcs connected by eight straight sections and is inclined by about 1.4 degrees with respect to the horizontal plane. Every other straight section is equipped with a general purpose detector (ALEPH, DELPHI, L3 and OPAL), designed to record all kinds of interactions that occur in e^+e^- collisions.
During operation, bunches of approximately 10^{11} particles circulate in a single evacuated beam pipe, with electrons and positrons moving in opposite directions. In the straight sections radio-frequency cavities accelerate the particles and compensate the energy loss that the particles suffer due to synchrotron radiation in the arcs. At the beam crossing points outside the detectors collisions are avoided by electrostatic separators or a special beam optic. The bending is achieved by dipole magnets in the arcs, the focussing with quadrupole and sextupole magnets. About four meters in front of the detectors the bunches are squeezed together to a dimension of about 200 μm $\times$ 8 μm (with a length of about 1 cm per bunch).

LEP started operation in 1989. For a period of six years—referred to as the LEP1 era—the machine was running at a centre-of-mass energy of about 91 GeV, the Z^0-resonance. In November 1995 the LEP energy was increased to 130–140 GeV and finally reached 161 GeV in 1996, the threshold for W-pair production, which marks the beginning of the LEP2 period. To achieve this goal LEP was upgraded with several superconducting cavities replacing some copper cavities and supporting the remaining ones. In its last year of running, 2000, LEP has so far reached a peak energy of about 209 GeV. A sketch of the LEP accelerator, its injection system and the four experiments can be seen in figure 3.2.

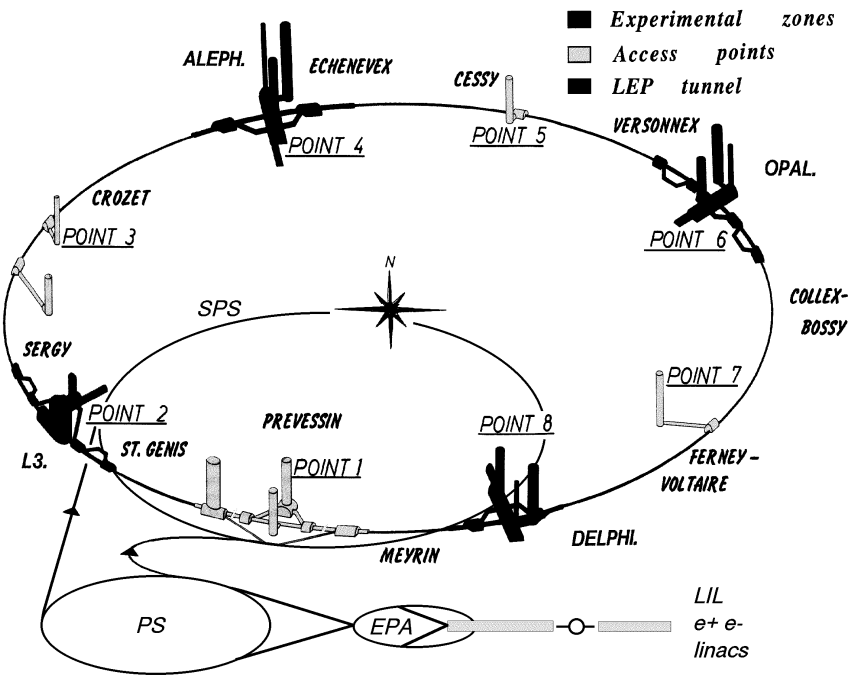

Figure 3.2: The LEP accelerator with its injection system and the four experiments. The towers indicate the access shafts that lead under ground to the experimental areas. The electrons and positrons are produced within the LIL (**L**EP **I**njector **L**inac) and accelerated to an energie of 600 MeV. From there they are injected into the EPA (**E**lectron **P**ositron **A**ccumulator) where they are grouped into bunches for further acceleration within the PS (**P**roton **S**ynchrotron). After reaching an energy of 3.5 GeV within the PS the electrons and positrons are further accelerated within the SPS (**S**uper **P**roton **S**ynchrotron). After they reach an energy of 22 GeV they are injected into the LEP machine.

3.2 The OPAL Detector

The OPAL (**O**mni **P**urpose **A**pparatus at **L**EP) detector is seated at point 6 at the LEP ring. As its acronym indicates, it is a general purpose experiment designed to record all kinds of interactions occurring in electron-positron collisions, for which it has excellent acceptance over nearly the full solid angle of 4π. Figure 3.3 shows its general layout, with dimensions of about 12 m x 12 m x 12 m, making it a considerably large detector.

The coordinate system of OPAL is cartesian, with the x-axis pointing to the centre of LEP, the z-axis following the nominal e^--direction and the y-axis perpendicular on the two other ones. The azimuthal angle ϕ is defined with respect to the x-axis, rotationally symmetric around the z-axis. The polar angle θ is defined with respect to the z-axis and subdivides the detector in a central region with $|\cos\theta| \leq 0.72$ and an endcap region with $|\cos\theta| > 0.72$.

The main elements of the OPAL detector are: a tracking system seated within a solenoidal magnetic field of 0.435 Tesla, which is oriented along the z-axis, a time-of-flight detector, an electromagnetic calorimeter made of lead glass, a hadron calorimeter made of iron and wire chambers, the iron serving as return yoke for the magnet, and muon chambers as the outermost layers. Additionally, a system of detectors placed in the forward region of the detector allows a measurement of the luminosity and ensures the identification of particles emitted at a small angle with respect to the beam line. These elements will be briefly described in the following. Detailed information can be found in [7].

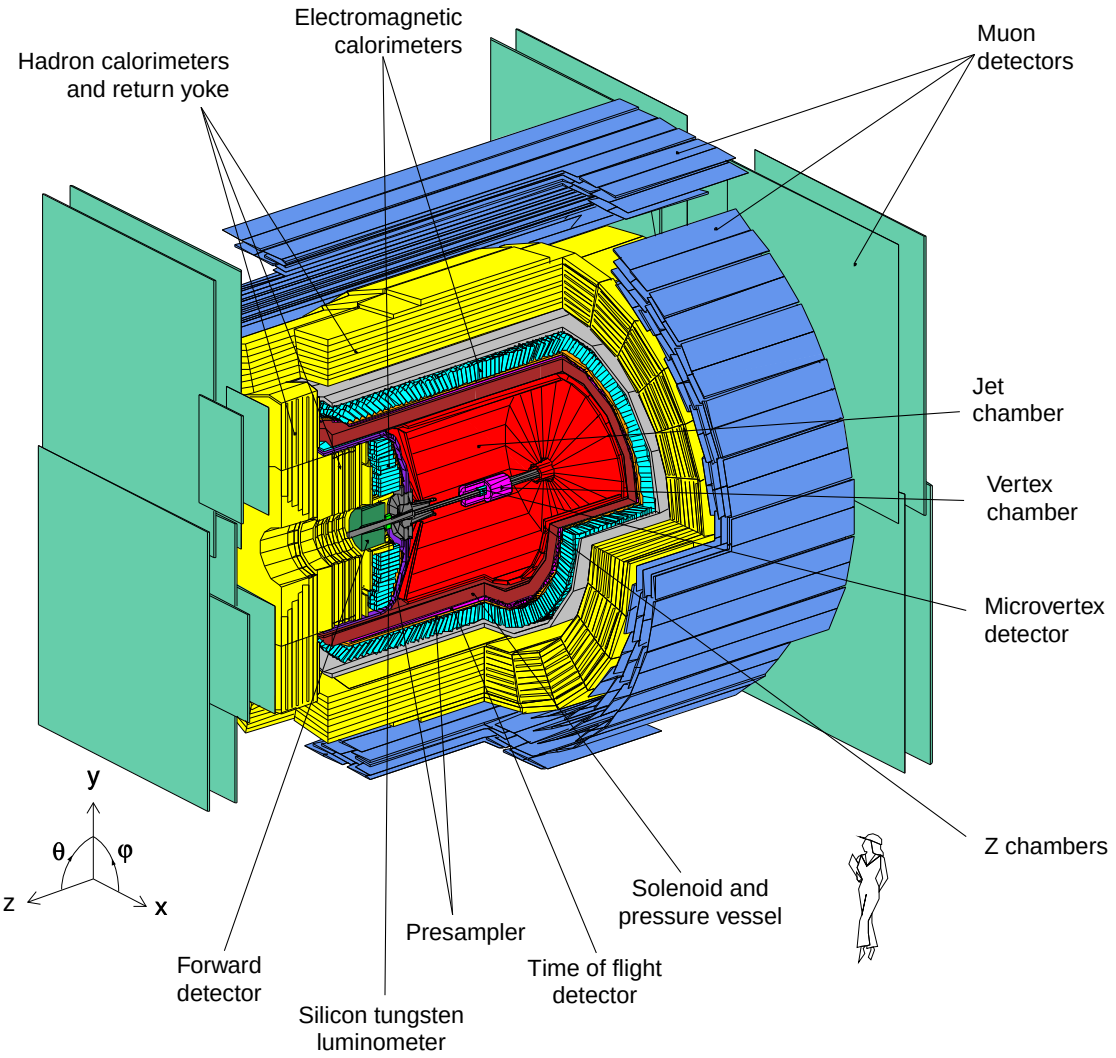

Figure 3.3: A 3-dimensional schematic view of the OPAL detector.

Central Tracking Detectors

The purpose of the central tracking detectors is to measure the tracks, momentum (from the curvature of the tracks inside the magnetic field) and differential energy loss (for particle identification) of charged particles.

A high precision silicon microvertex detector (SI) [8–10] builds the innermost part of the detector, immediately surrounding the beam pipe. The low backgrounds measured during the first LEP1 runs made the radiation damage for such a detector tolerable and the occupancy manageable. It consists of two concentric layers of single sided silicon detector wafers with AC coupled readout strips. After several upgrades it has today a geometrical acceptance of $|\cos\theta| < 0.89$ in the polar coordinate and 97% in the azimuthal angle for two-layer coverage.

Together with the tracking chambers it yields very precise measurements of the position of the primary vertex and, from decays of the resulting short lived particles, secondary vertices.

The Vertex detector (CV) is a cylindrical drift chamber of 1 m in length and 470 mm in diameter. It is operated at 4 bar within the common central tracking pressure vessel adjoining the microvertex detector. It supports the latter in finding secondary vertices and improves the overall momentum resolution of charged particles tracks.

This high precision subdetector is surrounded by a large drift chamber, the Jet chamber (CJ). It consists of 24 identical sectors in ϕ, that are separated by cathode wire planes. In the middle of each sector 159 sense wires are strung parallel to the beam pipe from an inner radius of 255 mm to an outer one of 1835 mm. A mechanical staggering of the wires of +/- 100 μm ensures the track is reconstructed at the correct side of the wire plane. These sense wires are interspaced with 160 potential wires. The Jet chamber is operated at a nominal pressure of 4 bar with a gas mixture of Argon/Methane/Iso-Butane and a few 100 ppm water. The homogeneous magnetic field inside the tracking chambers forces the particles on curved paths. From the radius of curvature the charged particle's momentum can be determined. The differential energy loss dE/dx of the particles can be calculated from a summation of the charge collected at both ends of the wires. For the performance of the OPAL Jet-chamber see [11]. Combination of the measurements of the Jet-chamber, the Vertex detector and the Silicon microvertex detector yields a momentum resolution for Bhabha scattering and muons for all data taken at a centre-of-mass energy of 189 GeV of [12]

$$\frac{\sigma_p}{p^2} = (1.58 \pm 0.02) \cdot 10^{-3}\text{GeV}^{-1}.$$

Z-chambers surround the Jet-chamber to provide a good measurement of the z-coordinate of charged particles which the Jet-chamber is just able to measure with a resolution of 6 cm [7] using a charge division technique. The z-chambers consist of 24 drift chambers covering a polar angle from 44^o to 136^o and 94% of the azimuthal angle.

Calorimeters

While the tracking detectors are low density position measurement devices, calorimeters are total absorption detectors designed to determine the energy of particles.

The electromagnetic calorimeter is built to provide an energy measurement for electrons (positrons) and photons. The main processes occuring when these particles enter the material are, for energies above a few 100 MeV, bremsstrahlung for electrons (positrons) and pair production for photons. Figure 3.4 shows the development of a so-called electromagnetic shower: a photon enters the detector

material and produces an electron-positron pair with an energy of half the photon energy each. After having traversed about what is called a radiation length X_0 of material the probability for the photon to produce such a pair is 54%. In the field of nuclei these newly created particles radiate photons, a process known as bremsstrahlung. This shower process comes to rest when the energy of the particles falls below the *critical energy* and ionisation and excitation occur rather than the creation of new particles.

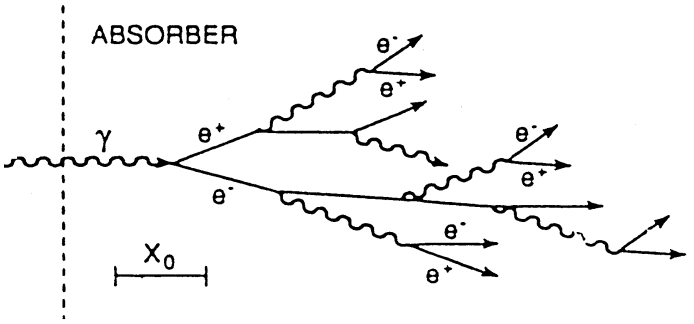

Figure 3.4: Development of an electromagnetic shower [13].

OPAL's electromagnetic calorimeter (ECAL) is a homogeneous detector composed of 9440 (2264) lead glass blocks in the barrel (endcap) region, that correspond to 24.6 (22) radiation lengths. In the barrel part they form a cylinder around the beam pipe, pointing towards the nominal point of interaction. However, they are not perfectly aligned towards the vertex to prevent particles from escaping the detection by travelling through the tiny gap between two lead glass blocks. Photomultipliers are placed behind the lead glass blocks to detect the Čerenkov radiation[1] and thus measure the energy deposited inside the detector. The intrinsic energy resolution for the described assembly is for the barrel part [7]

$$\frac{\sigma_E}{E} \approx 0.2\% + \frac{6.3\%}{\sqrt{E\,[\mathrm{GeV}]}}$$

and for the endcap region (at low energy) [7]

$$\frac{\sigma_E}{E} \approx \frac{5\%}{\sqrt{E\,[\mathrm{GeV}]}}.$$

The actual resolution is degraded due to a few radiation lengths of material in front of the calorimeter (mainly the pressure vessel and the magnet coil). To improve energy and position resolution as well as the π^0/γ and electron/hadron discriminating power of the calorimeters, a set of tubes operated in limited streamer mode, situated in front of the electromagnetic calorimeter, is used as presampling device.

The next outer detector is the hadron calorimeter. If hadrons of energies above about 5 GeV impinge on a block of matter, inelastic as well as elastic scattering will occur between the particles and

[1] Charged particles emit Čerenkov radiation in a cone of halfangle $\theta_{\check{\mathrm{C}}} = \arccos\frac{1}{\mathrm{n}\beta}$ if their velocity exceeds the local phase velocity v of light; n is the refractive index, β=v/c.

the nucleons inside the material. Thus energy is transferred and secondary hadrons are produced, that further collide inelastically. A hadron shower occurs. The basic interaction responsible for the shower development is the strong interaction. In addition, the shower has an electromagnetic component originating mainly from the decay of secondary π^0, as can be seen in figure 3.5.

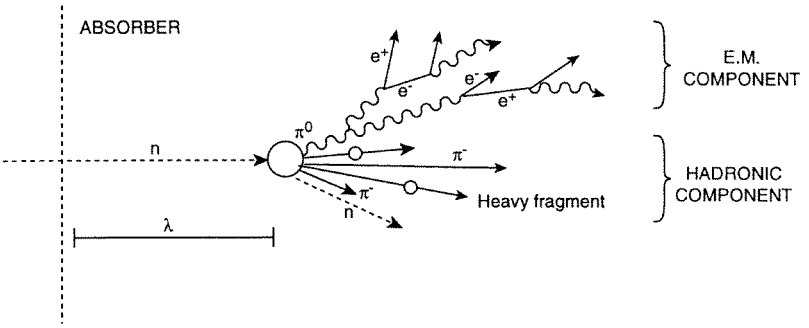

Figure 3.5: Development of a hadron shower [13].

The hadron calorimeter covers 97% of the solid angle and is subdivided in three sections, the barrel, the endcaps, and the pole tips, according to their angular coverage in terms of $|\cos\theta|$ of $0-0.81$, $0.81-0.91$, and $0.91-0.99$ respectively. OPAL's hadron calorimeter is a sampling calorimeter, consisting of layers of active detectors interspaced with iron providing the absorbing material. In the barrel and endcap region wire chambers operated in limited streamer mode are placed between the iron layers, while in the pole tips the active detectors are thin high gain multiwire chambers. The energy resolution is [7]

$$\frac{\sigma_E}{E} \approx \frac{120\%}{\sqrt{E\,[\mathrm{GeV}]}}.$$

The information gained from this detector must be used in combination with the electromagnetic calorimeter since there are about 2 interaction lengths of material before the hadron calorimeter.

The Time-Of-Flight Detector

In the barrel, between the tracking devices and presampler, lies a system of 160 scintillation counters. When a charged particle traverses the counters the molecules inside are excited. Certain molecules release part of their excitation energy in form of optical photons. These photons are then collected at either side of the trapezoidal 6.84 m long counters and passed on, via light guides made of Plexiglas, to photomultipliers which measure the signals .

The main purpose of the time-of-flight detector is to provide trigger signals and aid in the rejection of cosmic rays. Additionally it allows charged particle identification in the range of 0.6 – 2.5 GeV.

In order to enhance the trigger information available from the forward region for LEP2 running, a system of scintillating tiles [14] has been installed between the endcap presampler and the electromagnetic calorimeter.

The Muon Chambers

Muon chambers form the outermost layer of the OPAL detector. They detect charged particles (mainly muons since all others have been already stopped in the calorimeters) mainly against a hadronic background. Hadrons can appear as muons in the chamber if either they fail to interact strongly in the calorimeter, or interact close to the edge of the calorimeter, so that secondary particles escape and fake a muon. The probability of a pion not interacting before entering the muon chamber is less than 0.001, though, as they travel through the equivalent of 1.3 m of iron before reaching the chamber. Decays of pions and kaons to muons can also occur, but combining the spatial information of the muon chamber with the tracking detectors helps to identify whether one is dealing with an initial muon.

The barrel part of the muon system consists of 110 drift chambers, while the endcaps consist of tubes operated in limited streamer mode. The angular coverage in $|\cos\theta|$ is for one layer operation 0.72, for 4 layers 0.68. The endcaps cover the region between 0.67 and 0.98.

Forward Detector and Silicon Tungsten Luminometer

The forward detector is designed to detect particles that leave the interaction point under a low angle with respect to the beam pipe.

It mainly consists of a calorimeter that together with tube and drift chambers is able to measure the luminosity via low angle Bhabha-scattering. The calorimeter is made of 35 layers (24 radiation lengths) of lead alternating with scintillators. It has an energy resolution of

$$\frac{\sigma_E}{E} \approx \frac{17\%}{\sqrt{E\,[\mathrm{GeV}]}}.$$

The tube chambers are operated in proportional mode.

In 1991 the decision was taken to build a more precise luminosity monitor. As the data recorded at the Z^0 resonance accumulated with the high statistics, the uncertainty in the luminosity measurement became a limiting factor for the systematic error of cross-section measurements. The silicon tungsten luminometer is a sampling calorimeter consisting of layers of silicon detectors and tungsten absorbers. It was first operated in 1993. See [15] for the precision of the luminosity measurement for Z^0 lineshape measurements with this detector.

Trigger

At four on four bunch operation of LEP, the bunch crossing rate within the OPAL detector is 22 μs. The purpose of the trigger is to pick the true events occuring from e^+e^- collisions with high efficiency out of background arising from cosmic radiation, noise or interactions of particles with either the evacuated beam pipe itself or the few remaining gas atoms, while keeping the trigger rate low enough for the Data Acquisition system to handle.

Most subdetectors provide inputs to the trigger decision, comprising a “track trigger”, a time-of-flight trigger, calorimeter triggers, a muon detector and forward detector trigger.

The trigger signals are twofold. Information from single detector components serves as a direct trigger signal. These signals, such as total energy, have generally rather high thresholds.

The heart of the trigger remains the so-called “theta-phi matrix”. It has 24 bins in phi and 6 in theta and looks for spatial association of two input signals, either from different subdetectors in the same bin in theta-phi or two inputs from a single subdetector that are back-to-back in theta-phi. For further information see [16, 17].

Online Dataflow

Once the trigger logic decides that an event might contain interesting physics, each subdetector is read out separately. The information of all subdetectors is then combined by the so-called event-builder and sent to the filter [18], a processor that performs a fast preselection of events, for instance a further rejection of cosmic events. From the filter the data are written to files and reconstructed as soon as the required calibration constants are available. These reconstructed data are in a form that allow their use in offline analysis.

3.3 The Simulation and Reconstruction Chain

The electrons and positrons accelerated in several steps to their peak energy are brought into collision with the LEP accelerator inside the four detectors. All kind of collisions occur and are recorded by these detectors. This analysis performs a search for new particles, namely for the neutral Higgs bosons h and A as they appear in models with two scalar Higgs field doublets. All Standard Model processes occuring e^+e^- collisions constitute background for searches for new particles. Therefore, it is crucial to know which kinds of processes one has to expect from the Standard Model predictions at the energy and type of accelerator that is used, as well as the rate at which they occur and how they appear in the detector. Nowadays, in high energy physics, Monte Carlo simulation plays a very important role. It provides a way for the theory to enter the experiment. To investigate which signature a certain signal or background process will show in the detector, the Monte Carlo events have to go through a chain of simulations. Finally, these processed events, as well as the raw data enter the same reconstruction routines, that build tracks and energy clusters out of all detector components that responded to the events (in real or simulation). In the first step of the simulations, signal and background events are generated with the Monte Carlo generator designed for the specific type of events. That means that the 4-vectors of the particles contained in these events are produced, taking into account the momentum and energy of the initial electron and positron, as well as model parameters for the process under investigation. The newly created 4-vectors are then input to a routine simulating the passage of the particles through the detector, their interactions with the detector material and the production of secondary particles, as well as the energy deposit in the several detector cells. The program package in use for that is GEANT [19]. The simulation package GOPAL [20], which itself uses GEANT routines, then simulates the detector response to these energy deposits and delivers the simulated raw data. These enter just as the real data the event reconstruction software ROPE [21], which reconstructs tracks and clusters from the data collected with the subdetectors.

Chapter 4

Background Processes and their Simulation

As discussed previously in chapter 3.3, it is crucial to understand which background processes occur in an experiment when searching for new physics. Figure 4.2 shows the cross sections of the most important Standard model processes in the energy range of LEP2. The background processes for this analysis arise from 2-fermion and 4-fermion production.

4.1 2-fermion Processes

Two fermion processes (figure 4.1) arising from Z^0 decays have been studied extensively and precisely at LEP1. At higher energies, moving away from the Z^0 resonance, the cross section for Z^0 production

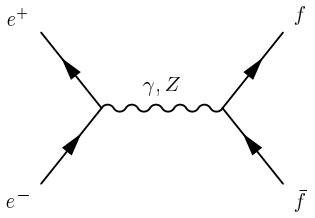

Figure 4.1: Feynman diagram for fermion pair production.

becomes rapidly smaller while the photon exchange becomes important. A new feature at LEP2, that has to be taken into account, is the large correction to the cross section due to initial state radiation (ISR), i.e. the emission of photons by the incoming electrons and positrons just before the collision. At LEP1 energies hard photon emission is inhibited, while soft photon radiation reduces the cross section at the Z^0 resonance. At LEP2 the rapidly decreasing cross section favours the emission of hard photons, so that the remaining energy, carried by the electron and the positron, is close to the Z^0 mass. This process is therefore referred to as a *radiative return*. The Feynman diagrams for such processes are shown in figure 4.3. The convolution of the ISR photon spectrum with the e^+e^- Born cross section leads to a significant enhancement of the cross section, as can be seen in figure 4.4, which shows the cross section for the process $e^+e^- \to \mu^+\mu^-$ compared to the pure Born cross section. From figure 4.2 it can be seen, that, taking initial state radiation (denoted $\Sigma q\bar{q}(\mathrm{ISR})$) into account the cross section for Z^0 production remains dominant over WW production even at higher energies. As

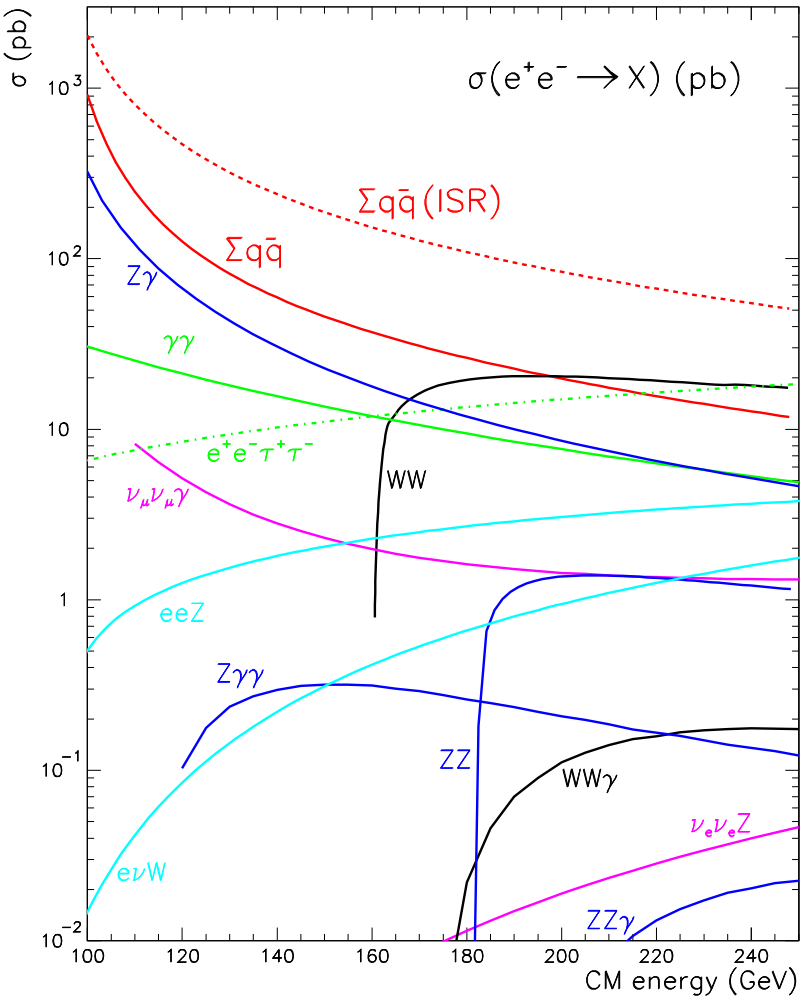

Figure 4.2: Cross-sections of the most important Standard Model processes; for $e^+e^-Z^0$, $\nu_e\bar{\nu}_eZ^0$ and $e^\pm\nu_eW^\mp$ only the dominant t-channel contribution is shown.

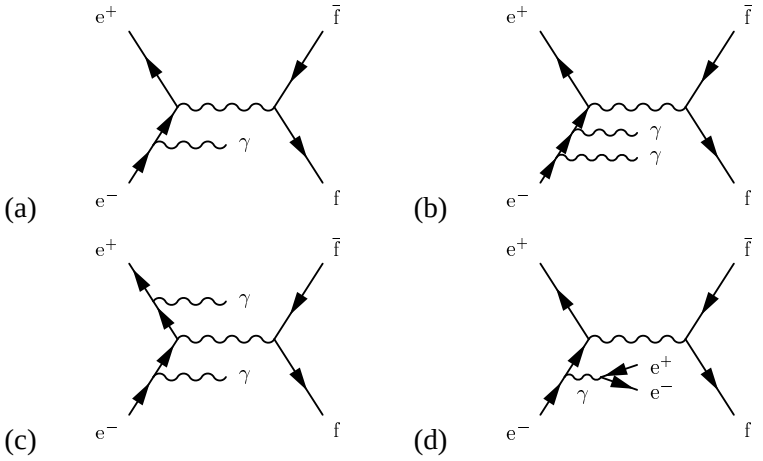

Figure 4.3: Feynman diagrams for fermion pair production with (a) single photon radiation, (b-c) double photon radiation and (d) photon conversion into an e^+e^- pair.

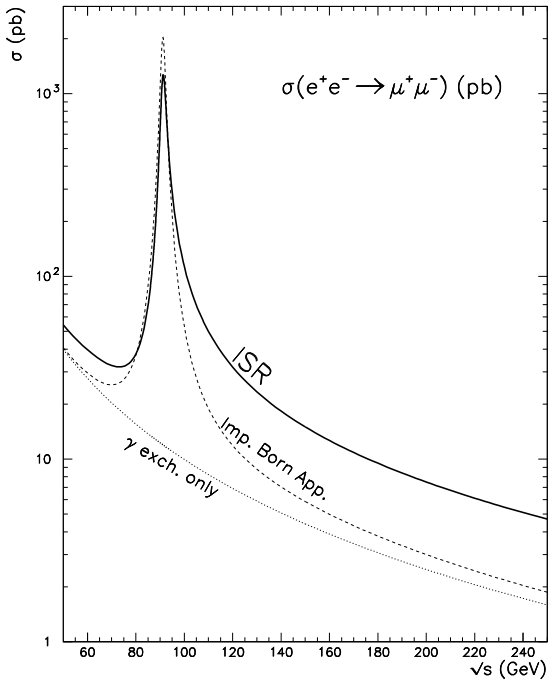

Figure 4.4: The $e^+e^- \rightarrow \gamma/Z^0 \rightarrow \mu^+\mu^-$ cross section before (dashed line) and after the ISR convolution (solid line) [6]. The dotted line shows the cross section for the mediation of this process via a photon only.

this analysis searches for a signal in hadronic final states, the main background contribution of the 2-fermion processes arises not from lepton-pair production, but from quark-pair production. Signal events can be faked through multiple hard gluon radiation in $e^+e^- \rightarrow q\bar{q}$ events which results in more than 2 jets in the final state. The Feynman diagrams for such processes can be seen in figure 4.5, where one or more gluons are radiated by the quarks, producing themselves further gluons or convert to quark-antiquark pairs. Events arising from quark-pair production will in the following be referred to as Z/γ events (even if they just make the hadronic part of this event class) or simply as QCD events.

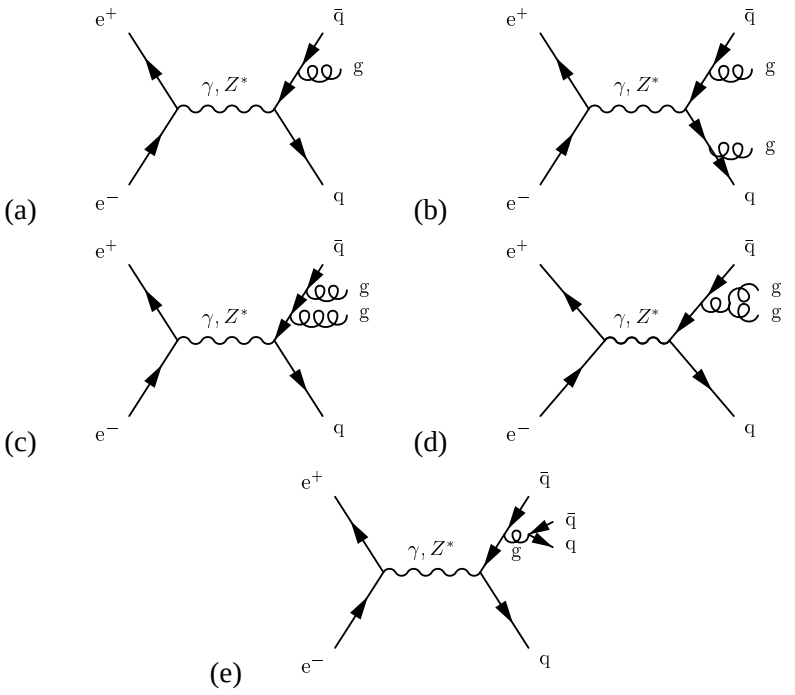

Figure 4.5: Feynman diagrams for quark pair production with hard gluon emission.

4.2 4-fermion Processes

The most significant background for the analysis presented in this thesis—a Higgs search in the hadronic channel—originates from decays of W and Z pairs. At LEP2, the centre-of-mass energy is higher than the threshold energy necessary for the double resonant production of real W and Z boson pairs. In the case where the W and Z boson decay hadronically, the final state observed in the detector has the same topology as the expected signal, namely 4 jets.

The WW and ZZ production belongs to the larger class of 4-fermion processes. Figure 4.6 shows all possible lowest order Feynman diagrams for 4-fermion processes; the diagrams can be classified as Abelian (a-d) and non-Abelian (e and f). The non-Abelian diagrams include a triple gauge boson vertex.

The WW and ZZ processes are described by the Conversion (fig. 4.6 (d)) and non-Abelian Annihilation diagram (fig. 4.6 (e)). Of the 4-fermion processes, the multiperipheral diagrams (fig. 4.6 (c)), have the most sizeable cross section. In this class, two quasi-real photons are exchanged in the

t-channel, together with a non-resonant fermion-antifermion pair, so that these reactions are often referred to as two-photon processes. However, with forward (and often undetected) electrons and positrons, they are a negligible background for Higgs searches with hadronic final states.

Abelian classes:

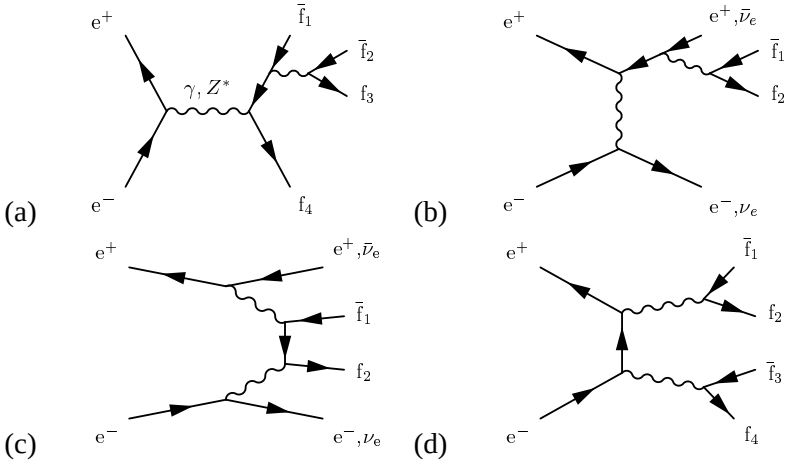

Non-Abelian classes:

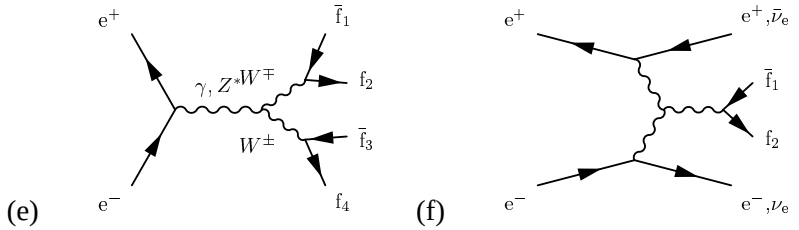

Figure 4.6: Feynman diagrams for four-fermion production; the inner vector boson lines may correspond to γ, Z^0, or $W^{\pm}$ exchange, unless otherwise indicated. The diagrams are referred to as (a) Annihilation, (b) Bremsstrahlung, (c) mulitiperipheral diagrams, (d) Conversion, (e) Annihilation and (f) Fusion. Bosons in (a) and (b), originating from outgoing fermion lines, can also be emitted by incoming fermions.

4.3 Monte Carlo Simulation

Standard Model Background

- 2-fermion processes have been simulated with the PYTHIA [22] generator.
- 4-fermion processes have been simulated with the `grc4f` [23] generator, which takes into account possible interferences between different classes of 4-fermion diagrams.

Hadronisation

The hadronisation of the initial partons has been modelled by JETSET [24] which uses the Lund-String-Fragmentation. The parameters of the JETSET program used within the OPAL collaboration

have been extensively tuned to LEP1 $e^+e^- \rightarrow Z \rightarrow qq$ data. JETSET thus provides a very good description of hadronic final states as they are observed with the detector.

Signal

The features of the signal processes will be explained in chapter 6, after the introduction of some common tools of high energy physics analyses. The generator HZHA [25] was used for their creation. The modelled background and signal events are subject to the same analysis as the data.
For further details on Monte Carlo samples used in this analysis see appendix C.

Chapter 5

Analysis Tools

In the following a few general tools applied in the analysis will be explained. As this analysis focusses on hadronic final states of the decaying Higgs bosons h and A, as a first step hadronic events are selected.

5.1 Multihadron event selection

Higgs bosons can decay into all massive particles and gauge bosons as long as a certain decay channel is not forbidden by conservation laws. This analysis concentrates on the case where the neutral Higgs Bosons h and A are produced as a pair and then decay into either quark-antiquark pairs or gluons. As explained above, this leads to hadrons as detected particles. Events of this type are referred to as fully hadronic events, as no primary leptons are produced in the decay of the h and A bosons.

Before the events enter the actual analysis they have to pass some general quality criteria. The efficiency of these quality criteria is almost 100% for the class of events under investigation. The quality requirements defining what is thought to be a good track or cluster can be found in detail in [26].

To finally select hadronic events the following requirements are used:

- an event should have at least 7 good clusters and 5 good tracks (they are asked to have high multiplicity in order to reduce background from leptonic final states)
- the total energy deposit in the electromagnetic calorimeter should exceed 14% of the centre-of-mass energy (to reduce background from two photon events[1].)
- the energy balance along the beam direction:

  $$R_{bal} \equiv |\Sigma(E_{clus}\cos\theta)|/\Sigma E_{clus} < 0.75.$$

  This reduces any remaining background from beam-gas and beam-wall interactions and helps in a further reduction of two-photon events.

This multihadron event selection has an efficiency of about 99 % for events with four quarks in the final state.

[1]Processes where two quasi-real photons are exchanged in the t-channel, giving rise to usually undetected forward electrons and positrons plus a fermion pair with a non-resonant structure, see fig. 4.6(c)

5.2 Event Reconstruction Tools

5.2.1 Energy Correction

The energy and momentum of jets is derived from the combined information of the central tracking system and the calorimeters. However, one has to avoid *double counting* of the momenta of charged particles, as they leave a track in the tracking devices as well as energy deposits in the calorimeters.

About 2/3 of the total energy in a hadronic final state is carried by charged particles, which are usually measured with better momentum and angular resolution in the central tracking system. The energy of neutral particles, on the other hand, can only be measured in the calorimeter system.

Thus, to obtain the best jet energy resolution, the energy information for charged particles should be taken from the central tracking detectors and combined with the calorimeter information of the neutral particles. Unfortunately the calorimeter granularity is not sufficient to separate the charged and neutral particles of a jet, as they are intermixed in a very narrow space region. To use the energy information from the calorimeters for the neutral particles, the contribution of the charged particles in the same calorimeter cluster has to be removed.

The *Matching Algorithm* [27–29] provides a very sophisticated way of correcting the energy of calorimeter clusters for charged particles. In addition, it also implements compensations for the different responses to hadrons of the electromagnetic and the hadronic calorimeters in OPAL and thus further improves the energy and momentum resolution of jets. Usually, hadrons already begin to interact within the ECAL and deposit part of their energy. However it is also possible that hadrons penetrate the ECAL without strong interactions and deposit their full energy only in the HCAL. This scenario is further complicated by the fact that only the electromagnetic part of the hadronic shower (compare section 3.2) can be measured in the ECAL. Simply adding the energies of the electromagnetic and hadronic calorimeter clusters would underestimate the energy of the hadron and lead to a bad resolution.

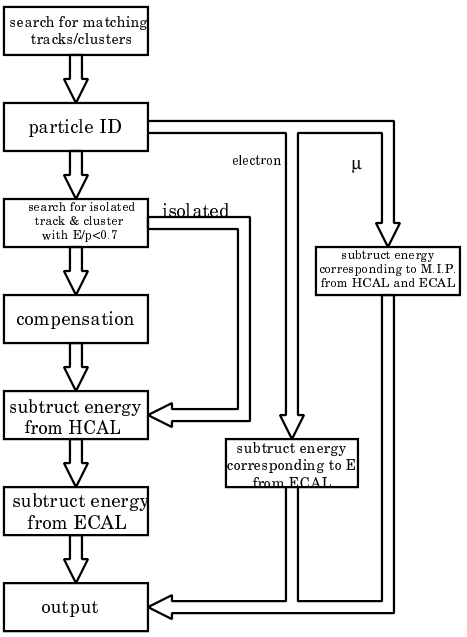

Figure 5.1: Schematic diagram ot the matching algorithm to measure the energy flow [29].

A flow diagram of the *Matching Algorithm* is shown in figure 5.1. The algorithm initially matches tracks to calorimeter clusters by using the extrapolated track to the electromagnetic or hadronic calorimeter and taking into account the cluster center and boundaries as well as the energy of the cluster and the expected calorimeter response as calculated from the track momentum. The identity of the particles of the matching tracks is then determined, as electrons and muons have to be treated differently from hadronic particles by the algorithm in the energy compensation stage. The separate treatment of leptons is especially important for analyses concerning the search for Higgs bosons, as jets originating from the decay of Higgs bosons often contain leptons from the decay of b- and c-mesons. In the case of an electron, the energy as measured in the tracking chambers is subtracted from the associated calorimeter clusters. In the case of a muon, the energy that a Minimum Ionising Particle (MIP) of the measured momentum would deposit in the calorimeters is subtracted. The *Matching Algorithm* continues by locating isolated tracks and clusters which are likely to originate from a photon conversion or a single pion that interacts in the ECAL and deposit a large amount of its energy before reaching the HCAL. In these cases the cluster energies are not compensated, since for photon conversion the ECAL cluster corresponds to an electromagnetic shower which is measured correctly, and for the pion the energy is calculated from the track momentum. The energy of all remaining non-isolated clusters which have a matching hadron track is then compensated for the different response of the electromagnetic and hadronic calorimeter. After this compensation the cluster energies are corrected for double counting by subtracting the energy of the matching tracks. The energy correction starts at the HCAL and only if the energy deposit there is not large enough the ECAL energy is corrected by the missing amount. After this correction, the cluster energies should have their origin only in photons and neutral particles. For Z^0 data, an energy resolution for the visible energy in the barrel region for mulithadronic events of 8.6 GeV is reached.

5.2.2 Jet Finding

Due to the hadronisation of the quarks created in the e^+e^- collisions and decays of other primary or secondary particles, more particles are measured in the detector than initially produced. To estimate the invariant masses and four-vectors of the initially created particles all the tracks have to be combined somehow to a certain number of so-called jets.

There are several iterative combination algorithms, often referred to as jetfinders, to accomplish this goal. This analysis uses the DURHAM jetfinder [30,31] with a reassociation procedure as described in [32].

The starting point for the DURHAM Algorithm are all particles observed in the detector. They are taken as initial objects entering an iterative procedure. For every possible pair (k,l) of these particles the scaled minimal transverse momentum of the less energetic particle with respect to the more energetic one, defined as

$$y_{kl} = \frac{2\min(E_k^2, E_l^2)(1-\cos\theta_{kl})}{E_{vis}^2}, \tag{5.1}$$

is calculated. E_k and E_l are the energies of the two particles, θ_{kl} is the angle between their momentum vectors and E_{vis} is the total visible energy of all final state particles. The two particles with smallest y_{kl} are combined to a new *pseudo-particle* by summing up their four-vectors if y_{kl} is smaller than a certain resolution parameter y_{cut}. Once all combinations yield values larger than y_{cut} the procedure is stopped and the remaining *pseudo-particles* are referred to as jets. Every event can be forced to any number of jets equal or smaller than the number of initial final state objects. A smaller number

of jets is achieved by gradually increasing the value of y_{cut}. The value of y_{cut} where the number of jets switches from $n+1$ to n is usually referred to as $y_{(n+1)n}$. A large value of $y_{(n+1)n}$ indicates good separation between the remaining $n+1$ jets.

After a predefined number of jets has been found with the DURHAM algorithm, their direction is taken as a starting point for a reassociation procedure. Every particle, that left a track or energy cluster in the detector, is associated to the jet with the shortest distance defined via

$$D^{E0}_{i,j} \equiv 2E^{jet}_i \cdot E^{j}_{particle} \cdot (1-\cos\Theta_{ij}).$$

This distance is referred to as Jade E0 distance, as in the JADE jet finding algorithm [33, 34] y_{kl} is calculated as

$$y^{JADE}_{kl} = \frac{2E_kE_l(1-\cos\theta_{kl})}{E^2_{vis}}. \tag{5.2}$$

5.2.3 Event Shape Variables

At high energies the charged particle multiplicity is rather large (at LEP and a centre-of-mass energy of 189 GeV the mean multiplicity for 4 quark events yields about 38 charged particles per event [35], at Hadron Colliders significantly more). To quantify the topology of an event, how the tracks are distributed over the detector volume, a few event shape variables have been introduced. The analysis makes use of the so-called C-parameter, which is defined as

$$C = 3(\lambda_1\lambda_2+\lambda_2\lambda_3+\lambda_3\lambda_1). \tag{5.3}$$

The $\lambda'_\alpha s$ ($0 \leq \lambda_\alpha \leq 1, \Sigma_\alpha\lambda_\alpha = 1$) are the eigenvalues of the linearized momentum tensor

$$\Theta^{\alpha\beta} = \frac{\Sigma_i \mathbf{p}^\alpha_i \mathbf{p}^\beta_i/|\mathbf{p}_i|}{\Sigma_j|\mathbf{p}_j|}. \tag{5.4}$$

The sums go over all observed particles. The possible values for this so defined C-parameters range from 0 to 1. Here C = 0 indicates a perfectly two-jet-like final state (pencil shaped) and C = 1 an isotropic distribution of the final-state momenta. Further information on the C-variable can be found in [36, 37].

5.2.4 Kinematic Fits

The correct determination of energy and momentum of hadronic jets is a very important issue, for instance to reconstruct the invariant mass of jets with an optimal resolution. Even after the energy correction described in chapter 5.2.1 is applied, the invariant mass distributions are broadened as the detector resolution is not infinitely small and the energy and momentum of the final state hadrons are reconstructed without using additional physical information such as overall energy and momentum conservation. It is however possible to exploit such information by applying kinematic fits based on the method of least-squares. In this method, features like energy and momentum conservation can be implemented by Lagrange multipliers to derive improved estimates for the 4-momenta of jets. The underlying principles and some features of a particular sampling distribution, the Chi-Square distribution, are briefly reviewed. A more detailed treatment of this subject can be found in [38].

The Chi-Square Distribution

Given a set of measured values $x_1, x_2, ..., x_n$, that are mutually independent random variables and normally distributed with the mean values μ_i and the variances σ_i^2. Then the sum of the squares of the standardized normal variables $(x_i - \mu_i)/\sigma_i$

$$\chi^2 \equiv \sum_{i=1}^{n} \left(\frac{x_i - \mu_i}{\sigma_i} \right)^2 \tag{5.5}$$

is called the chi-square sum χ^2. The probability density function of this variable χ^2 is given by

$$f(\chi^2, n) = \frac{1}{\sqrt{2^n}\Gamma(\frac{1}{2}n)} (\chi^2)^{\frac{1}{2}n-1} e^{-\frac{1}{2}\chi^2} \tag{5.6}$$

and referred to as chi-square distribution with n degrees of freedom, the number of degrees of freedom being the number of independent variables making up the chi-square sum. The gamma function Γ is defined via $\Gamma(x+1) = x\Gamma(x),\ \Gamma(\frac{1}{2}) = \sqrt{\pi},\ \Gamma(1) = 1$.

A useful quantity for the following application of kinematic fits is the cumulative chi-square distribution

$$F(\chi_\alpha^2; n) \equiv \int_0^{\chi_\alpha^2} f(\chi^2; n)\, d\chi^2 = 1 - \alpha. \tag{5.7}$$

$F(\chi_\alpha^2; n)$ is uniform over the interval [0,1], as any variable defined by the cumulative integral of a probability density function (see [38]).

The Least-Squares method

Given a set of N independent measured values $x_1, x_2, ..., x_N$, with true values, that are unknown, but predicted by some theoretical model and related to the measured values through some functional dependence

$$f_i(\lambda_1, \lambda_2, ..., \lambda_L; x_i) = 0,\ L \leq N,$$

then the Least-Squares Principle including the Lagrangian multipliers λ_k states that the best estimates $x_1', x_2', ..., x_N'$ of the unknown parameters are those which minimize

$$\chi^2 = \sum_{i=1}^{N} \left(\frac{x_i' - x_i}{\sigma_i} \right)^2 + \sum_{k=1}^{L} \lambda_k f_k(x_1', x_2', ..., x_N'). \tag{5.8}$$

In the case of the measurement of correlated variables $x_1, x_2, ..., x_N$ this expression changes to

$$\chi^2 = \sum_{i=1}^{N} \sum_{j=1}^{N} (x'_i - x_i) V_{ij}^{-1} (x'_j - x_j) + \sum_{k=1}^{L} \lambda_k f_k(x_1', x_2', ..., x_N') = \text{minimum}. \tag{5.9}$$

Herein V denotes the symmetric covariance matrix of the measured variables. The equations of constraints are automatically fulfilled in the minimum, $f(x') = 0$. In the case of the x_i being 4-vectors of jets for instance, the constraints f_k can contain the requirement of energy and momentum conservation, or the assumption that a certain dijet combination results in a given invariant mass.

Goodness-of-fit

A very important feature of the method of Least-Squares is that the distribution of the χ^2_{min} is known if the number of degrees of freedom is known. The number of degrees of freedom is given by the number of measurements minus the number of fitted parameters plus the number of constraints. That means that a measure for the goodness-of-fit can be derived from the value of the χ^2_{min} by calculating the fit-probability

$$P_{\chi^2} = \int_{\chi^2_{min}}^{\infty} f(\chi^2; n) d\chi^2 = 1 - F(\chi^2_{min}; n). \tag{5.10}$$

$F(\chi^2_{min}; n)$ is the cumulative chi-square distribution of equation (5.7). The chi-square probability gives the probability for obtaining a higher value of χ^2_{min} in a new minimization within the same model and similar measurements. If the errors contained in V are correctly estimated and the data obey the constraints, the distribution is uniform between zero and one.

Implementation of Fits in Analyses

Kinematic fits are an important tool in physics analyses. In this analysis they are used in two ways. A kinematic fit imposing energy and momentum conservation is applied to find better estimates for the 4-momentum of jets. It is referred to as 4C fit, as there are four equations of constraint, one from energy conservation and the remaining three from momentum conservation in all directions. The fit-probability of such a 4C fit can be used to identify poorly reconstructed events. For such events the errors are not correctly estimated, so that the chi-square probability peaks at lower values instead of being distributed uniformly.

In addition, the fit-probability can be used to discriminate between different classes of events. For instance, a fifth constraint can force the invariant dijet masses to be equal. For events where two particles with the same masses are produced, the fit-probability should be uniformly distributed. For data that do not obey this constraint, the fit-probability will have a pronounced peak at low values which helps to distinguish between different classes of events.

5.3 Signal Discrimination based on Likelihood Techniques

A standard task in high energy physics is to extract a signal from a large number of background events. The traditional technique for that is to find variables that discriminate between signal and background and then to find a value (so-called cut) for each such variable that separates most part of the signal events from a large fraction of the background events. In some searches for new particles however, finding appropriate cuts, i.e. cuts that reduce the number of background events while leaving most signal events, is rather difficult. As well cut-based methods do not take probabilistic effects into account: it does not matter, whether an event will fail one cut or several, while we would certainly agree that an event that fails all cuts is more likely to be a background event than an event that just fails a single cut. New methods that do take the probabilistic nature of events into account are such as artificial neural networks, Fisher discriminants and the likelihood method.

The goal is to separate N_{class} classes of different events, but considering N_{var} different variables, in a way described in the following: Each of the variables i will be distributed in each class j according to a certain probability density function $f_i^j(x_i)$, where x_i is the measured value of the variable i in an individual event. This probability density functions are usually taken from fully simulated Monte Carlo events.

If each event belongs to exactly one of the N_{class} classes, for a single variable the probability that an event belongs to class j is given by

$$p_i^j(x_i) = \frac{f_i^j(x_i)}{\sum_{j=1}^{N_{class}} f_i^j(x_i)}. \tag{5.11}$$

The likelihood function for each class j is then formed as the normalized product of $p_i^j(x_i)$, combining the information of several variables, to:

$$L^j(\vec{x}) = \frac{\prod_{i=1}^{N_{var}} p_i^j(x_i)}{\sum_{j=1}^{N_{class}} \prod_{i=1}^{N_{var}} p_i^j(x_i)}, \tag{5.12}$$

where $\vec{x}$ denotes the event vector, consisting of all measured x_i. $L^j(\vec{x})$ takes values between 0 and 1. It can be used to classify to which class j an event belongs to by requiring that its value of the likelihood function for this particular class exceeds some cut value. The probability functions entering the likelihood function should be normalized. Thus, being a normalized product of probabilities, the likelihood function itself is a joint probability, only if the variables entering are uncorrelated. This is not true in practise and one should keep in mind not to think of the likelihood function as a true probability. However, this does not spoil its discrimination power between several classes of events.

For an actual analysis, it would be sufficient to discriminate between two classes: signal and background. It is sensible though to take different properties of different kinds of background into account by choosing more than one background class. In this analysis three classes are used and instead of setting a cut at a certain value, the discrimination power of the likelihood function is used by taking it as an input for limit settings as no excess of events above the expected Standard Model background has been observed in the data. The normalised probability functions will in the following be referred to as reference distributions.

Chapter 6

Analysis in a 2HDM Framework

6.1 Introduction

This analysis performs a search for the neutral Higgs Bosons h and A as they would occur in the type II of two Higgs Doublet Models. Their discovery would be a clear indication of a non-minimal Higgs sector.
The analysis is based on data of an integrated luminosity of approximately 172 pb^{-1}, collected with the OPAL detector at a centre-of-mass energy of about 189 GeV. At LEP2, the main production mechanisms for neutral Higgs Bosons are Higgs-strahlung (where the CP-even scalar h is radiated off the virtual Z-Boson line) and pair-production. Figure 6.1 shows the Feynman diagrams for these processes. They are complementary in the sense that the production cross section for Higgs-strahlung

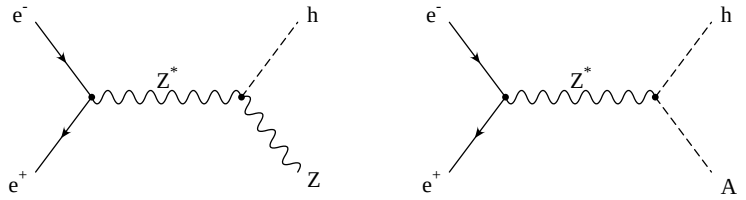

Figure 6.1: Production mechanisms for neutral higgs bosons: Higgs-strahlung on the left and pair-production on the right.

is proportional to $\sin^2(\beta-\alpha)$ while the one for pair-production is proportional to $\cos^2(\beta-\alpha)$ (see chapter 2.2.1); α denotes the weak mixing angle in the CP-even sector and $\tan\beta$ the ratio of the two vacuum expectation values of the Higgs fields. This analysis focuses on the latter process where the h is produced together with the CP-odd Boson A.

The search for this process $e^+e^- \rightarrow hA$ has been performed for the final states $h, A \rightarrow qqqq, ggqq$ and gggg. The Feynman diagrams for these processes can be seen in figure 6.2.

For the minimal Higgs boson, as well as over a large range of values for $\tan\beta$ and α in models with two Higgs doublets, the decay to b-quarks is predominant as Higgs bosons couple proportional to mass:

$$Br(ZH \rightarrow q\bar{q}b\bar{b})_{SM} = 58\% \text{ ([1])} \qquad Br(hA \rightarrow b\bar{b}b\bar{b}) = 83\% \text{ ([6])}.$$

Therefore (and as W-bosons cannot decay into b-quark pairs) most standard analyses rely on b-quark

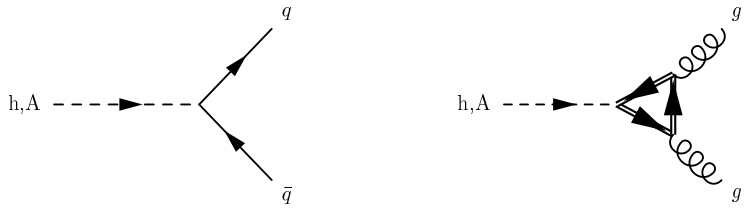

Figure 6.2: Possible hadronic decay modes of the neutral Higgs bosons h and A. The graph on the left-hand side shows the decay of h and A to a quark-antiquark pair, the graph on the right-hand side shows the decay of the bosons into gluons via a quark loop.

specific information, the so-called b-tagging.

However, there are certain regions where the decay rate for h or A to $b\bar{b}$ drops to zero. This can be understood by looking at the couplings for h and A to $c\bar{c}$ and $b\bar{b}$, which are the heaviest up and down type quarks respectively that can be created at LEP2 energies. The couplings are shown relative to the canonical Standard Model values $-im_f(\sqrt{2}G_F)^{\frac{1}{2}}$

$$\begin{aligned} \mathrm{hc\bar{c}} &: \frac{\cos\alpha}{\sin\beta} & \mathrm{hb\bar{b}} &: \frac{-\sin\alpha}{\cos\beta} \\ \mathrm{Ac\bar{c}} &: \cot\beta & \mathrm{Ab\bar{b}} &: \tan\beta. \end{aligned} \tag{6.1}$$

The couplings depend strongly on the values for α and β, so that for instance for α equal to zero the decay of h to b-quarks is forbidden. Figure 6.3 illustrates the behaviour of the branching ratios for certain choices of the parameters $m_{\mathrm{h}}, m_{\mathrm{A}}, \tan\beta$ and α.

In regions where the decay to b-quarks is suppressed or even drops to zero, the standard analyses are not sensitive to a signal from the decay of neutral Higgs bosons. Therefore the analysis performed in this thesis makes no use of any b-quark specific information. Indeed it makes no use of any 'flavour'-specific information, so that it can be used for a search in all regions of the parameter-space. However, because of the high separation power of variables based on a b-tag against the background from WW production, analyses that make use of information from b-quarks will have more sensitivity in regions where the decay to b-quarks is not suppressed.

6.2 Signal and Background Features

The actual topology of the signal events depends on the masses m_{h} and m_{A}. However, in the hadronic channel the signal events have the common features that they contain four more or less distinct jets and little or no missing energy and momentum. This signature makes it rather difficult to distinguish signal events from hadronic final states resulting from the decay of two pair-produced W or Z bosons, which can similarly produce four jets with little or no missing energy and momentum. A second problem is caused by the fact that most event-shape variables have different distributions for different masses m_{h} and m_{A}, as will be shown later. Therefore, treating all these masses with search techniques such as the likelihood function in the same way will not provide sufficient discrimination between signal and background over the whole mass-range. To build the likelihood function, a set of variables are found to discriminate between signal and background. The distributions of these variables are (after they have been normalized) input to the likelihood function. If now the signal distributions differ from mass-point to mass-point, still one distribution has to be chosen as input. If it is taken

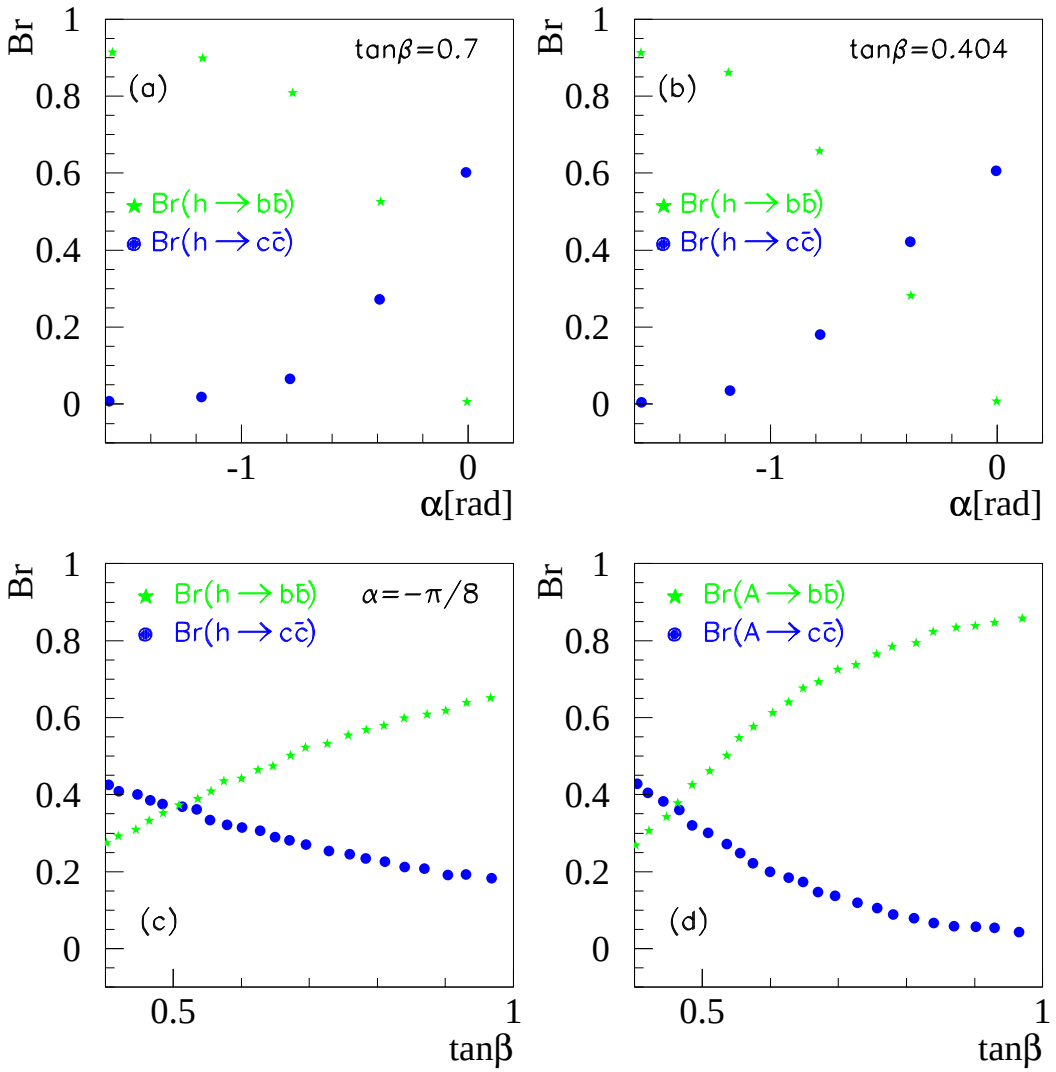

Figure 6.3: Branching ratios for h, A to $c\bar{c}$ and $b\bar{b}$ versus the model parameters α and $\tan\beta$. All figures are shown for $m_A = 40$ GeV and $m_h = 60$ GeV. (a) shows how the branching ratio of h to $b\bar{b}$ drops to zero when α approaches zero. With lower values of $\tan\beta$ this behaviour is even more pronounced (b). In (c) the branching ratios of h to $c\bar{c}$ and h to $b\bar{b}$ are shown for $\alpha = -\pi/8$. For $\alpha = 0$ one would just see a straight line at 0 for $h \to b\bar{b}$, independent from the value of $\tan\beta$. Figure (d) finally shows the behaviour of the branching ratio for A to $c\bar{c}$ as well as to $b\bar{b}$. This behaviour is independent from the choice of the model parameter α.

from one specific mass it will be optimal for just this mass. Other masses might not at all look like a signal when tested under this mass hypothesis.

Therefore it has been decided to develop a mass-dependent analysis. The reference distributions for every mass-point that is tested are then its own distributions. Thus, every mass-point basically leads to an own analysis. This way the information from the distributions is used in an optimal way. Another major advantage of this method is that it enables to use test-mass specific information in an efficient way. Kinematic variables can be build as an input to the likelihood function, that explicitly contain mass information, e.g. that the invariant mass of two dijets should be equal to m_{h} and m_{A}.

With both masses m_{h} and m_{A} being unknown parameters, it takes a lot of computing power to simulate a sufficient number of signal events per mass point in the mass plane. The signature of the events, however, does not depend on the values of α and $\tan\beta$. These two parameters only affect the total number of events expected for a certain mass-point. For this analysis the mass-region $25\ \mathrm{GeV} < m_{\mathrm{h}} < 100\ \mathrm{GeV}$ and $40\ \mathrm{GeV} < m_{\mathrm{A}} < 60\ \mathrm{GeV}$ has been chosen. The analysis itself is symmetric under the interchange of h and A. Therefore as well the region $25\ \mathrm{GeV} < m_{\mathrm{A}} < 100\ \mathrm{GeV}$ and $40\ \mathrm{GeV} < m_{\mathrm{h}} < 60\ \mathrm{GeV}$ is included. The difference lies only in the expected number of events, which will be taken into account after the likelihood function is build, by normalizing it to the correct number of events. The region chosen covers already a wide range of masses. This region has been chosen because here the analysis can contribute most efficiently to existing searches in other channels. At OPAL for instance the flavour-independent search (described in [39]) for Higgs bosons produced together with a Z-boson in the Higgs-strahlung process, covers the region $m_{\mathrm{h}} > 60\ \mathrm{GeV}$. In the mass grid $25\ \mathrm{GeV} < m_{\mathrm{h}} < 100\ \mathrm{GeV}$ and $40\ \mathrm{GeV} < m_{\mathrm{A}} < 60\ \mathrm{GeV}$, for steps of 2.5 GeV, a thousand events each have been simulated per mass-point for the process $\mathrm{h}, \mathrm{A} \rightarrow \mathrm{c\bar{c}}$. Furthermore, for 34 points in the mass-region $30\ \mathrm{GeV} < m_{\mathrm{h}},\ m_{\mathrm{A}} < 160\ \mathrm{GeV}$, additional samples of $\mathrm{h}, \mathrm{A} \rightarrow \mathrm{c\bar{c}}, \mathrm{b\bar{b}}, \mathrm{gg}$ have been available for systematic checks.

As mentioned above, the main background arises from WW-production which, together with ZZ-production, will in the following be referred to as qqqq or 4-fermion background. The second largest background arises from hadronic 2-fermion processes, where two quarks are produced, and where, through multiple hard gluon radiation, a 4-jet final state is produced. This Z/γ mediated process will be often referred to as qq or 2-fermion background even if it just makes the hadronic part of it.

The multi-hadron event selection (see section 5.1) should reject most non-hadronic background. However, the processes $\mathrm{e^+e^-} \rightarrow \mathrm{e^+e^-q\bar{q}}$ and $\mathrm{e^+e^-} \rightarrow \mathrm{llq\bar{q}}$ have additionally been investigated.

6.3 Event Selection

The event selection is applied to reduce the amount of data that enter the analysis. It should have a high efficiency for the signal and a high suppression factor for the background. A cut-based selection is used and based only on such variables that do not make explicit use of a specific mass-hypothesis. The signal efficiencies, however, still depend on the mass sample tested, as for instance, depending on the mass of the neutral Higgs Bosons, a different amount of the centre-of-mass energy is left for the kinetic energy, which results in different kinematic effects that will be described below.

The following consecutive cuts are applied to the data as well as to the simulated signal and background events:

1.
   - The event is required to be a hadronic final state as described in 5.1.
   - Its effective centre-of-mass energy $\sqrt{s'}$ has to exceed 150 GeV, mainly to reduce the 2-fermion background and exclude poorly reconstructed events if an initial photon escapes

detection. The quark antiquark pairs that can be produced at a centre-of-mass energy of 189 GeV are light compared to the total energy. Therefore nearly no energy is used for their production. For those processes, the earlier on mentioned radiative returns to the Z^0 mass are favoured. On the other hand for heavier particles, thus in most of the m_h, m_A mass plane, not enough energy is available to produce these bosons if a hard photon is radiated. However one looses some efficiency in low m_h, m_A mass-regions. How this cut affects the main background and the signal for some mass points is shown in figure 6.4.

- The event should have four distinct jets, therefore the jet-resolution parameter y_{43} (see section 5.2.2) has to be larger than 0.003.

2. Each jet is required to have more than two tracks, to further reduce background from not fully hadronic events.

3. To ensure that only well measured and well reconstructed jets enter the main analysis the χ^2 probability of a 4C fit imposing energy and momentum conservation must exceed 10^{-5}.

4. Then a 6C fit is performed. Again the four-vectors are constrained to fulfil energy and momentum conservation. The two additional constraints come from requiring that the invariant masses of the dijet pairs are equal to the mass of the W-Bosons. The χ^2 probability of this fit is then required to be less than 0.01 for each of the three possible combinations of assigning two of the four jets to a W-Boson (There are 6 ways to pair 4 jets to form two particles; for the fit two of these combinations each lead to the same result, since both W bosons are assumed to have the same mass).

The number of events that is left after each of the cuts can be seen in table 6.1[1].

Cut	Data	Expected Background					Average Signal Efficiency
		Total Bgd.	$q\bar{q}q\bar{q}$	$q\bar{q}$	$e^+e^-q\bar{q}$	$l\bar{l}q\bar{q}$	
-	-	24318.4	1448.7	16985.8	4391.4	1493.7	100 %
1	1947	1886.6	1195.7	539.0	6.1	145.8	65.76 %
2	1592	1530.8	1087.8	409.9	1.4	31.7	60.92 %
3	1496	1445.1	1062.0	376.0	0.9	6.2	57.97 %
4	908	890.5	555.7	328.4	0.8	5.6	51.54 %

Table 6.1: Cut-flow table. The numbers for the average signal efficiency are evaluated with the main Monta Carlo sample for the decay $h, A \to c\bar{c}$. For the additional samples $h, A \to c\bar{c}, b\bar{b}, gg$ see appendix B. The background reduction factor for qqqq background is 2.6, the reduction factor for qq background is 51.7.

It can be seen from these numbers that the first cut is rather effective in reducing 2-fermion background, eeqq and llqq events with reduction factors of about 32, 720 and 10. With the 2-fermion background this is mainly due to a large amount of events with initial state radiation that are reduced by the cut on the $\sqrt{s'}$ value, while the eeqq and llqq events are mainly reduced with requiring the event to be multihadronic. The last cut has, as expected, the largest impact on background from WW production. The overall reduction factors are 2.6 for WW/ZZ events and 51.7 for hadronic 2-fermion events. As the signal distributions for $\sqrt{s'}$ as well as the other cut variables vary over the mass plane, so does the signal efficiency vary from mass point to mass point. Table 6.1 contains the average signal efficiency. For a detailed scan in figure 6.5 the efficiencies are shown for all scanned mass points.

[1] Tables of this kind are often referred to as cut-flow tables.

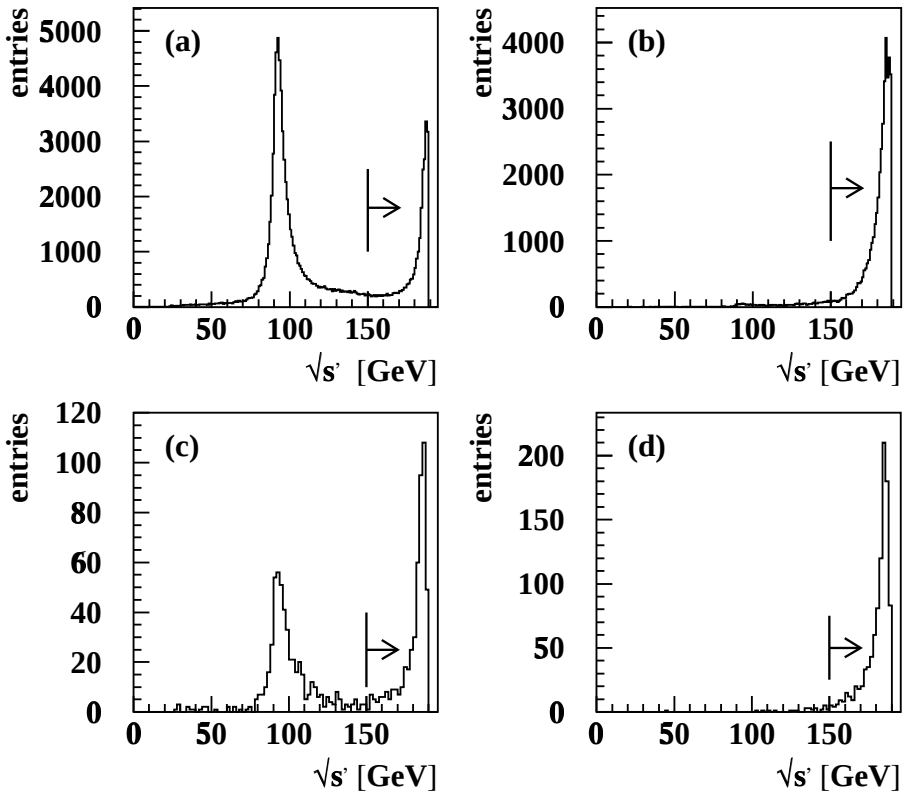

Figure 6.4: Distribution of the effective centre-of-mass energy: (a) for the processes $e^+e^- \to \gamma \setminus Z \to q\bar{q}$, (b) for the processes $e^+e^- \to WW \setminus ZZ \to q\bar{q}q\bar{q}$ and (c),(d) for $e^+e^- \to hA$, with $m_h = 40$ GeV, $m_A = 40$ GeV and $m_h = 60$ GeV, $m_A = 60$ GeV, respectively. Above $m_h = m_A \approx 40$ GeV the effective centre-of-mass energy is approximately distributed like (d).

For points outside the efficiencies have been interpolated with the points in the described mass grid and additional points reaching up to 160 GeV in mass. The interpolation is done in a plane in the ($m_{\mathrm{h}}, m_{\mathrm{A}}, efficiency$) space, using the three closest mass points. The rejection of WW events reduces the signal efficiency at masses around the W mass. Due to incorrect jet assignments, hA events away from the W mass can produce interpretations consistent with the WW hypothesis. The efficiency in low mass regions is mainly reduced due to the cut on $\sqrt{s'}$. Additionally events with rather low m_{h} and m_{A} cease to have four distinct jets. After all cuts 908 candidate events remain in the data, which is in agreement with 890.5$\pm$ 29.8 (statistical error only) events expected from Standard Model background.

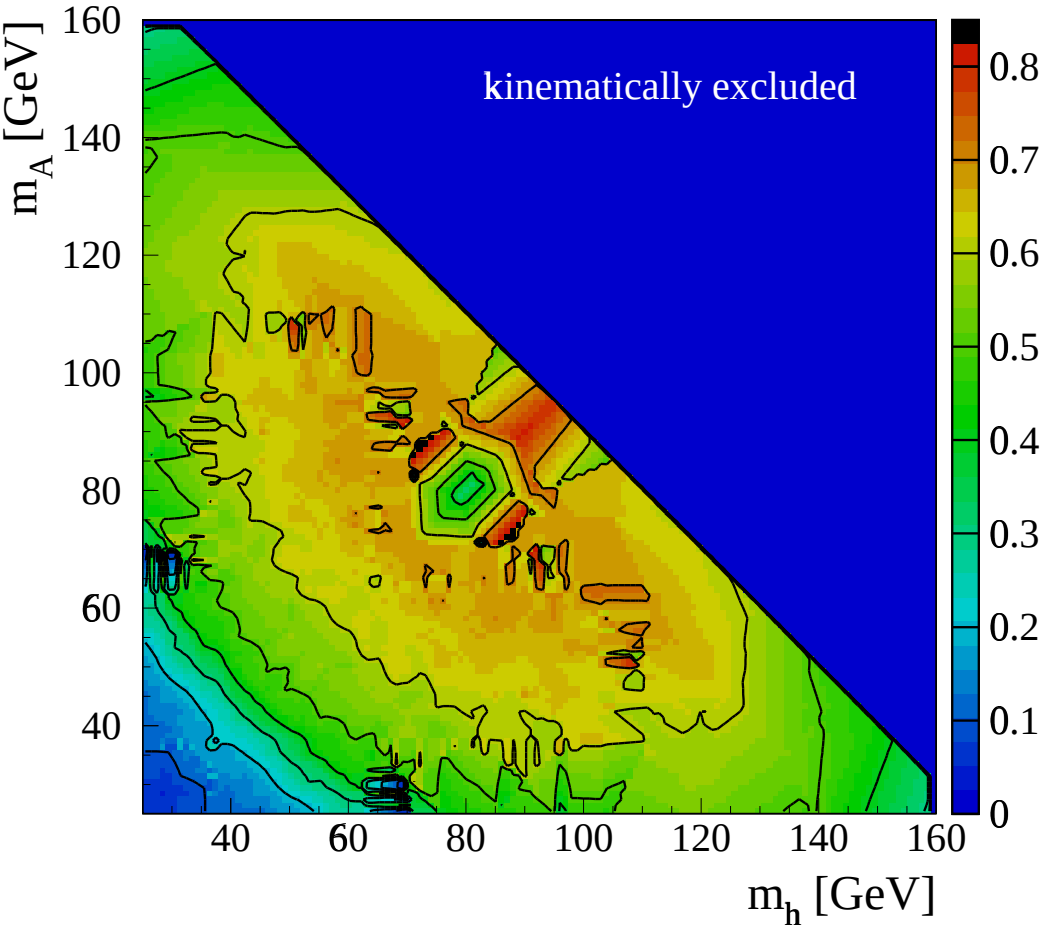

Figure 6.5: Signal efficiency after all cuts for the process $\mathrm{h,A} \rightarrow \mathrm{c\bar{c}}$. All available mass points are taken into account and the efficiency for intermediate mass points has been interpolated using the three closest mass points.

6.4 Likelihood Discriminant

As a next step the probabilistic nature of the events is used to build a likelihood function, as described in the previous chapter. It is build from the signal likelihood as defined in 5.12, the background shapes enter the function as normalisation. This function is build as a discriminating variable between the above described signal and the background from Standard model processes. As mentioned earlier on, this analysis is based on a three class likelihood. That means that the normalized probability functions are build from three classes: the signal, the background from WW/ZZ events and the background from qq-events, which is justified by the fact that hardly any events from the other two background channels remain after the cuts. They are however included in the further analysis, by calculating their likelihood function for the signal class.

6.4.1 Likelihood Variables

In the following the variables used to build the normalized probability functions are introduced.

Jet Resolution Parameter

The jet resolution parameter y_{43} has already been used as a cut-variable in the event selection. However it still contains information to discriminate between signal and background. The normalized probability function is build out of its logarithm. It mainly discriminates between signal and 2-fermion background, as the 2-fermion background has a rather 2 jet-like structure and therefore $\log_{10} y_{43}$ takes lower values.

C-Parameter

The C-Parameter, as described in 5.2.3, reaches values close to one if the energy and tracks are spread homogeneously over the whole solid angle. For pencil-like shaped events it takes values close to zero.

QCD- Matrix Element

The calculation of decay rates and cross sections needs two main ingredients, the amplitude of a certain process, often referred to as matrixelement M, and the available phase space (the density of possible final states). This is summarized in Fermis *Golden Rule*

$$transition\ rate = 2\pi |M|^2 \times phase\ space.$$

The phase space factor contains the kinematical information and reflects the fact that a process is more likely to occur the more possible final states it take. The matrixelement on the other hand contains all the dynamical information specific for a certain process. It is a result from evaluating all relevant feynman diagrams for the underlying interaction. The matrixelement is related to the probability for a certain initial state to produce a certain final state. Therefore it is suitable to discriminate between different channels. In ignorance of the actual process that occured in an interaction, every event can be treated as if came from a certain process. A matrixelement can be calculated for all events from the initial and final state 4-vectors, treating it as if the process comes from a certain calculable one. In this analysis the logarithm of the QCD-matrixelement, as calculated in [40], is used as an input for the likelihood discriminant. It has higher values (as it is related to a probability) for actual QCD events and lower values for non-QCD events, such as 4-fermion backgrounds and the signal process.

5C fit Probability

The probability of a kinematic fit with five constraints is used. The first four constraints are the usual constraints on energy and momentum conservation. The fifth constraint entering the fit procedure forces the two dijet masses to be equal. Therefore, for masses off the diagonal in the mass plane, the 5C fit probability should be lower for the signal compared to the values it takes for the background. The possible values range from 0 to 1. In all following figures this fit probability is shown on a logarithmic scale.

Cosine of Minimal Angle between Jets

The minimal angle between any two jets is found and the cosine of this value is taken as input for the likelihood function. For a four jet topology it can in principle take values from -0.5 to 1 corresponding to angles between 120 degree and 0 degree. The maximal possible value for this minimal angle is reached when the jets are equally distributed over the solid angle, when the angle between all jets in all directions is the same. For four jets this value is 120 degree.

For background from $e^+e^- \to Z^0/\gamma \to q\bar{q}$ with multiple hard gluon radiation this value peaks close to one. This is due to the fact that high energetic gluons are emitted from the quarks under a rather small angle. For the four fermion background the value is rather low, due to the low kinetic energy of the W-bosons decaying. The signal distribution in this variable thus depends on the masses of the produced bosons h and A. For low masses and therefore higher kinetic energies of the produced bosons, the two quarks resulting from the bosons have a rather low angle between them. The angle increases then with decreasing mass.

Chisquare Distribution

The last variable entering the Likelihood is a test-mass specific variable, the logarithm of the χ^2 resulting from the difference in the measured mass and the hypothesized mass for m_{h} and m_{A}.

There are six possible assignments of pairs of jets to h and A. However, as this analysis does not distinguish between h and A one is left with three possible assignments that should be tested for consistency with a possible signal.

A 4C fit, imposing energy and momentum conservation, is performed for all three possible combinations. This fit yields reconstructed masses for h and A as well as their 2×2 covariance matrices c.

From these matrices the χ^2 is computed according to

$$\chi^2 = \frac{(x-x_{rec})}{\sigma_x^2(1-\rho^2)} + \frac{(y-y_{rec})}{\sigma_y^2(1-\rho^2)} - 2\frac{(x-x_{rec})}{\sigma_x}\frac{(y-y_{rec})}{\sigma_y}\frac{\rho}{1-\rho^2}. \tag{6.2}$$

$x(y)$ and $x_{rec}(y_{rec})$ stand for the hypothesized and reconstructed $m_{\mathrm{h}}(m_{\mathrm{A}})$ respectively and ρ is the correlation coefficient defined as

$$\rho = \frac{\mathrm{c}(1,2)}{\sqrt{\mathrm{c}(1,1)\cdot\mathrm{c}(2,2)}}. \tag{6.3}$$

The logarithm of the smallest χ^2 out of the three possibilities provides the last input variable to the Likelihood function.

6.4.2 Data-MC Comparison

Figure 6.6 shows the input variables for the likelihood function. The simulated background is normalized to the integrated luminosity of the data collected with the OPAL detector in 1998 at a centre-of-mass energy of 189 GeV. Within statistical fluctuations the data agree with the background from Standard Model expectations.

6.4.3 The Normalized Probability Density Functions

Figures 6.7 and 6.8 show the discrimination power of the 6 input variables for the likelihood for signal mass hypotheses of $m_{\mathrm{h}} = 30$ GeV and $m_{\mathrm{A}} = 60$ GeV (and vice versa) and $m_{\mathrm{h}} = 60$ GeV and $m_{\mathrm{A}} = 60$ GeV. The distributions are normalized to unit surface. The background shape of the first five variables does not change with the signal mass hypothesis. The sixth variable is dependent on the signal mass tested and thus changes slightly. As can be seen the shapes depend rather strongly on the signal mass hypothesis, a reason for this analysis being mass dependent. In appendix A these distributions are shown for several more mass points to make clear how the signal evolves. In figure 6.7 one can see that with the Boson h being rather light, the signal distributions rather resemble background from 2-fermion processes, while in 6.7, for higher (and equal) masses of h and A the signal starts to rather look like the 4-fermion background.

6.4.4 Likelihood Performance

The six variables are now input to the likelihood discriminant for the signal class explained in chapter 5.3. For background and signal the value of the likelihood function is calculated assuming the event is signal like. Therefore background events should have low values of this a probability resembling quantity, while signal events should have rather high values. Figures 6.9 and 6.10 show the likelihood function on a logarithmic scale for all backgrounds, signal and data.

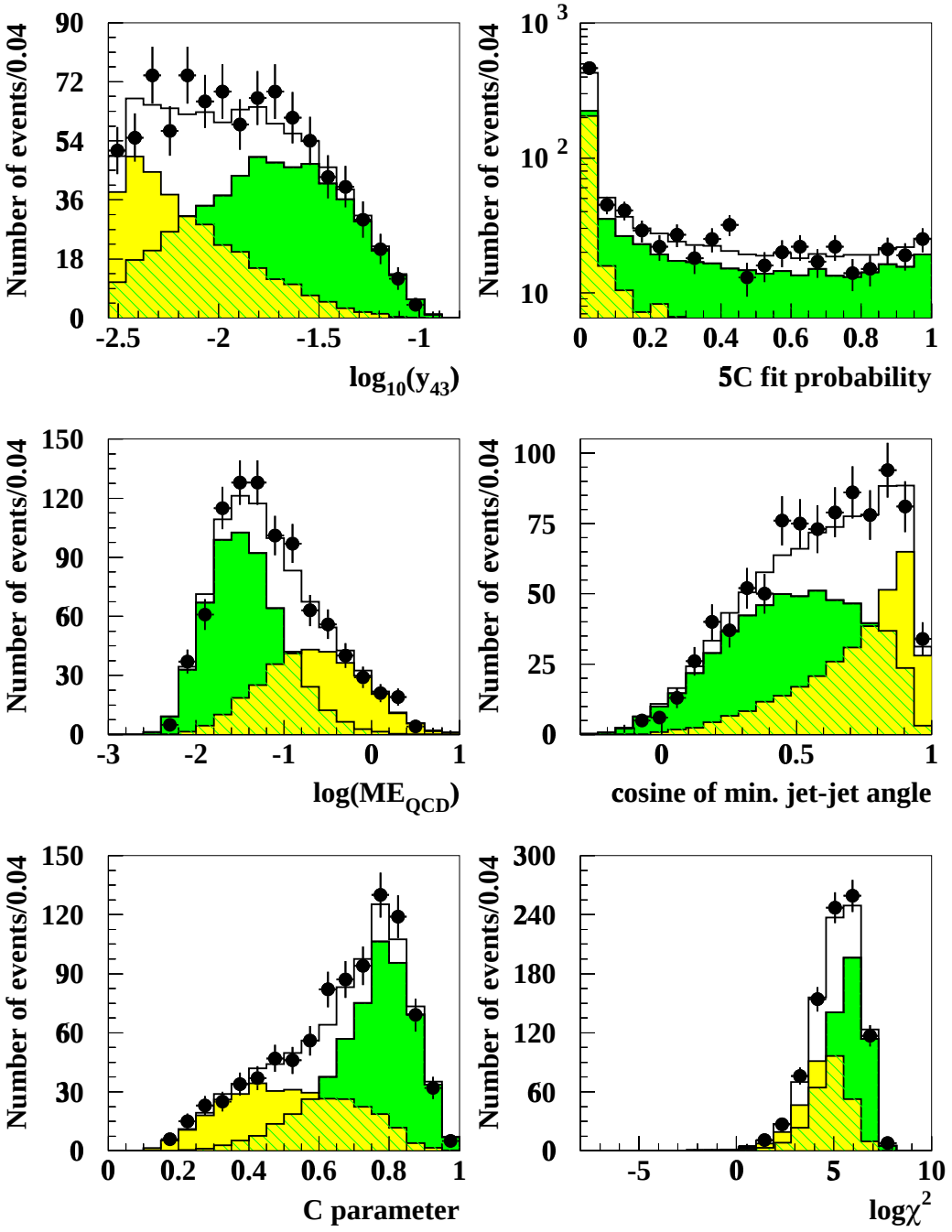

Figure 6.6: Distribution of the likelihood input variables. Compared are the data taken at 189 GeV and the two main Standard Model backgrounds. The green (dark grey) histogram shows the distribution of the 2-fermion background, the yellow (light grey) histogram shows the distribution of the 4-fermion background. In the white histogram the two backgrounds are added together for comparison with the data shown as dots with error bars.

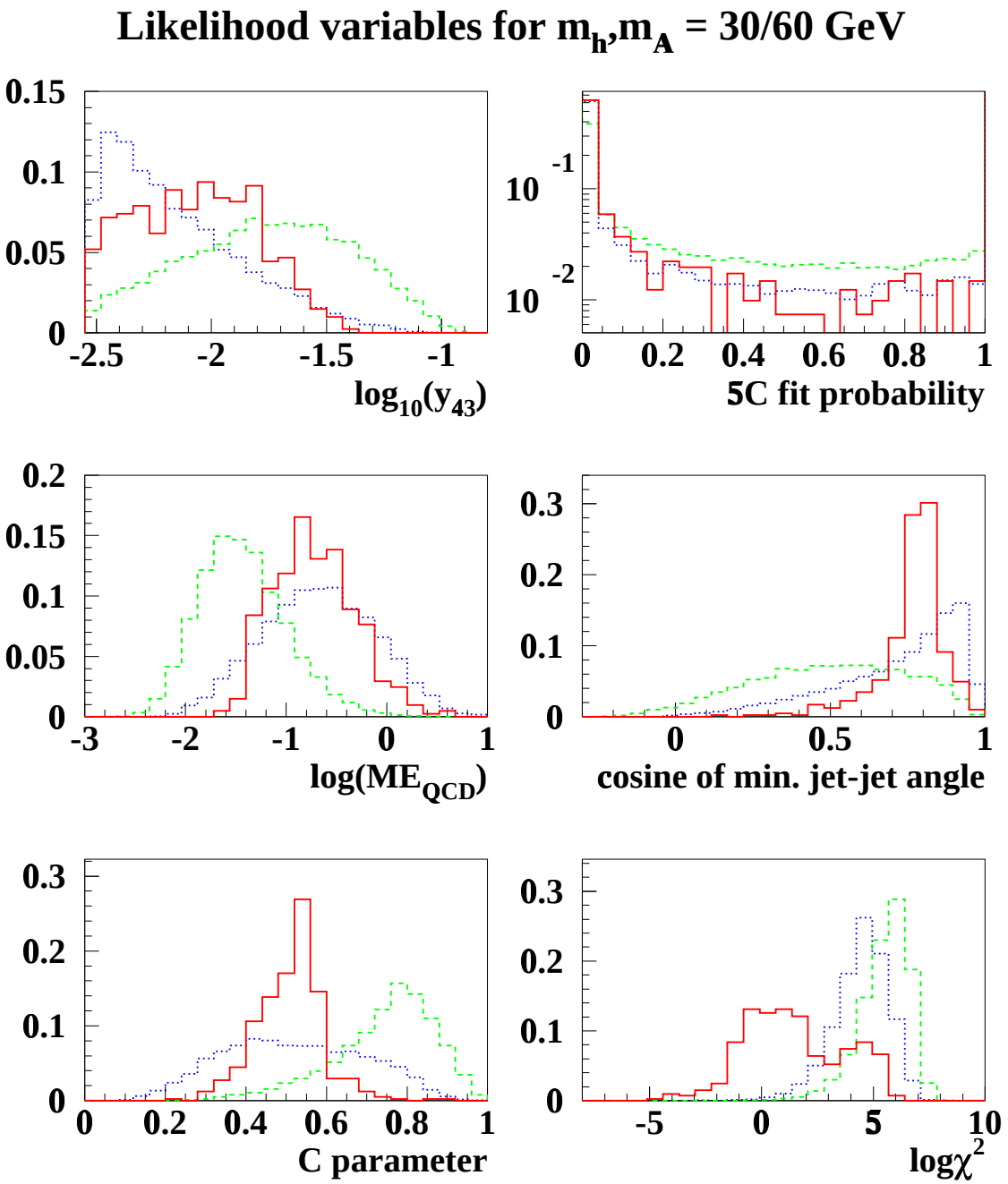

Figure 6.7: Normalized reference distributions for a signal mass $m_h = 30$ GeV and $m_A = 60$ GeV or vice versa. The red (solid) histogram shows the signal distribution, the green (dashed) histogram shows the distributions of the 4-fermion background and the blue (dotted) histogram shows the 2-fermion background distribution.

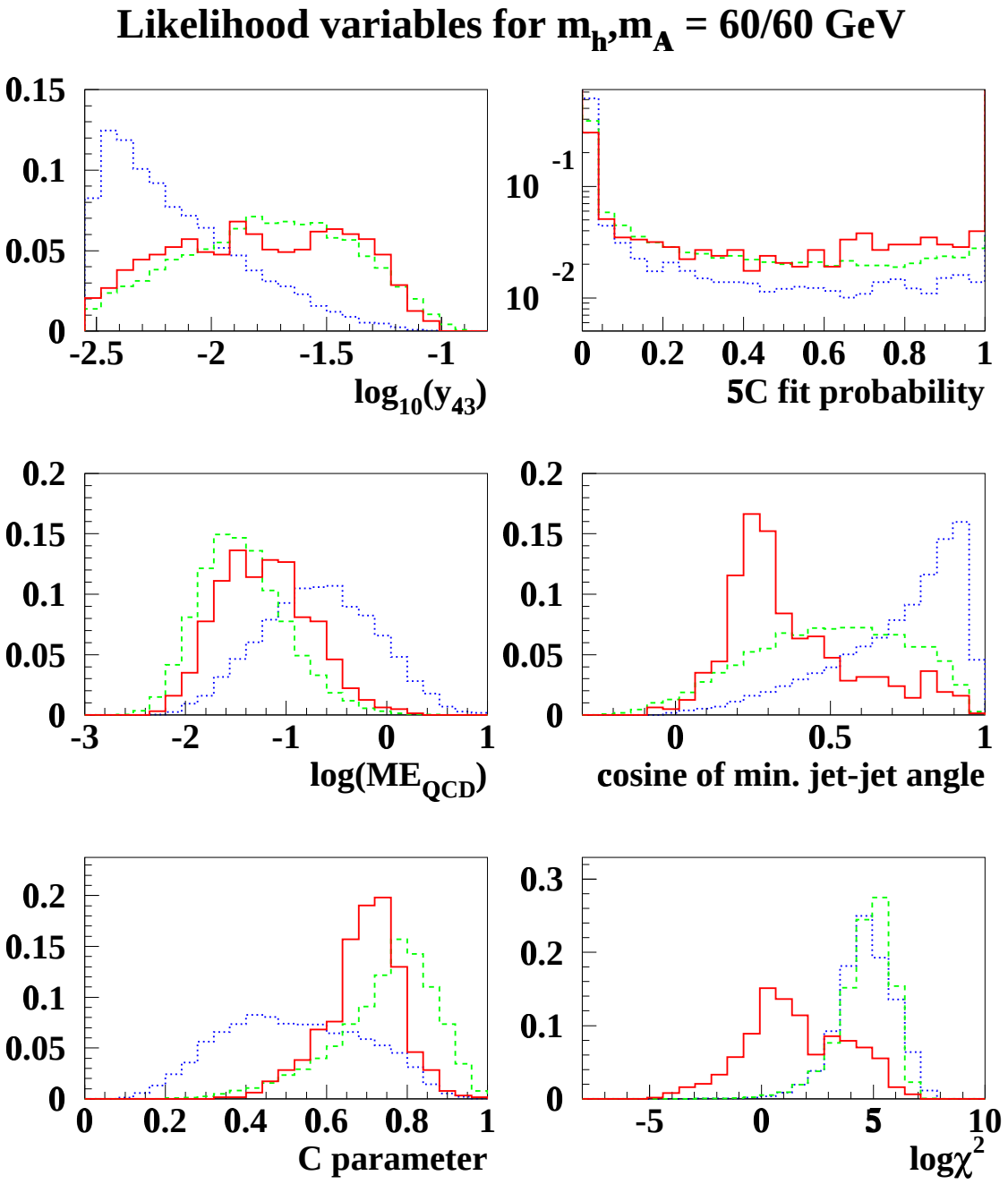

Figure 6.8: Normalized reference distributions for a signal mass $m_h = 60$ GeV and $m_A = 60$ GeV. The colour code may be taken from figure 6.7.

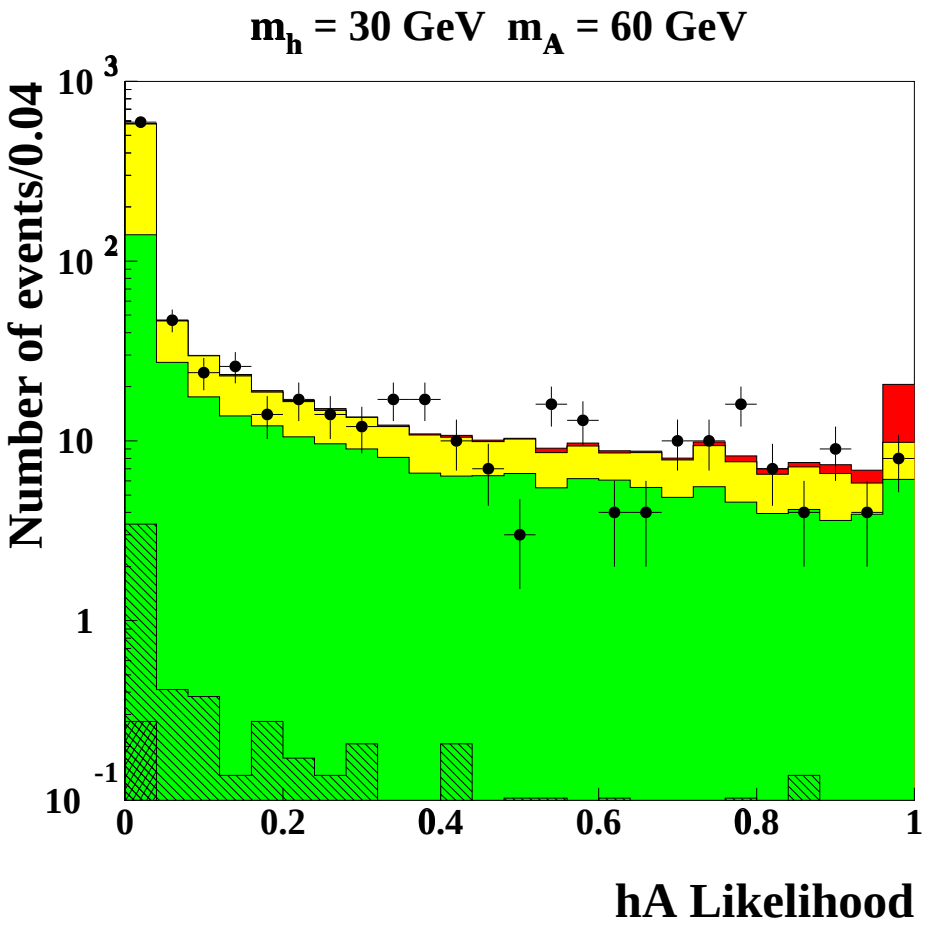

Figure 6.9: Distribution of the hA Likelihood for $m_h = 30$ GeV and $m_A = 60$ GeV. The hatched histogram shows the background from $llq\bar{q}$ production including a small contribution from the $e^+e^-q\bar{q}$ background (reverse-hatched). The green (dark grey) histogram shows the 2-fermion background on top and the yellow (light grey) histogram finally shows all backgrounds together, including the 4-fermion background. The points with error bars show OPAL data at a centre-of-mass energy of 189 GeV. The red (dark) histogram shows how a signal would be distributed for $m_h = 30$ GeV and $m_A = 60$ GeV. Although the signal shape does not change over the $\tan\beta/\alpha$ plane, the total number of expected signal events varies. Here the number expected for $\tan\beta = 0.7, \alpha = 0$, a data luminosity of 172.1 pb^{-1} and a signal efficiency of 40.5% is shown.

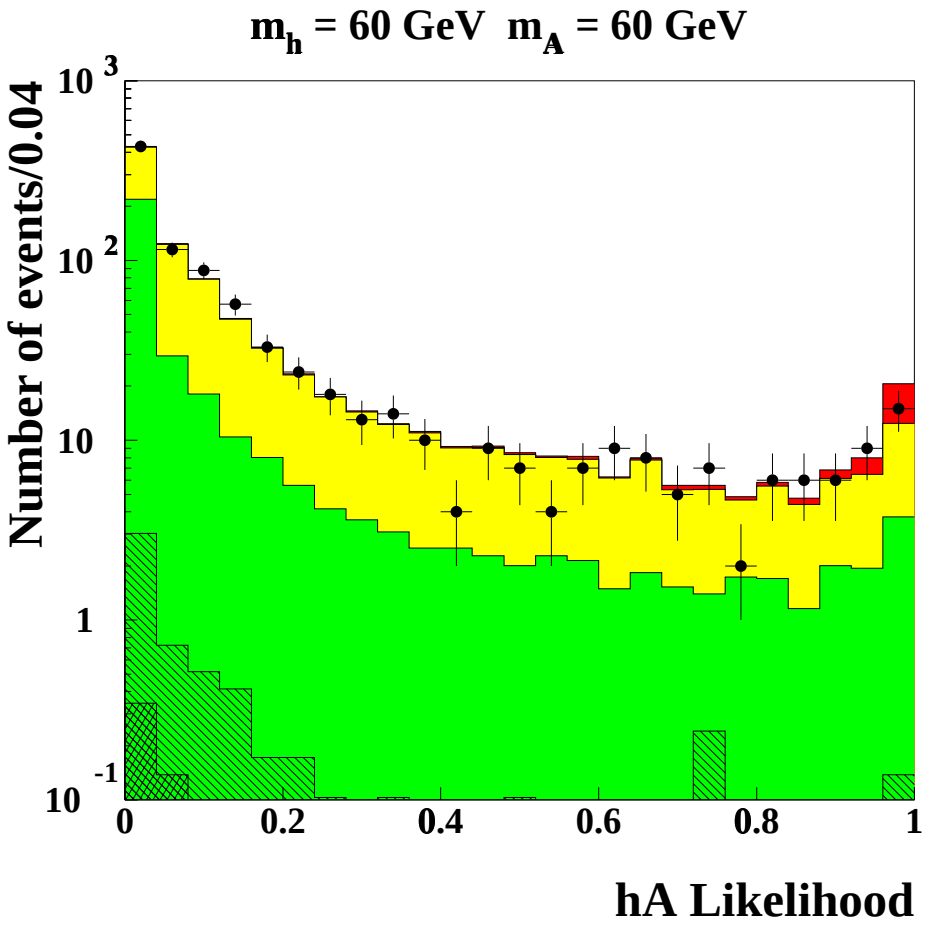

Figure 6.10: Distribution of the hA Likelihood for $m_h = 60$ GeV and $m_A = 60$ GeV. The colour code is as in figure 6.9. The expected number of signal events shown on top of the background belongs to $\tan\beta = 0.7, \alpha = 0$ and a signal efficiency of 63.2%.

6.5 Limit Setting

Searches are designed to distinguish between two hypotheses: the production and detection of new particles along with the Standard Model background, or the presence of Standard Model background only. They aim to either confirm a signal or, in its absence, to exclude a signal as strongly as possible. If the data show no significant excess above the Standard Model background the exclusion of a possible signal is commonly expressed in terms of *confidence levels CL*. A *confidence limit* is then the value of a population parameter (such as the mass of a particle or a production rate), that is excluded at a certain *CL*. A confidence limit becomes an upper (lower) limit for a model parameter, if the confidence level is less (greater) for all values of the modelparameter above (below) this confidence limit. A 95 % confidence level means that a search could have missed a signal in not more than 5% of the cases. To describe what it means to miss a signal the quantity *test statistic* or *estimator X* plays an important role. It is a function of the observed candidates, the expected signal and the expected background and is constructed to increase monotonically for increasingly signal-like (decreasingly background-like) events so that the confidence level in the signal+background hypothesis is given by the probability that the test-statistics is less than or equal the value observed in the experiment X_{obs}. With the choice of a test statistic the above mentioned confidence level can be expressed as follows

$$CL_{s+b} = P_{s+b}(X \leq X_{obs}), \tag{6.4}$$

where X_{obs} is the value of the test statistic computed from the observed candidates and the expected signal and background. The probability is the fraction of possible experimental outcomes smaller than the observed assuming the presence of signal and background together

$$P_{s+b}(X \leq X_{obs}) = \int_0^{X_{obs}} \frac{dP_{s+b}}{dX} dX, \tag{6.5}$$

where dP_{s+b}/dX is the probability distribution function of the test statistic for signal+background experiments. Small values of CL_{s+b} indicate poor compatibility with the signal+background hypothesis and favor the background hypothesis. Analogously the confidence level for the background-only hypothesis is defined as

$$CL_b = P_b(X \leq X_{obs}), \tag{6.6}$$

where dP_b/dX is the probability distribution function of the test statistic for background-only experiments.

$$P_b(X \leq X_{obs}) = \int_0^{X_{obs}} \frac{dP_b}{dX} dX. \tag{6.7}$$

Nevertheless the test statistic remains unchanged and thus is still a function as well of the expected signal. (The test statistic is calculated from the observed candidates, the signal and background shapes are then tested for compatibility with a background-only hypothesis.) A third quantity is defined from the two quantities CL_{s+b} and CL_b. Due to the fact, that for very low rates the above definitions could yield very high exclusion limits for the signal+background hypothesis, but also for the hypothesis of background only, the confidence level observed for signal+background is normalized to the confidence level for the background-only hypothesis

$$CL_s \equiv CL_{s+b}/CL_b. \tag{6.8}$$

This approach is commonly referred to as 'modified frequentist procedure' [41–43]. The quoted confidence level finally is

$$CL = 1 - CL_s. \tag{6.9}$$

The test statistics used in this analysis is a sum of weights of all selected events. It assumes that there exists a physical variable m, which could for instance be an invariant mass or some output of artificial neural nets and in the case of this analysis is the signal likelihood function. The expected spectrum for the search channel k, $D_k(m - m_{theo})$, is determined from Monte-Carlo events. This spectrum has its maximum value D_{max} if m is close to m_{theo}. The weight X_i of event i with value m_i is then given by

$$X_i = \frac{D(m_i - m_{theo})}{D_{max}}, \quad (0 \leq X \leq 1) \tag{6.10}$$

The probability distributions of this weighted sum is calculated considering the number of produced events, that follow a Poisson statistics. The analytical formula as well as approximations for the case of gaussian distributed variables or large event counts are derived in [44]. This test statistics is chosen according to [44], to simplify a possible combination of several search channels with this analysis for a general scan of the parameters in the 2HDM as it has been performed in [39].

Another interesting application of this analysis is the model independent interpretation of the results. The analysis can be used to search for any scalar neutral boson S^0 produced along with a pseudo-scalar neutral boson P^0 in the generic process $e^+e^- \to Z^0/\gamma \to S^0P^0$. If a process is not predicted by a particular model, usually the cross sections and decay rates are unknown, so that just upper limits can be set on the cross section for such processes. These are commonly [39] expressed in terms of the scale factor c^2 which relates the cross sections of these generic processes to those of the Standard Model

$$\sigma_{\mathrm{SP}} = c^2 \bar{\lambda} \sigma_{\mathrm{HZ}}^{\mathrm{SM}}. \tag{6.11}$$

Assuming a 100 % branching ratio to this final state, c^2 is, for the respective final state under investigation, obtained from

$$c^2 = \frac{N_{95}^{\mathrm{SP}}}{\Sigma(\varepsilon \mathscr{L} \lambda \sigma_{\mathrm{HZ}}^{\mathrm{SM}})}, \tag{6.12}$$

where N_{95}^{SP} is the upper limit at the 95 % CL on the number of possible signal events in the data, $\mathscr{L}$ is the integrated luminosity and ε is the efficiency of the selection. The sum runs over different centre-of-mass energies.

6.6 Results

The analysis did not reveal any significant excess above the expected background from Standard Model processes. Therefore the method described above has been applied to set confidence levels for each considered point in the $(m_{\mathrm{h}}, m_{\mathrm{A}}, \tan\beta, \alpha)$ space. The shape of the likelihood function does not change with the values for the model parameters $\tan\beta$ and α. However, the expected number of

signal events does change significantly and has to be calculated for every space point. Therefore, a scan over these parameters has been performed and limits are derived for all points subject to this scan. The production cross sections for h and A as well as the decay branching ratios have been determined with the HZHA-Generator ([45] [25]) for the following scan points representative for the whole parameterspace

α :$0^o, -15^o, -30^o, -45^o$ and -90^o;
β :22^o to 89^o in steps of 1^o (corresponding to $0.4 \leq \tan\beta \leq 57$).

As analyses relying on b-quark specific informations have higher sensitivity at scan points where the branching ratio to b-quarks is not suppressed in this analysis the scan has been restricted to values $\alpha = 0^o$ and $\alpha = -15^o$.

Figure 6.12 shows the value of CL_s for all scanned mass points and the model parameter values α=0 and $\tan\beta$=0.577. In the top plot the maximum value of CL_s is set to one, which belongs to the black coloured areas. As exclusion at a 95% confidence level means a value of CL_s below 0.05, the maximum—related to the black coloured points—is set to 0.05 in the bottom plot, so that black areas correspond to unexcluded mass points (the white points are not included in the analysis).

For mass points with $m_{\mathrm{h}} \geq 2m_{\mathrm{A}}$ the decay rate for $\mathrm{h} \rightarrow \mathrm{AA}$ exceeds by far the decay rates $\mathrm{h} \rightarrow \mathrm{q\bar{q}}$, due to the fact that the Higgs boson coupling increases with mass [2]. As this analysis does not focus on such decays, the exclusion limit is weakened due to a rather low number of expected signal events for these points. This behaviour can be clearly seen in figure 6.12.

Figure 6.13 finally shows in yellow mass points that have been excluded for a whole range of values of $\tan\beta$.
It can be seen that the sensitivity decreases for increasing values of $\tan\beta$. This is due to the interplay of $\tan\beta$ and α both influencing the production cross section. For $\alpha = 0^o, -15^o$, the production cross section for pair-production decreases with increasing values of $\tan\beta$ according to 2.24.

[2] For very low masses of m_{h}, in the order of the mass of the b-quark, the decay $\mathrm{h} \rightarrow \mathrm{AA}$ ceases to be the most important decay for the case $\mathrm{m_h} \geq 2 \times \mathrm{m_A}$. However this low mass region is not subject to this analysis.

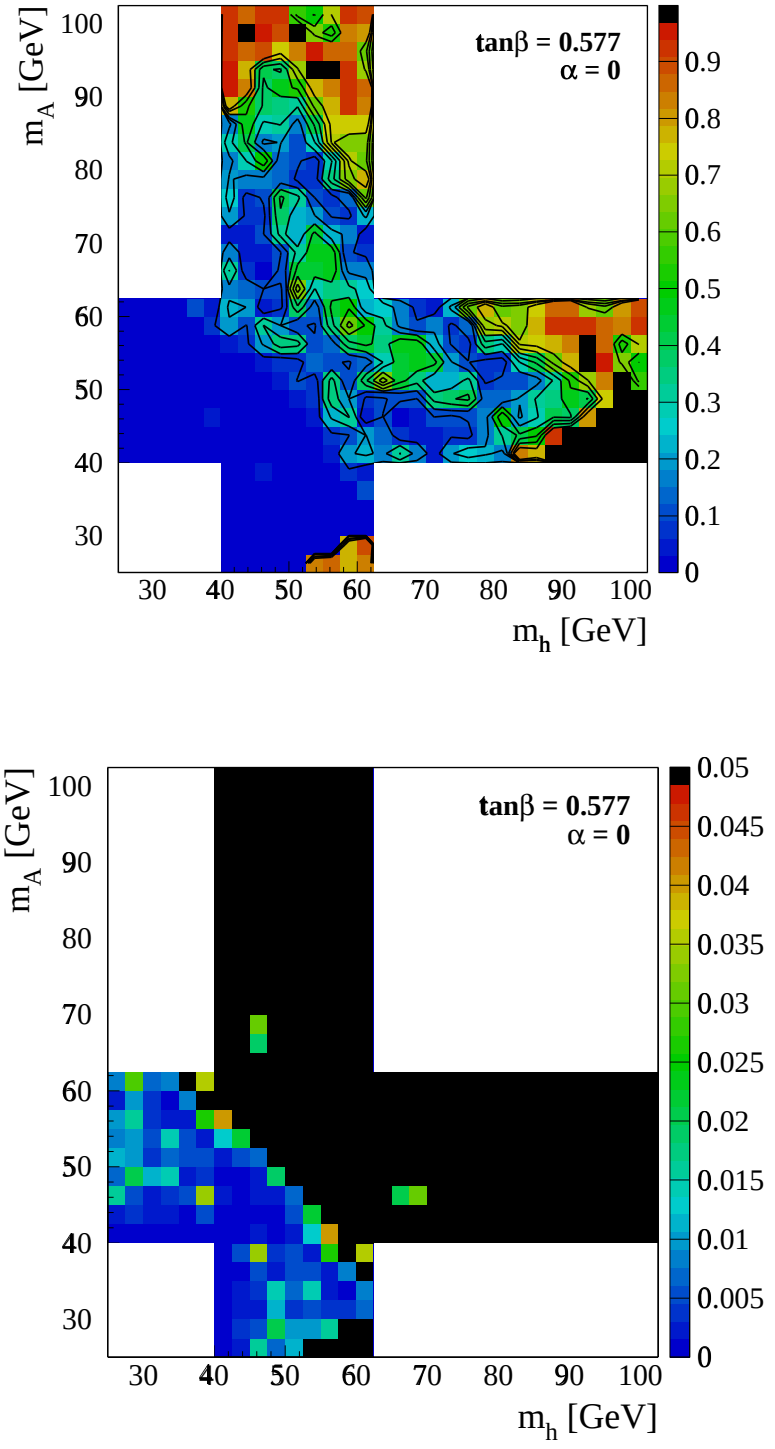

Figure 6.11: Exclusion plots for $\tan\beta = 0.577$ and $\alpha = 0$. Shown is the value of CL_s, mass points with values lower than 0.05 are excluded at the 95% confidence level. The white areas are regions not included in the analysis. The top plot shows a range of values between 0 and 1, the bottom plot shows a range between 0 and 0.05, so that all points but the black points are excluded at the 95% confidence level.

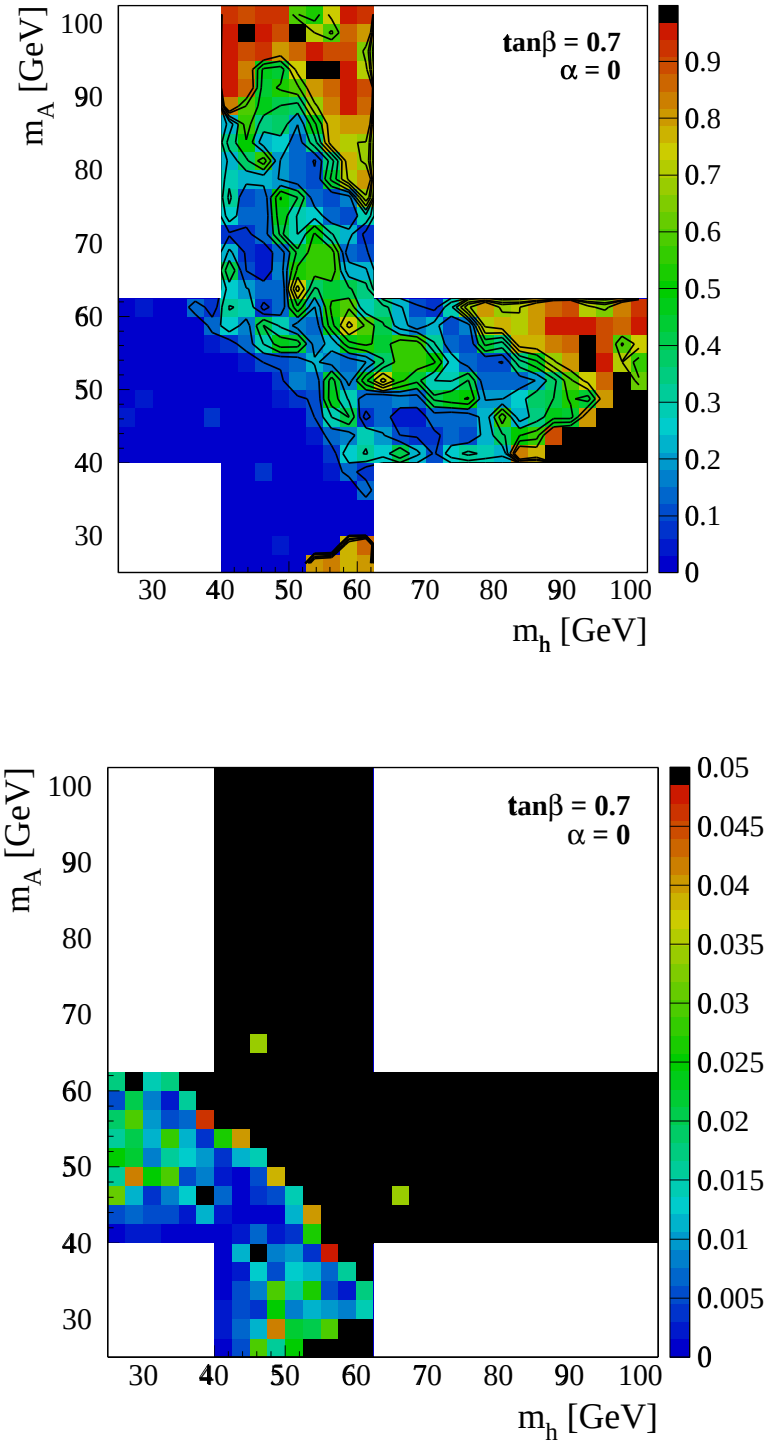

Figure 6.12: Exclusion plots for $\tan\beta = 0.7$ and $\alpha = 0$. Shown is the value of CL_s, mass points with values lower than 0.05 are excluded at the 95% confidence level. The white areas are regions not included in the analysis. The top plot shows a range of values between 0 and 1, the bottom plot shows a range between 0 and 0.05, so that all points but the black points are excluded at the 95% confidence level.

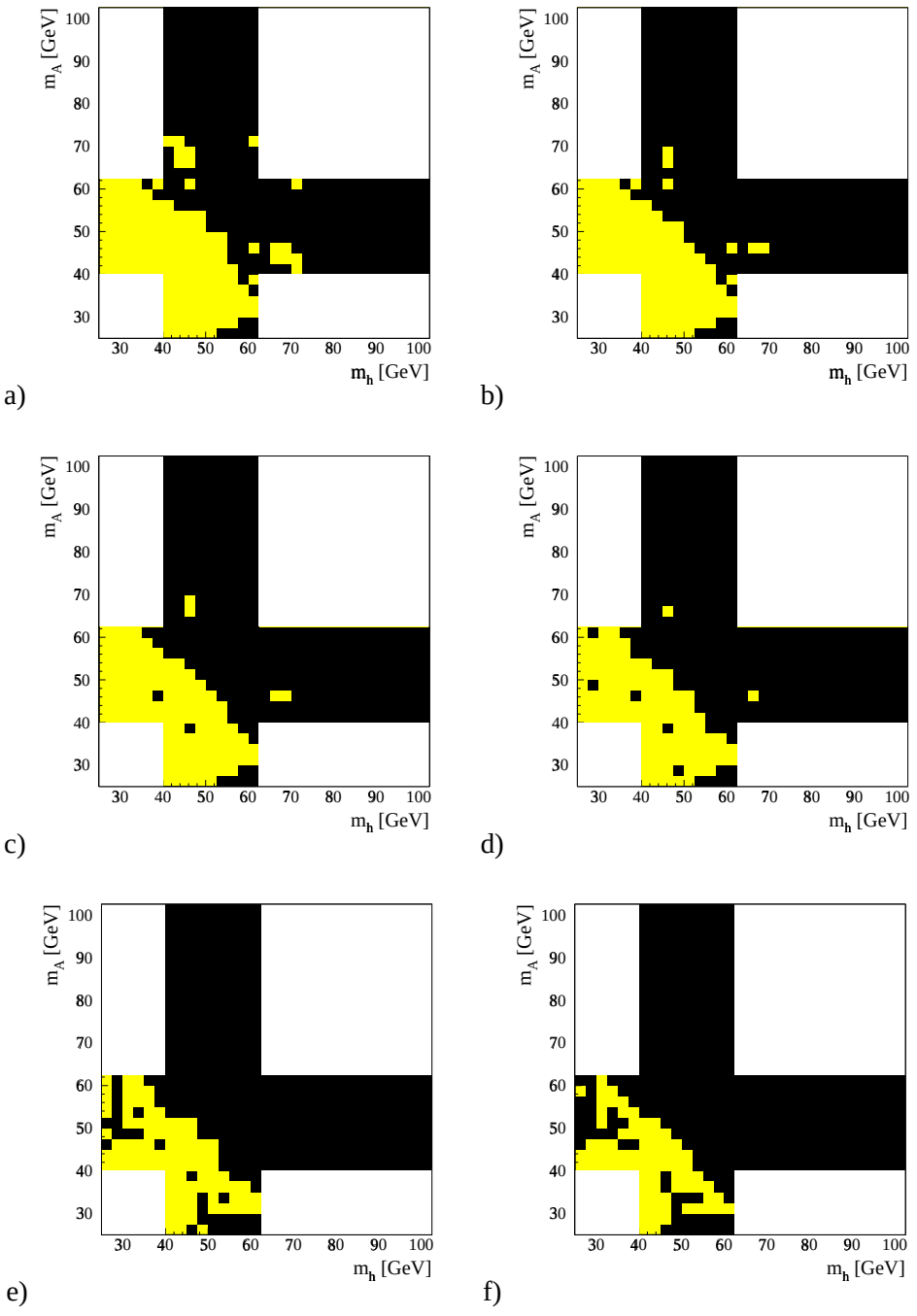

Figure 6.13: Exclusion plots of $\alpha = 0$. The yellow areas indicate points in the (m_h, m_A) plane that are exluded with this analysis at the 95 % confidence level for scanned values of $\tan\beta$ up to a) 0.5, b) 0.6. c) 0.7, d) 0.8, e) 0.9, f) 1.0.

Chapter 7

Conclusions and Outlook

This thesis preformed a search for the neutral Higgs bosons h and A in the framework of the 2HDM(II) model. It focussed on the process where the h and A are pair-produced and is sensitive to all hadronic decay modes which are resulting in a four jet final state.

Conventional analyses use the identification of b-quarks to distinguish a possible signal against W^+W^- and Z^0Z^0 production, which constitute the most serious background from Standard Model processes. This so-called tagging of b-quarks is an essential tool in standard analyses. The decay rate of Higgs bosons to a $b\bar{b}$ pair is with 85 % very high. On the other hand, the decay of W bosons into a $b\bar{b}$ pair is not allowed (charge conservation at each vertex) and the decay to a b-quark along with a top quark is kinematically not accessible for centre-of-mass energies available at LEP2. The remaining hadronic decay modes $W^- \to b\bar{u}, b\bar{c}$ only add up to less than 0.05 % of the hadronic branching ratio. However, in the 2HDM(II) models there are regions where the decay rate for $h \to b\bar{b}$ drops to zero, so that the conventional analysis would loose a signal in these regions. This work showed that moving onto a mass dependent analysis yields significant improvements in the discrimination between signal and background, that is otherwise—without the essential tool of tagging b-quarks—rather poor.

The main advantage of a mass dependent analysis is that it allows the explicit use of mass dependent variables, such as kinematic fits constraining dijet masses to Higgs mass hypotheses. In general, a mass dependent analysis makes the best use of any kind of kinematic variables. The analysis has been applied to data recorded with the OPAL detector at a centre-of-mass energy of 189 GeV, which correspond to an integrated luminosity of 172.1 pb^{-1}. No significant excess of a signal above the expected Standard Model background was observed for any of the mass points in the m_h and m_A plane subject to this analysis. Therefore, exclusion limits were calculated for every mass point in the $(m_h, m_A, \tan\beta, \alpha)$ parameter space. All obtained results, the explicit confidence levels for each analysed point, are stored and are made available to the collaboration. For a set of 34 mass points spread over the entire kinematically accessible (m_h, m_A) plane the decay of the h and A bosons to b-quarks and gluons is also simulated. The $c\bar{c}$ and $b\bar{b}$ sample resemble each other, whilst the average efficiency for gluons is higher. The Monte Carlo events are available for further checks. Systematic uncertainties in the signal normalization and shapes are not yet included in the analysis. Systematic uncertainties for the background normalization and shapes have been included in the limit setting following [39].

The analysis presented can be combined with other channels for a general scan of the parameter space of the 2HDM(II). In [39] first results of this analysis—still in its mass independent form—were used in such a combination. The updated inputs needed for such a combination are stored and made available for further studies. For a combination of several analyses, the expected confidence level is

calculated for every point in the $(m_{\mathrm{h}}, m_{\mathrm{A}}, \tan\beta, \alpha)$ parameter space according to [44]. The analysis that yields the best confidence level is chosen for the extraction of the limits. Details on the scanned regions can be found in [39].

The analysis can be extended to the whole kinematically accessible mass region and to intermediate mass points. Enough Monte Carlo samples are available to test interpolations of the likelihood input variables and the output of the likelihood for the signal case. For mass points outside the mass grid it should then be sufficient to generate Monte Carlo events in steps of 5 GeV and interpolate in between.

This analysis did not reveal a significant excess over the expectation from Standard Model background processes.

For the future the analysis can also be applied to the new data taken with the OPAL detector in the two recent years, during which the LEP accelerator was performing amazingly. The centre-of-mass energy reached 209 GeV and the luminosity from the years 1999 and 2000 sums up already to about 400 pb^{-1}, which provides more statistics and a higher kinematic limit for searches for new particles.

Appendix A

Improvements with a mass-dependent analysis

In this appendix a mass-dependent analysis is compared with two mass-independent approaches. It will become clear that moving on to a mass-dependent analysis can significantly increase the discrimination power between signal and background. The comparison is based on the likelihood performance, illustrated in terms of signal over the square root of background ratios. Subject to comparison is the likelihood function based on the jet resolution parameter y_{43}, the C parameter, the logarithm of the QCD matrixelement, the probability of a 5C fit imposing energy and momentum conservation as well as constraining the two dijet masses to be equal, and the cosine of the minimal inter-jet angle; all of these variables have been explained in section 6.4.1. The sixth likelihood input variable to this analysis, the logarithm of the χ^2 of a 6C fit, makes explicit use of test mass specific information and is therefore taken out of the comparison up to the level of the likelihood performance.

Before it had been decided to perform a mass-dependent analysis, Monte Carlo generated events for the processes $e^+e^- \to c\bar{c}, b\bar{b}, gg$ had been available for the 34 mass points in the m_h, m_A plane shown in figure A.1, which from now on are referred to "all" mass points.

These points are used to test three different approaches. In the first approach all mass points are taken together to form the reference distributions (see figure A.2). In the second approach the reference distributions are based on the "low" mass subset of mass points $m_h(m_A)$[1]=30 GeV and $m_A(m_h)$ = 40, 60, 80, 100, 120, 140, 160 GeV. This sample had been chosen in the analysis described in **??**, as the sensitivity for $m_h = m_A = 80$ GeV is expected to be rather low in any case. Therefore the analysis is optimised for mass points away from the W mass [2]. Figure A.3 shows the normalised probability functions for this case.

In the third and mass-dependent approach, the single mass point tested in the analysis is used itself to determine the shape of the reference distributions. In figures A.4 to A.5 the distributions of the 3 likelihood input variables that change most significantly with the mass hypothesis are shown for 6 different test-masses. For comparison the distributions gained in the other two approaches are added. The figures show very clearly how the signal shape changes from one mass hypothesis to the next. Looking at the cosine of the inter-jet angle (fig. A.5 on page 68) in the approach using all masses there is no discrimination between the 4-fermion background and the signal shape. Therefore

[1] The analysis does not distinguish between h and A.

[2] The sixth likelihood input variable, the logarithm of the χ^2 of a 6C fit was used as input histogram to the limit calculations. Here the analyses will be just compared at the level of the likelihood function, using in all cases just the above mentioned 5 variables.

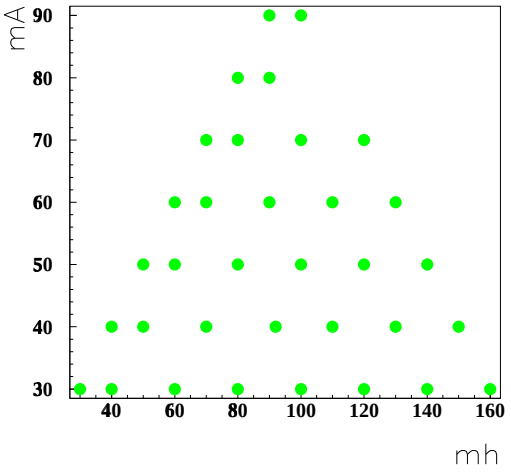

Figure A.1: Set of mass points for which signal events of the type $e^+e^- \rightarrow hA \rightarrow c\bar{c}, b\bar{b}, gg$ have been simulated.

for instance testing the performance of the likelihood for a signal m_h, m_A= 30,60 GeV using these reference histograms will assign for these signal events a rather low probability to belong to the signal class. For m_h, m_A= 30,60 GeV the cosine of the minimal jet-jet angle is distributed around 0.8. If one is looking at the distributions of this variable for signal and background using all masses, an event with a value of 0.8 is categorized to originate more likely from a QCD than from a signal process itself and equally likely from a 4-fermion process.

Figure A.7 on page 70 shows the likelihood performance for a mass point of m_h, m_A= 30,60 GeV tested with the first two hypotheses. Indeed the discrimination between signal and background is very poor in the first case. As expected (this point is included in the subsample of mass points) the second approach yields a slightly better performance. Figure A.8 on page 71 shows the mass-dependent analysis, which significantly performs better than the other two approaches. From the first, over the second mass-independent, to the mass-dependent analysis, the signal evolves out of the background and peaks at ever higher values of the signal likelihood. The last plot in figure A.8 on page 71 shows how drastically the performance is improved, if a variable explicitly containing test-mass specific information is included in the likelihood. In the figure this is the in the analysis used χ^2 variable for a 6C fit constraining the dijet masses to the tested masses. In both figures the number of signal events is the number expected for an integrated luminosity of 172.1 pb^{-1}, and the model parameters $\tan\beta$=0.7 and $\alpha = 0$.

A way to see the performance of the likelihood more easily is to calculate the ratio of the number of signal events and the square root of the number of background events left after gradually increasing the cut on the likelihood variable to receive a more pure sample of signal events. The first plot in figure A.10 on page 73 shows this ratio for m_h, m_A= 30,60 GeV. As expected the subset performs better than the all mass approach, while the mass dependent approach is the best. The second plot is for m_h, m_A= 60,60 GeV. While here the mass subset and the all mass approach change their roles (this mass point is not included within the subset), the mass-dependent approach again marks the best solution.

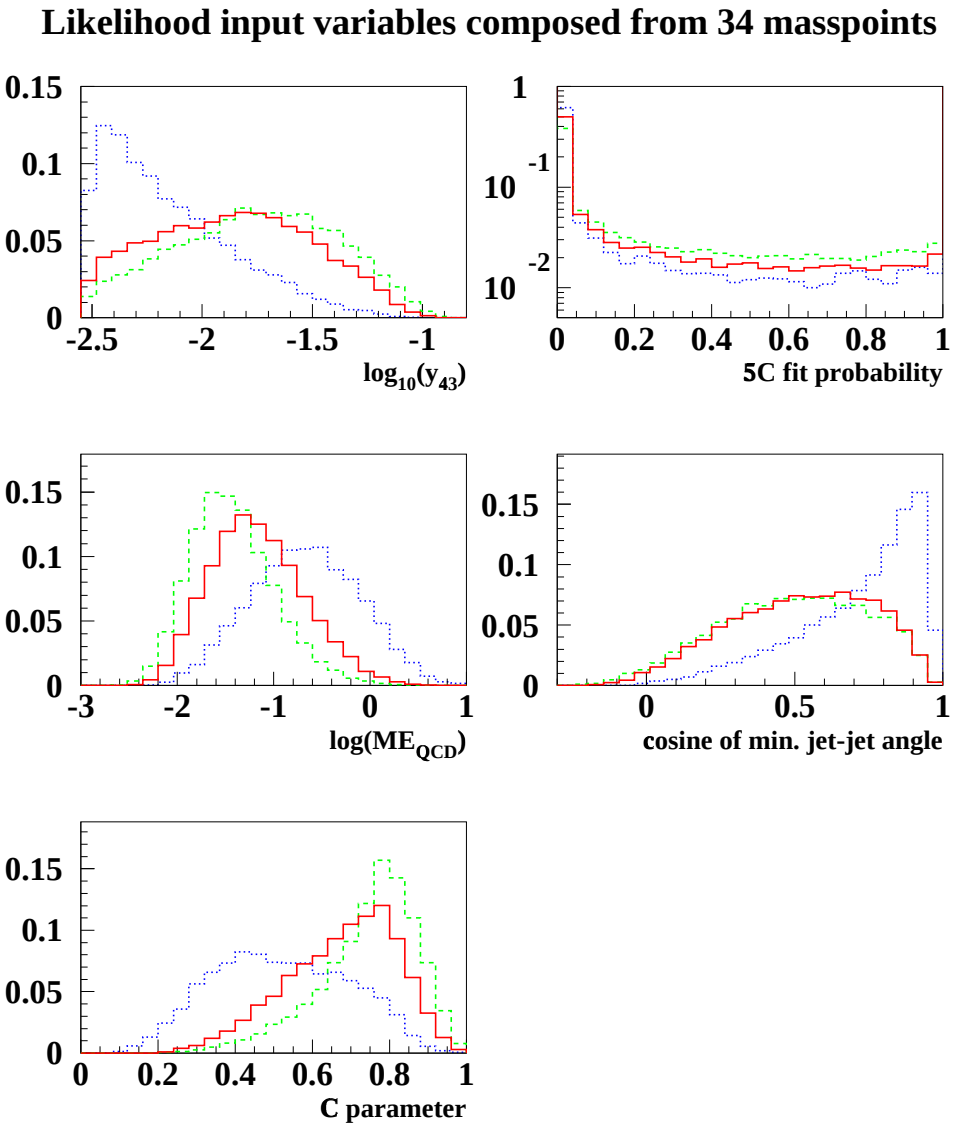

Figure A.2: Reference distributions for the first approach under comparison. The signal distributions are made using all the 34 mass points in the m_h, m_A plane shown in figure A.1. The red (solid) histogram shows the signal distribution, the green (dashed) line shows the distributions of the 4-fermion background and the blue (dotted) shows the 2-fermion background distribution.

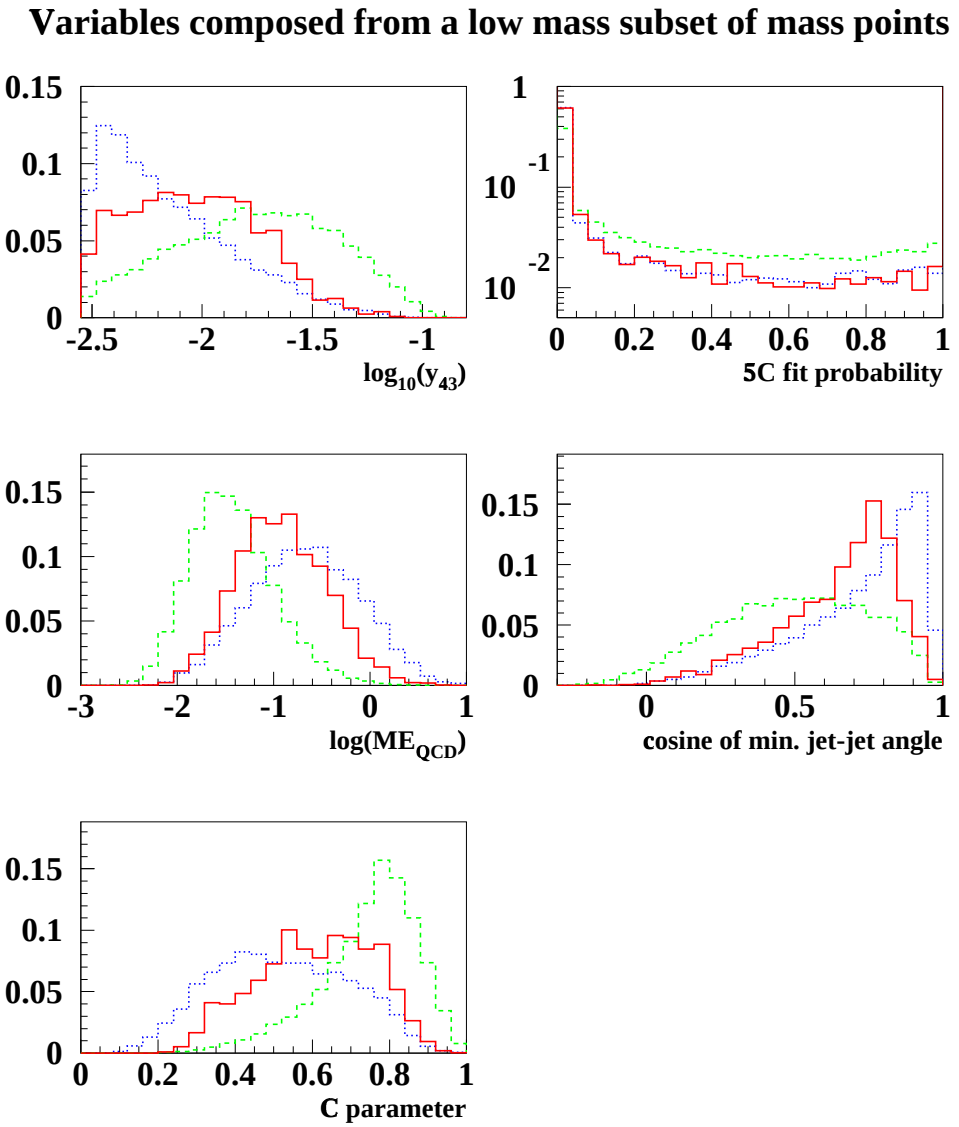

Figure A.3: Reference distributions for the second approach under comparison. The signal distributions are made using the subset of mass points, $m_h(m_A)$= 30 GeV and $m_A(m_h)$= 40, 60, 80, 100, 120, 140, 160 GeV. The colour code is as in fig. A.2.

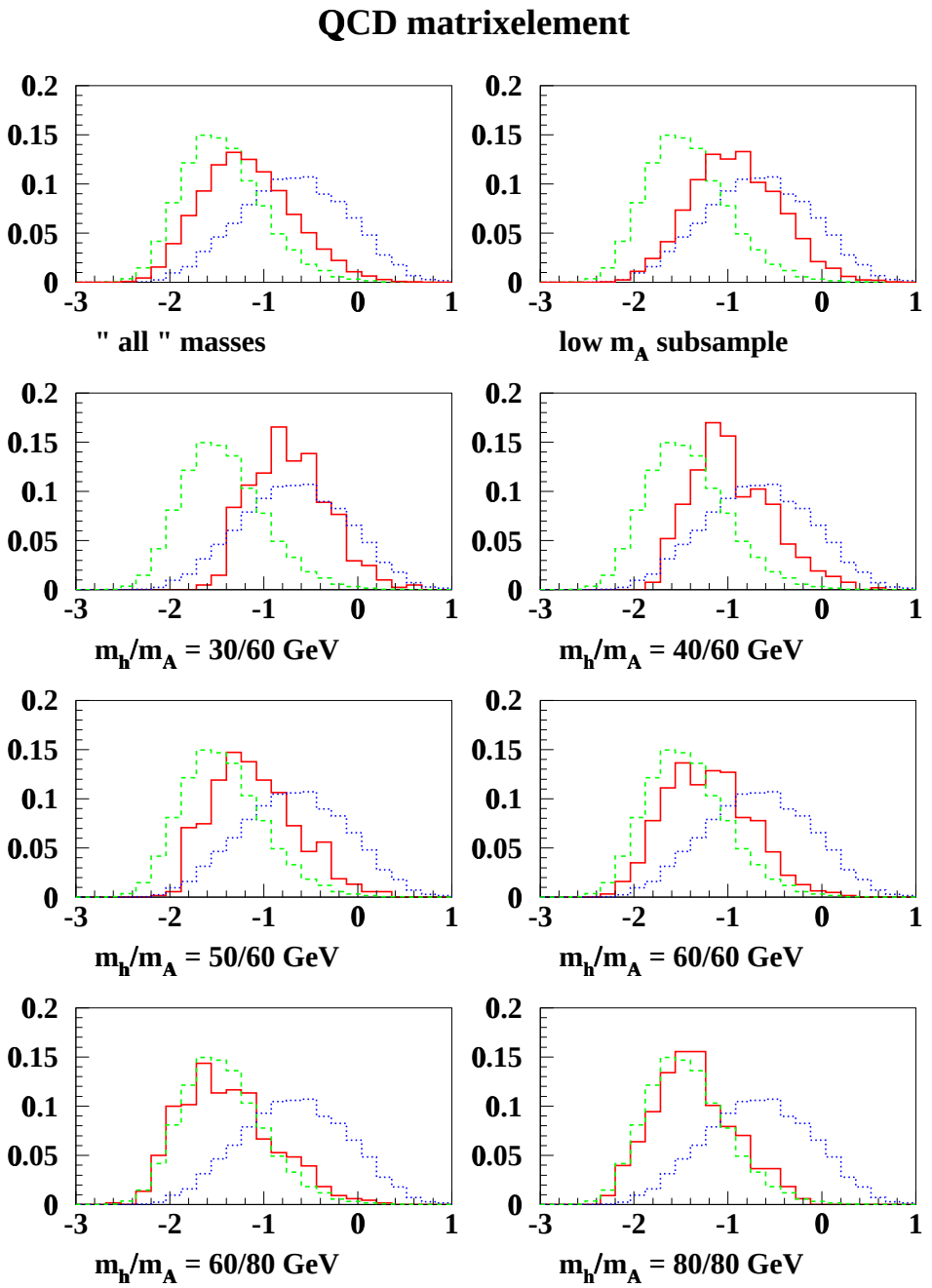

Figure A.4: Distribution of the logarithm of the QCD matrixelement for several mass hypotheses. The colour code is as in fig. A.2.

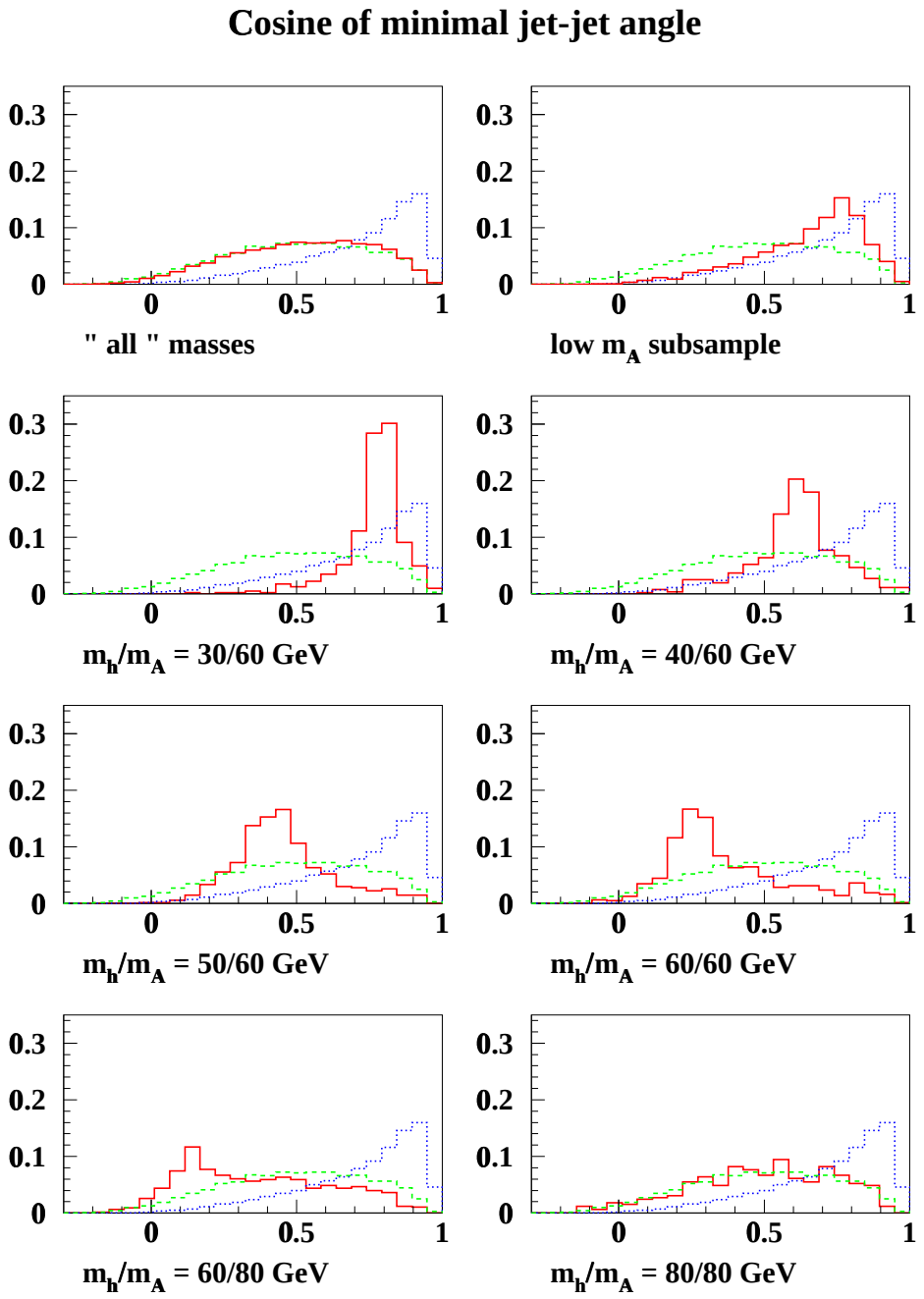

Figure A.5: Distribution of the cosine of the minimal jet-jet angle for several mass hypotheses. The colour code is as in fig. A.2.

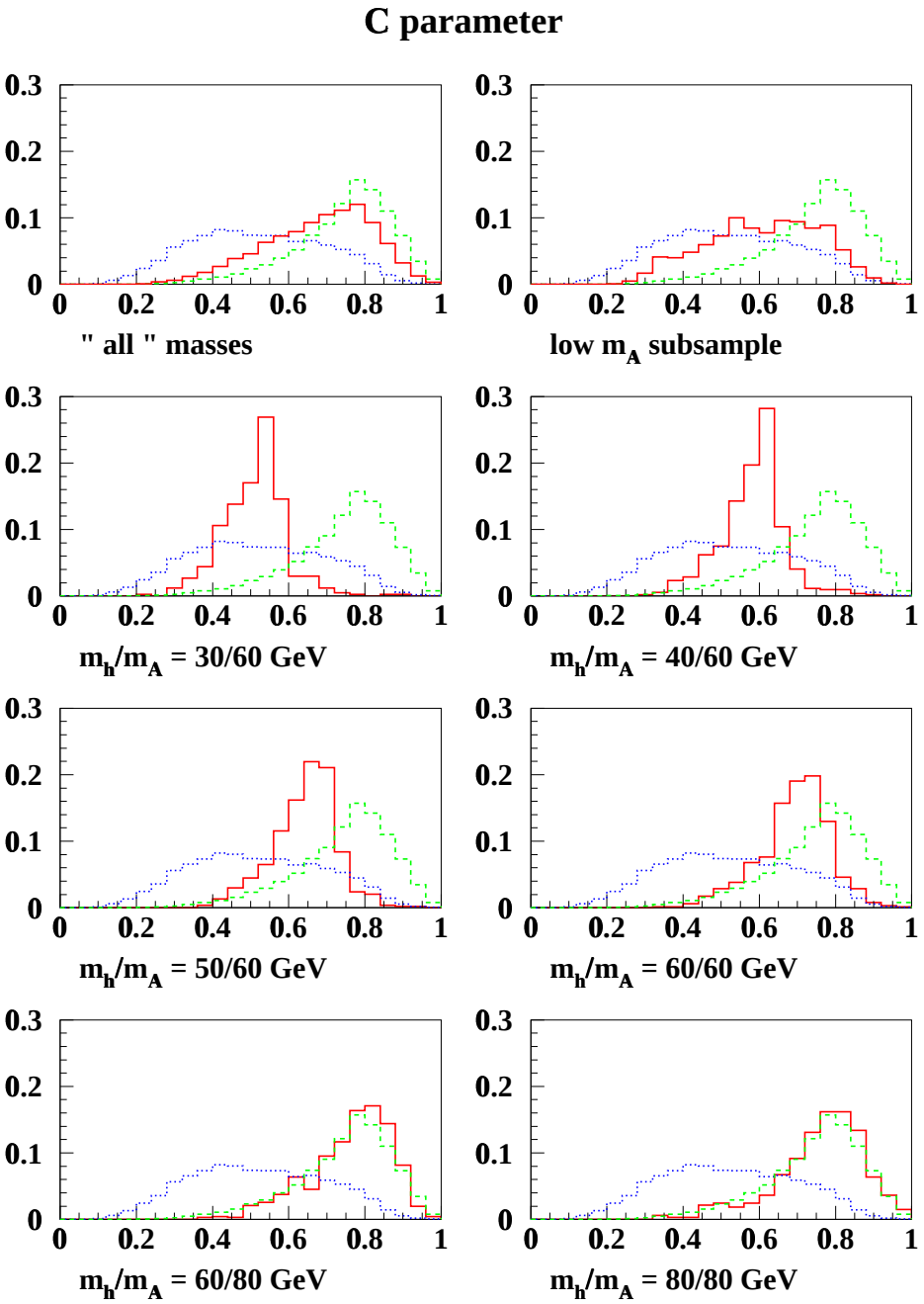

Figure A.6: Distribution of the C parameter for several mass hypotheses. The colour code is as in fig. A.2.

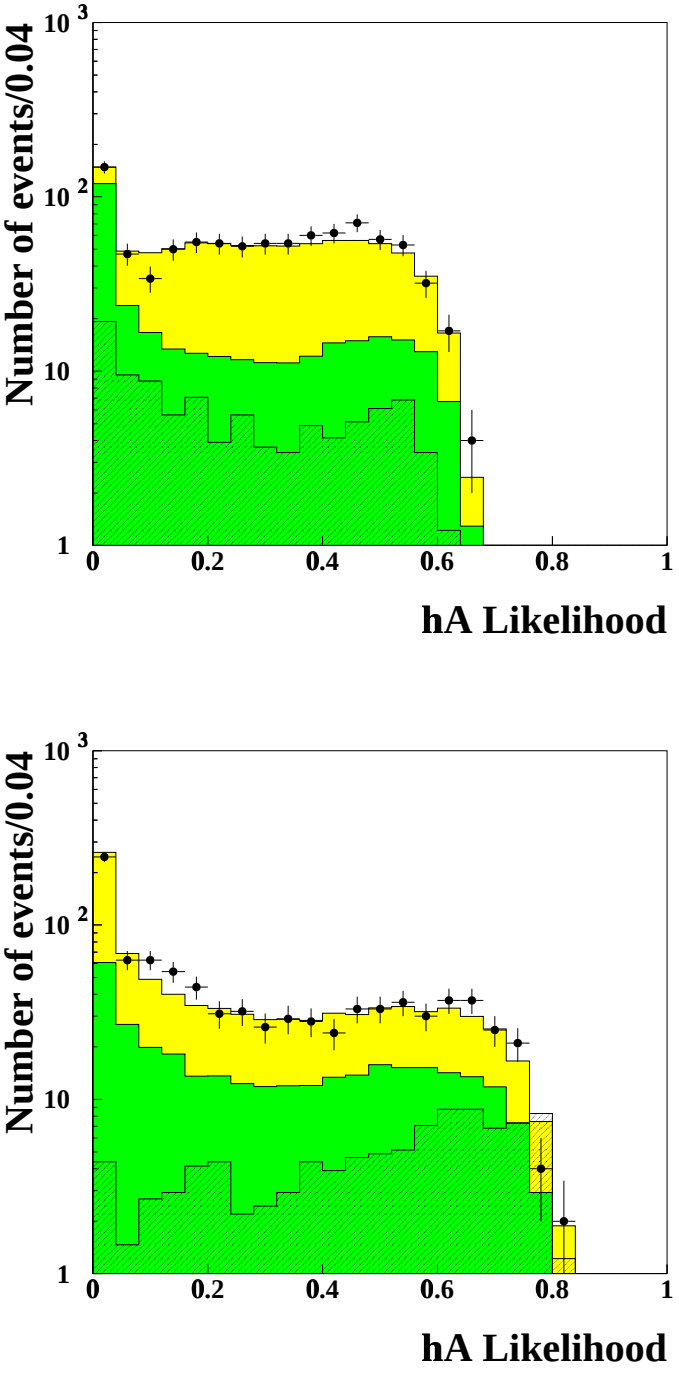

Figure A.7: Distribution of the hA Likelihood for a signal of $m_h = 30$ GeV and $m_A = 60$ GeV. The green (dark grey) histogram shows the 2-fermion background and the yellow (light grey) histogram shows the 4-fermion background on top of the latter. The points with error bars show OPAL data at a centre-of-mass energy of 189 GeV. The hatched histogram shows how a signal would be distributed for $m_h = 30$ GeV and $m_A = 60$ GeV. The number of signal events shown belongs to 5 times the number of expected events for the given data luminosity, a value of $\tan\beta$=0.7, $\alpha = 0$ and a signal efficiency of 40.5%. The top plot in this figure shows the shapes for an analysis building the signal reference histograms from all masses, the bottom plot shows the same for reference histograms build from the subset of points.

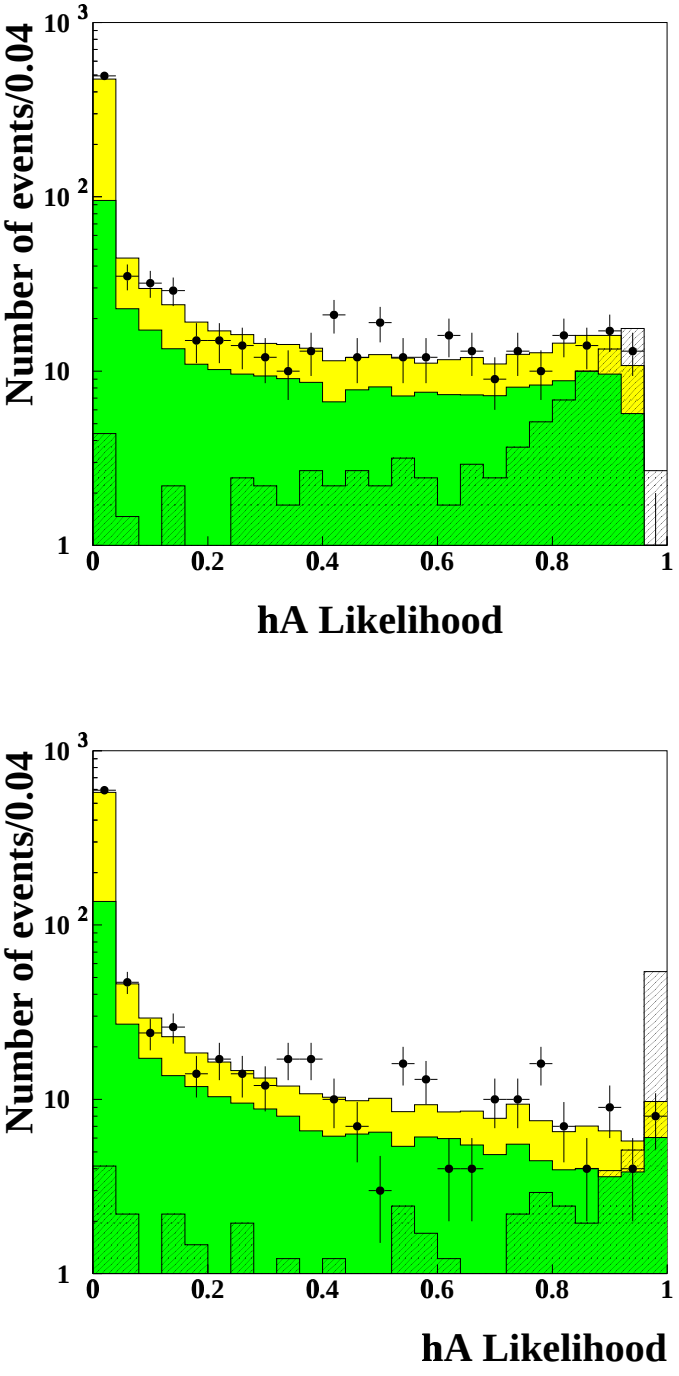

Figure A.8: Distribution of the hA Likelihood for a signal of $m_h = 30$ GeV and $m_A = 60$ GeV. The colour code is as in fig. A.7. Again the number of signal events shown belongs to 5 times the number of expected events for the given data luminosity, a value of $\tan\beta$=0.7, $\alpha = 0$ and a signal efficiency of 40.5%. The top plot shows the shapes for an analysis building the reference histograms from the mass point $m_h = 30$ GeV and $m_A = 60$ GeV itself. The bottom plot shows the same, but including a sixth variable into the likelihood, the logarithm of the χ^2 function as described in 6.4.1 on page 47.

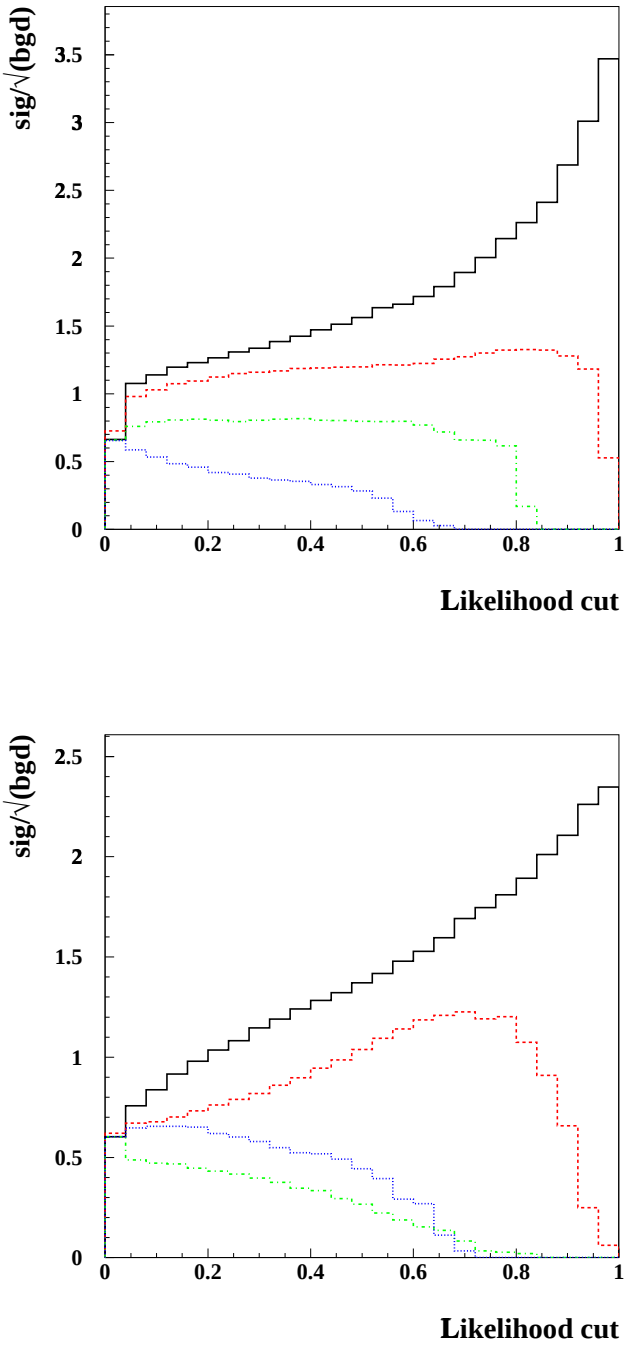

Figure A.9: Signal over square root of background ratios for different approaches and signal mass hypotheses of $m_h = 30$ GeV and $m_A = 60$ GeV and $m_h = 60$ GeV and $m_A = 60$ GeV. The signal is normalised to the number of signal events belongs to the number of expected events for the given data luminosity, a value of $\tan\beta$=0.7, $\alpha = 0$ and the for the mass according efficiency. The blue (dotted) line shows the ratio using the all mass analysis, the green line (dashed-dotted) shows the ratio resulting from a the subset approach, the red (dashed) line shows the mass-dependent result and the black (solid) line shows for comparison how the ratio is improved including the sixth input variable. The top plot in this figure is for a signal mass of $m_h = 30$ GeV and $m_A = 60$ GeV, the bottom plot for a signal mass of $m_h = 60$ GeV and $m_A = 60$ GeV.

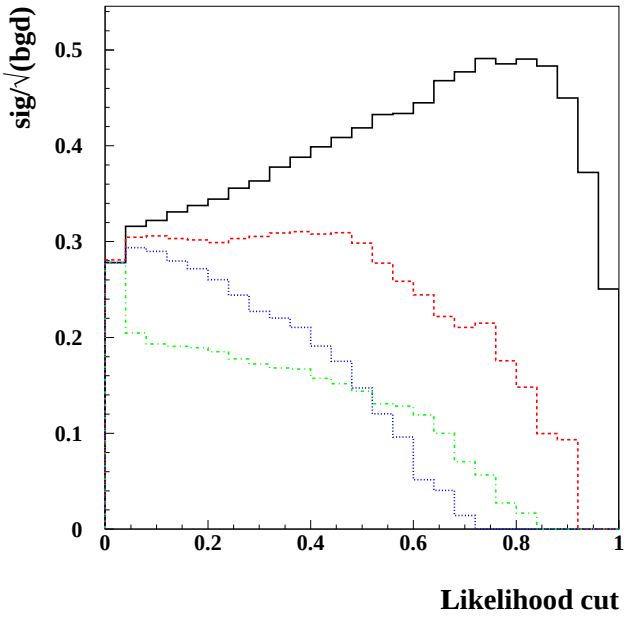

Figure A.10: Signal over square root of background ratios for different approaches and a signal mass hypothesis of $m_h = 60$ GeV and $m_A = 90$ GeV. The colour code and features are the same as in fig. A.10.

Appendix B

Efficiencies for different signal processes

masses	$c\bar{c}$	$b\bar{b}$	gg	masses	$c\bar{c}$	$b\bar{b}$	gg
30/ 30	7.9	9.4	9.0	50/ 80	61.9	62.0	68.0
30/ 40	14.1	13.4	17.2	50/100	62.8	64.0	70.0
30/ 60	40.5	39.4	48.4	50/120	66.3	69.2	68.8
30/ 80	49.6	48.6	59.6	50/140	48.8	48.6	58.8
30/100	53.0	50.2	60.4	60/ 60	63.2	64.0	67.0
30/120	56.8	54.0	64.4	60/ 70	66.2	65.0	68.4
30/140	50.3	50.4	65.8	60/ 90	68.9	66.4	73.4
30/160	30.3	31.0	33.8	60/110	68.3	67.6	69.0
40/ 40	24.8	24.6	24.8	60/130	58.5	57.4	61.0
40/ 50	44.7	43.8	48.4	70/ 70	68.5	68.4	73.6
40/ 70	57.2	57.6	60.8	70/ 80	66.6	64.0	68.0
40/ 92	58.6	60.0	65.6	70/100	67.8	71.6	71.6
40/110	59.0	59.6	68.8	70/120	61.7	60.4	66.6
40/130	57.9	55.4	67.0	80/ 80	32.8	30.0	46.6
40/150	44.1	39.4	45.4	80/ 90	67.5	74.4	67.8
50/ 50	50.3	52.6	59.6	90/ 90	80.3	80.8	77.2
50/ 60	53.7	56.4	65.2	90/100	64.3	65.4	69.0

Table B.1: Selection efficiencies for $e^+e^- \to Z/\gamma \to c\bar{c}, b\bar{b}, gg$. The first column indicates the point in the m_h, m_A plane, the following columns show the efficiencies in % for the decay of h and A to $c\bar{c}, b\bar{b}, gg$ respectively.

Appendix C

Monte Carlo Samples

This appendix lists the Monte Carlo samples that were used in the presented analysis of the OPAL data at center-of-mass energies of $\sqrt{s} = 189$ GeV.

Run number	Generator info	events per mass point
9248	HZHA2	1000
10597	HZHA2	1000
10701	HZHA2	1000

Table C.1: Monte-Carlo signal samples.

Run number	Generator info	events per mass point
9248	HZHA2	1000
7875	HZHA2	500
10113	HZHA2	500

Table C.2: Monte-Carlo signal samples for systematic checks.

Background	Run number	Generator info	Events
WW/ZZ	7846	`grc4f`	42088
Z/γ	5078	PYTHIA	500000
$e^+e^-q\bar{q}$	7849	`grc4f`	127583
$ll q\bar{q}$	8055	`grc4f`	43396

Table C.3: Monte-Carlo samples used as background in this analysis.

Bibliography

[1] D.E.Groom *et al.* Review of Particle Physics. *Eur. Phys. J.*, C(15):1, 2000.

[2] H. Weyl. *Ann. Phys.*, 59:101, 1919.

[3] G.L. Kane J.F. Gunion, H.E. Haber and S. Dawson. *The Higgs Hunter's Guide*. Perseus Publishing, Cambridge, Massachusetts, 2000.

[4] B. Pietrzyk. The global fit to electroweak data. In *Proceedings of XXXth International Conference on High Energy Physics*, Osaka, Japan. To be published.

[5] P. Igo-Kemenes. Search for New Particles and New Phenomena, Results from e^+e^- Colliders . Osaka, Japan. To be published.

[6] G. Altarelli, T. Sjöstrand, and F. Zwirner Eds. Physics at LEP2. CERN 96-01, CERN, 1996. Volume 1.

[7] K. Ahmet *et al.* The OPAL Collaboration. *Nucl. Instr. and Meth.*, A(305):275–319, 1991.

[8] P.P. Allport *et al.* The OPAL Silicon Microvertex Detector. *Nucl. Instr. and Meth.*, A(324):34, 1993.

[9] P.P. Allport *et al.* The OPAL Silicon Strip Microvertex Detector with Two Coordinate Readout. *Nucl. Instr. Meth.*, A(346):476, 1994.

[10] S. Anderson *et al.* The extended OPAL silicon strip microvertex detector. *Nucl. Instr. Meth.*, A(403):326, 1998.

[11] O. Biebel *et al.* Performance Of The OPAL Jet Chamber. *Nucl. Instr. Meth.*, A(323):169, 1992.

[12] Michael Hauschild. Personal communication.

[13] J. March-Russel N. Ellis. 1998 European School of High-Energy Physics. CERN 99-04, CERN, July 1999.

[14] G. Aguillion *et al.* Thin Scintillating Tiles with High Light Yield for the OPAL Endcaps. *Nucl. Instr. Meth.*, A(417):266, 1998.

[15] G. Abbiendi *et al.* The OPAL Collaboration. Precision Luminosity for Z0 Lineshape Measurements with a Silicon-Tungsten Calorimeter. *Eur. Phys. J.*, C(14):373, 2000.

[16] M. Arignon *et al.* The Trigger System of the OPAL Experiment at LEP. *Nucl. Instr. Meth.*, A(313):103, 1992.

[17] M. Arignon *et al.* The Pretrigger System of the OPAL experiment at LEP. *Nucl. Instr. Meth.*, A(333):330, 1993.

[18] T.J. Smith P.S. Wells D.G. Charlton, F. Meijers. The Online Event Filter of the OPAL experiment at LEP. *Nucl. Instr. Meth.*, A(325):129, 1993.

[19] R. Brun. GEANT 3 User's Guide. CERN /DD/EE/84-1, CERN, 1984.

[20] J. Allison et al. The Detector Simulation Program for the OPAL Experiment at LEP. *Nucl. Instr. Meth.*, A(317):47–74, 1992.

[21] C. Hawkes, D. Lellouch, M. Redmond, O. Schaile, and M. Schröder. Rope410. OPAL-Offline note 16/OFFL-0487, CERN, 1996.

[22] T. Sjöstrand. The PYTHIA program. *Comp. Phys. Comm.*, (82):74, 1994.

[23] J. Fujimoto, T. Ishikawa, T. Kaneko, K. Kato, S. Kawabata, Y. Kurihara, T. Munehisa, D. Perret-Gallix, Y. Shimizu, and H. Tanaka. Grc4f v1.1: a four-fermion event generator for e+e- collisions. *Comp. Phys. Comm.*, (100):74, 1997.

[24] T. Sjöstrand. High-Energy Physics Event Generation with PYTHIA 5.7 and JETSET 7.4. *Comp. Phys. Comm.*, (82):74, 1994.

[25] HZHA generator: P. Janot. Physics at LEP2. CERN 96-01, CERN, 1996. Volume 2.

[26] K. Ackerstaff *et al.* The OPAL Collaboration. Tests of the standard model and constraints on new physics from measurements of fermion-pair production at 130-172 GeV at LEP. *Eur. Phys. J.*, C(2):441, 1998.

[27] T. Omori, S. Asai, I. Nakamura, and S. Yamashita. A Matching Algorithm: MT package. OPAL Technical Note TN381, CERN, 1996.

[28] T. Omori, S. Asai, and I. Nakamura. Attempt to Compensate Energy in OPAL Calorimeter Complex based on MT Package. OPAL Technical Note TN447, CERN, 1996.

[29] S. Mihara and S. Yamashita. MT 3.00 a new algorithm to calculate energy flow based on MT package. OPAL Technical Note TN575, CERN, 1998.

[30] N. Brown and W.J. Stirling. *Phys. Lett.*, B(252):657, 1990.

[31] N. Brown and W.J. Stirling. Finding Jets and Summing Soft Gluons: A New Algorithm. *Z. Phys.*, C(53):629–636, 1992.

[32] S. Yamashita. OPAL Technical Note TN579, CERN, 1998.

[33] W. Bartel *et al.* JADE Collaboration. *Z. Phys.*, C(33):23, 1986.

[34] S. Bethke *et al.* JADE Collaboration. *Phys. Lett.*, B(213):235, 1988.

[35] The OPAL Collaboration. Colour reconnection studies in $e^+e^- \rightarrow W^+W^-$ at $\sqrt{s}$ = 189 GeV. OPAL Physics Note PN417, CERN, 1998.

[36] S. Catani and B.R. Webber. Resummed C-Parameter Distribution in e^+e^- Annihilation. *Phys. Lett.*, B(427):377, 1998.

[37] G. Parisi. Superinclusive cross-sections. *Phys. Lett.*, B(74):65, 1978.

[38] O. Skjeggestad A. G. Frodesen and H. Tøfte. *PROBABILITY AND STATISTICS IN PARTICLE PHYSICS*. Universitetsforlaget, Bergen-Oslo-Tromsø, 1979.

[39] The OPAL Collaboration, G. Abbiendi *et al.* Two Higgs Doublet Model and Model Independent Interpretation of Neutral Higgs Boson Searches. CERN-EP 2000-092, CERN, 2000. Submitted to Eur. Phys. J. C.

[40] S. Catani and M.H. Seymour. The Dipole Formalism for the Calculation of QCD Jet Cross Sections at Next-to-Leading Order. *Phys.Lett.*, B:287–301, 1996.

[41] A. L. Read DELPHI Collaborations. Optimal Statistical Analysis of Search Results based on the Likelihood Ratio and its Application to the Search for the MSM Higgs Bosons at $\sqrt{s}$=161 and 172 GeV. DELPHI Physics Note 97-158 PHYS 737, CERN, 1997.

[42] T. Junk. Confidence Level Computation for Combining Searches using the Likelihood Ratio. OPAL Technical Note TN570, CERN, 1999.

[43] T. Junk. Confidence Level Computation for Combining Searches with Small Statistics. OPAL Physics Note Phys99-01, CERN, 1999.

[44] P.Bock. Determination of Exclusion Limits for Particle Production Using Different Decay Channels with Different Energies, Mass Resolutions and Backgrounds. OPAL-IP 059, CERN, 1997. to be submitted to Nucl. Inst. and Methods.

[45] Pamela Ferrari. Personal communication.

Acknowledgement

This work would have never come to reality without the help and support of many people.

Dorothee Schaile made it possible that this work could be realised in the inspiring atmosphere of CERN within the lively and friendly OPAL community. I thank my collegues at Cern and in munich, particularly Joerg Dubbert, Pamela Ferrari, Dezso Horváth, Tom Junk, Axel Leins, Koichi Nagai and Thomas
Trefzger for their help, fruitfull discussions and lots and lots of Monte Carlo events (thanks a lot Koichi!), without—no doubt—this analysis would not exist today.

I thank my friends back home, and the friends I made at Cern for their help and love, for cheering me up, for letters and music tapes, phone calls and visits and dragging me away from work and for still emailing me when I never reply. Thank you Barbara, David, Gabriele, Greg, Henrik, John, Michele, Monique, Moritz, Pete, Rhona, Sam, Steve, Theresa, Tim and Valeria.

I thank Tim for having been there for me all this time, however much annoying I was at times, thank you for being a true friend. And I thank John for having made Geneva home.

I thank my parents and my sister for their unfailing love, little parcels and phone calls, faxes and letters with little smiling faces on, and for that they made all this possible for me.

Thank you!

Erklärung

Ich versichere hiermit, die vorliegende Arbeit selbständig verfasst zu haben
und keine anderen als die angegebenen Quellen und Hilfsmittel benutzt zu haben.

München, den 25. September 2000

Tatjana Unverhau